

## REPORT 1307

# LIFT AND CENTER OF PRESSURE OF WING-BODY-TAIL COMBINATIONS AT SUBSONIC, TRAN- SONIC, AND SUPERSONIC SPEEDS

By WILLIAM C. PITTS, JACK N. NIELSEN, and GEORGE E. KAATTARI

### SUMMARY

A method is presented for calculating the lift and center-of-pressure characteristics of circular-cylindrical bodies in combination with triangular, rectangular, or trapezoidal wings or tails through the subsonic, transonic, and supersonic speed ranges. The method is restricted to wings which are unbanked and do not have sweptback trailing edges or sweptforward leading edges. The method is further restricted to small angles of attack and small angles of wing and tail incidence. To obtain the wing-body interference, certain factors are defined that are the ratios of the lift on the components in combination to the lift on the wing alone. These ratios are obtained primarily by slender-body theory. The wing-tail interference is treated by assuming one completely rolled-up vortex per wing panel and evaluating the tail load by strip theory. A numerical example is included to show that the computing form and design charts presented reduce the calculations to routine operations. Comparison is made between the estimated and experimental characteristics for a large number of wing-body and wing-body-tail combinations. Generally speaking, the lifts were estimated to within  $\pm 10$  percent and the centers of pressure were estimated to within  $\pm 0.02$  of the body length.

### INTRODUCTION

The problems of the interference among the components of airplanes or missiles have received much attention because of their great importance in high-speed aircraft design. This importance is due to the interest in designs employing large fuselage radii and tail spans relative to the wing span. One of the notable methods for determining wing-body interference at subsonic speeds is that of Lennertz, reference 1; data supporting the work of Lennertz are presented in reference 2. Laborious methods are available (refs. 3, 4, and 5) for computing the interference load distributions of wing-body (or tail-body) combinations at supersonic speeds. A simple method is presented in reference 6 for estimating the effects of wing-body interference on lift and pitching moment when the wing is triangular. One of the notable methods for calculating wing-tail interference in subsonic aircraft design is that of Silverstein and Katzoff in references 7 and 8. For supersonic speeds, Morikawa (ref. 9) has examined the four limiting cases of zero and infinite aspect ratio for wing and tail and has found that the loss of lift due to interference can be as large as the lift of the wing itself for equal wing and tail spans.

Using slender-body theory, Lomax and Byrd (ref. 10) have analyzed the wing-tail interference of a family of combinations having swept wings. Several authors have studied problems of the nonuniform downwash field behind wings in combination with a body at supersonic speeds; Lagerstrom and Graham (ref. 11) present solutions for certain vortex models representing the downwash field. The assumption of one fully rolled-up vortex per wing panel should provide a good prediction of the downwash even relatively close behind unbanked low-aspect-ratio triangular wings at small angles of attack. However, for large aspect ratios or high angles of attack more than one vortex per wing panel is probably needed to provide agreement between theory and experiment. With regard to the problem of determining the tail loads due to a nonuniform downwash field, Lagerstrom and Graham (ref. 11) advocate the use of strip theory. Alden and Schindel (ref. 12) have developed a method based on linear theory for determining the tail load in certain cases.

The purpose of the present report is twofold: first, to present a unified procedure for calculating interference effects and to examine the assumptions underlying the procedure; and, second, to compare the predictions of the method with experiment in order to estimate the accuracy of the predictions and their range of application.

### SYMBOLS<sup>1</sup>

#### PRIMARY SYMBOLS

$A_T$	tail-alone aspect ratio
$A_W$	wing-alone aspect ratio
$\bar{c}$	mean aerodynamic chord of wing alone or tail alone, in.
$c_r$	chord at wing-body juncture or tail-body juncture, in.
$c_t$	tip chord of wing or tail, in.
$c_y$	wing chord at spanwise distance $y$ from body axis, in.
$C_h$	hinge-moment coefficient based on wing-alone area
$C_{h\alpha}$	rate of change of hinge-moment coefficient with angle of attack, per radian
$C_{h\beta}$	rate of change of hinge-moment coefficient with wing incidence angle, per radian

<sup>1</sup> The wing alone or tail alone is always defined to be the exposed panels of the wing or tail joined together.

$C_L$	lift coefficient based on wing-alone area except tail-alone lift coefficient based on tail-alone area	$s$	maximum semispan of wing or tail in combination with body, in.
$C_{L_\alpha}$	lift-curve slope for angle of attack, per radian (unless otherwise specified)	$S_N$	cross-sectional area of nose at maximum section, sq in.
$C_{L_\delta}$	lift-curve slope for wing or tail incidence, per radian (unless otherwise specified)	$S_R$	reference area of combination lift coefficient, sq in.
$C_m$	pitching-moment coefficient based on wing-alone area	$S_T$	tail-alone area, sq in.
$C_{m_\alpha}$	pitching-moment-curve slope for angle of attack, per radian (unless otherwise specified)	$S_W$	wing-alone area, sq in.
$C_{m_\delta}$	pitching-moment-curve slope for wing-incidence angle, per deg	$\left(\frac{t}{c}\right)$	ratio of wing maximum thickness to chord length
$d$	body diameter, in.	$V$	volume of body, considering the body as cylindrical behind the position of maximum cross section, cu in.
$E$	complete elliptic integral of second kind	$V_S$	volume of body nose up to shoulder, cu in.
$f_T$	wing vortex semispan at tail position, in.	$V_\infty$	free-stream velocity, in./sec
$f_W$	wing vortex semispan at wing trailing edge, in.	$x, y, z$	streamwise, spanwise, and vertical coordinates, respectively
$f_\infty$	wing vortex semispan for large downstream distances, in.		distance to center of pressure measured from intersection of wing leading edge and body for wing quantities and from intersection of tail leading edge and body for tail quantities, in.
$F(\eta)$	Alden-Schindel influence coefficient at spanwise distance $\eta$	$\bar{x}_y$	distance to local center of pressure at spanwise distance $y$ measured from intersection of wing leading edge and body, in.
$g_T$	image vortex semispan at tail position, in.	$x_h$	distance from intersection of wing leading edge and body to wing hinge line, in.
$g_W$	image vortex semispan at wing trailing edge, in.	$\alpha$	angle of attack of body centerline or of wing alone, radian (unless otherwise specified)
$h_T$	height of wing vortex above body axis at tail center of pressure, in.	$\alpha_y$	local angle of attack at spanwise location $y$ from body axis, radians
$i$	tail interference factor	$\beta$	$\sqrt{M_\infty^2 - 1}$
$k$	ratio of lift component to lift of wing alone or tail alone for variable wing or tail incidence	$\beta A$	wing-alone or tail-alone effective aspect ratio
$K$	ratio of lift component to lift of wing alone or tail alone for variable angle of attack	$\Gamma$	circulation, positive counterclockwise facing upstream, sq in./sec
$K_N$	ratio of lift of body nose to lift of wing alone	$\Gamma_m$	circulation at wing-body juncture of combination, sq in./sec
$l$	length of wing-body-tail combination, in.	$\delta$	wing-or tail-incidence angle, radians
$l_W$	distance from most forward point of body to intersection of wing leading edge and body, in.	$\epsilon$	wing semiapex angle, deg
$l_M$	distance from most forward point of body to center of moments, in.	$\eta$	spanwise variable of integration
$l_R$	moment reference length, in.	$\lambda$	taper ratio, $\left(\frac{c_t}{c_r}\right)$
$l_S$	distance from most forward point of body to shoulder of body nose, in.	$\Lambda_{LE}$	sweep angle of leading edge, deg
$l_T$	distance from most forward point of body to intersection of tail leading edge and body, in.	$\Lambda_{TE}$	sweep angle of trailing edge, deg
$\bar{l}$	distance from most forward point of body to center of pressure position, in.	$\rho_\infty$	free-stream density, slugs/cu in.
$L$	lift force, lb	SUBSCRIPTS	
$L_{T(V)}$	lift on tail section due to wing vortices, lb	$B$	body
$L_{B(V)}$	lift on body section between wing and tail due to wing vortices, lb	$C$	combination, either wing-body or wing-body-tail
$m$	cotangent of leading-edge sweep angle	$C-N$	combination minus nose
$M$	pitching moment, lb-in.	$F$	forebody
$M_\infty$	free-stream Mach number	$N$	body nose
$\Delta p$	static pressure difference between top and bottom of wing, lb/sq in.	$T$	tail
$q_\infty$	free-stream dynamic pressure, lb/sq in.	$V$	wing vortex
$r$	body radius, in.	$W$	wing
$r_N$	body radius at shoulder of nose, in.	$AS$	Alden-Schindel theory
$r_W$	body radius at wing, in.	$B(T)$	body in presence of tail
$r_T$	body radius at tail, in.	$B(W)$	body in presence of wing
$R$	Reynolds number based on $\bar{c}$ of larger lifting surface	$ST$	strip theory
		$T(B)$	tail in presence of body

$W(B)$  wing in presence of body  
 $\alpha$   $\alpha$  variable,  $\delta$  constant  
 $\delta$   $\delta$  variable,  $\alpha$  constant  
 $W(B)\alpha$  wing in presence of body and  $\alpha$  variable,  $\delta$  constant  
 Other compound subscripts to be interpreted similarly to the preceding compound subscript.

### GENERAL THEORETICAL CONSIDERATIONS

Before presenting the detailed development of the method, an outline of the approach to be followed is presented. The theory is restricted to small angles of attack and small angles of wing and tail incidence. Attention is focused on pointed bodies having wings and tails mounted on body sections of uniform diameter. For the sake of consistency, the forward lifting surfaces are termed the wings, even in cases of canard configurations. Both wings and tails may have variable incidence, but cases of differential incidence between opposite panels of the wing or tail are beyond the scope of this report.

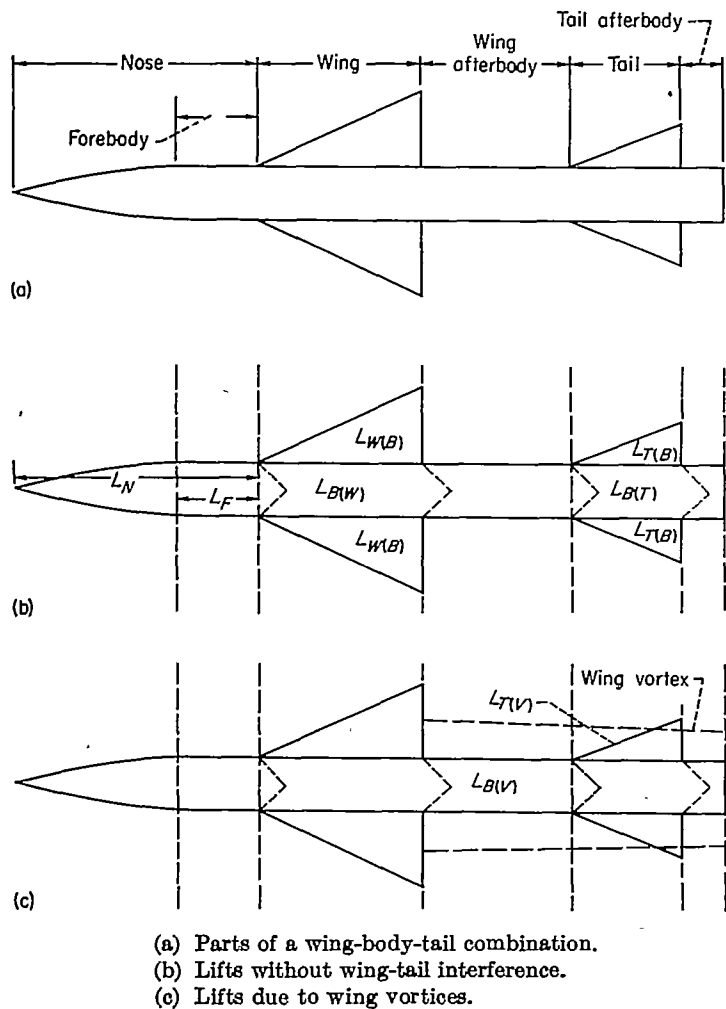


FIGURE 1.—Parts and lift components of a wing-body-tail combination.

The terminology is indicated in figure 1 (a). The nose is that part of the body in front of the wing. However, when the wing is mounted on an expanding section of the body, the nose is taken to be the entire expanding part of the body. For the purpose of analysis, the lift of the wing-body-tail combination is taken to be the sum of the seven

principal components indicated in parts (b) and (c) of figure 1.\* These components are:

1. Lift on nose including forebody,  $L_N$
2. Lift on wing in presence of body,  $L_{W(B)}$
3. Lift on body due to wing,  $L_{B(W)}$
4. Lift on tail in presence of body,  $L_{T(B)}$
5. Lift on body due to tail,  $L_{B(T)}$
6. Lift on tail due to wing vortices,  $L_{T(V)}$
7. Lift on wing afterbody due to wing vortices,  $L_{B(V)}$

All coefficients, except those for the tail alone, are based on the exposed wing area. The lift and center-of-pressure position calculation procedures for tail-body interference are identical to those for wing-body interference, except for a term to refer the tail-body interference lifts to the wing area; therefore, they will not be treated separately.

The method presented for computing the wing-body and tail-body interference (components 2 through 5) is based primarily on slender-body theory (ref. 13). In this theory, Spreiter has shown that the first term of the wave equation for the velocity potential

$$(M_\infty^2 - 1)\varphi_{xx} - \varphi_{yy} - \varphi_{zz} = 0 \quad (1)$$

can be ignored for slender wing-body combinations, so that equation (1) reduces to Laplace's equation in the  $y, z$  plane. Using this simplification, simple, closed expressions are obtained for lift-curve slopes.

It is well known that for wing-body combinations which are not slender, lift-curve slopes are overestimated by slender-body theory (ref. 6). However, this fact does not preclude the use of slender-body theory for nonslender configurations since, in certain instances, the ratio of the lift of the wing-body combination to that of the wing alone can be accurately predicted by slender-body theory, even though the magnitude of the lift-curve slope might be incorrect. From the foregoing ratio, which is called  $K_C$ , and a good estimate of the wing-alone lift-curve slope, the lift-curve slope of the combination can be obtained. This was essentially the method used by Nielsen, Katzen, and Tang in reference 6 to predict the lift and moment characteristics of triangular wing-body combinations. Good agreement between experiment and theory was obtained.

With these facts in mind, the method used by Morikawa (ref. 14) for presenting lift interference is adopted. In this method, the wing alone is defined as the exposed half-wings joined together. The lift of the combination is related to the lift of the wing alone by the factor  $K_C$  which is to be determined.

$$L_C = K_C L_W \quad (2)$$

The factor  $K_C$  is decomposed into three factors  $K_{B(W)}$ ,  $K_{W(B)}$ , and  $K_N$  which represent the ratios of the body lift, wing lift, and nose lift of the combination to that of the wing alone.

$$K_C = K_{B(W)} + K_{W(B)} + K_N \quad (3)$$

$$K_{B(W)} = \frac{L_{B(W)}}{L_W} = \frac{(C_{L_\alpha})_{B(W)}}{(C_{L_\alpha})_W} \quad \delta = 0 \quad (4)$$

$$K_{W(B)} = \frac{L_{W(B)}}{L_W} = \frac{(C_{L_\alpha})_{W(B)}}{(C_{L_\alpha})_W} \quad \delta = 0 \quad (5)$$

$$K_N = \frac{L_N}{L_W} = \frac{(C_{L\alpha})_N}{(C_{L\alpha})_W} \quad (6)$$

The factors  $K_{B(W)}$  and  $K_{W(B)}$  are defined for the case in which the angle of attack of the combination is varying but the wing- (or tail) incidence angle is zero. For the case in which the incidence angle is varying but the angle of attack of the body is zero, two analogous factors are defined.

$$k_{B(W)} = \frac{L_{B(W)}}{L_W} = \frac{(C_{L\alpha})_{B(W)}}{(C_{L\alpha})_W} \quad \alpha=0 \quad (7)$$

$$k_{W(B)} = \frac{L_{W(B)}}{L_W} = \frac{(C_{L\alpha})_{W(B)}}{(C_{L\alpha})_W} \quad \alpha=0 \quad (8)$$

So far, only a way of representing lift results has been presented. The solution of a problem requires a determination of each of these ratios. Then, the lift on any component can be estimated from the wing-alone lift-curve slope. The best value of the wing-alone lift-curve slope that is available should be used; preferably the experimental value. The detailed determination of each of these ratios is presented in subsequent sections of this report. In general, slender-body-theory values are computed. These are compared with values computed by other methods and ultimately with experimental results. There are some conditions for which slender-body theory is invalid or for which more exact methods are available. These are pointed out and the slender-body-theory values for the ratios are replaced.

#### LIFT THEORY

The lift theory as developed is for the angle-of-attack range over which the lift curves are linear and is equally applicable to subsonic and supersonic speeds unless otherwise noted.

##### LIFT ON BODY NOSE

From equation (6)

$$C_{L_N} = K_N (C_{L\alpha})_W \alpha \quad (9)$$

For the calculations in this report,  $L_N$  is evaluated by use of slender-body theory,

$$\frac{L_N}{q_\infty} = 2\pi r_N^2 \alpha \quad (10)$$

$$L_F = 0 \quad (11)$$

so that

$$K_N = \frac{2\pi r_N^2}{S_W (C_{L\alpha})_W} \quad (12)$$

It is known that slender-body theory is usually not sufficiently accurate to determine body-alone lifts in cases such as nonslender bodies or large angles of attack. However, for combinations which are not predominantly body, the nose lift is not a large part of the total lift, and slender-body theory generally gives satisfactory results. If improved accuracy is desired, linear theory, the viscous cross-flow theory of reference 15, or experimental results can be used.

#### LIFT ON WING IN PRESENCE OF BODY

Angle of attack.—From equation (5)

$$C_{L_{W(B)}} = K_{W(B)} (C_{L\alpha})_W \alpha \quad (13)$$

when  $\delta=0$ . The value of  $(C_{L\alpha})_W$  from experiment should be used if available; otherwise the value from linear theory should be used. Therefore, obtaining  $C_{L_{W(B)}}$  depends on obtaining  $K_{W(B)}$ .

The value of  $K_{W(B)}$  given by slender-body theory (ref. 14) is

$$K_{W(B)} = \frac{2}{\pi} \left\{ \left( 1 + \frac{r^4}{s^4} \right) \left[ \frac{1}{2} \tan^{-1} \frac{1}{2} \left( \frac{s-r}{r-s} \right) + \frac{\pi}{4} \right] - \frac{r^2}{s^2} \left[ \left( \frac{s-r}{r-s} \right) + 2 \tan^{-1} \frac{r}{s} \right] \right\} \frac{1}{\left( 1 - \frac{r}{s} \right)^2} \quad (14)$$

(The assumption is made that no negative lift is developed behind the maximum wing span. Jones (ref. 16) has pointed out that for wings, at least, the negative lift predicted on these sections by slender-body theory is prevented by separation.) This function is plotted in chart 1. In the limiting case of  $r/s=0$  the combination is all wing and the value of  $K_{W(B)}=1$ . As  $r/s$  approaches unity, there is a very small exposed wing. For this small wing, the body is effectively a vertical reflection plane and the angle of attack is  $2\alpha$  due to upwash (as is discussed later). This makes  $K_{W(B)}=2$ .

It is clear that the values of  $K_{W(B)}$  should be satisfactory for slender wing-body combinations. However, they cannot be used for large aspect ratios, for which slender-body theory is inapplicable, without further investigation. An approximate method for evaluating  $K_{W(B)}$  is to suppose that the exposed wings are operating in the upwash field of the body alone and then to calculate the resultant wing lift. Neglecting any effect of the nose, it has been pointed out (ref. 17) that the upflow angle due to the body varies spanwise on the horizontal plane of symmetry as

$$\alpha_y = \alpha_B \left( 1 + \frac{r^2}{y^2} \right) \quad (15)$$

where  $y$  is the lateral distance from the body axis. The wing is thus effectively twisted by the body-alone flow. If now the upwash angle given by equation (15) is taken into account by using strip theory, an approximate value of  $K_{W(B)}$  is obtained as follows:

$$K_{W(B)} = \frac{\int_r^s \alpha_y c_y dy}{\alpha_B \int_r^s c_y dy} \quad (16)$$

Equation (16) does not include tip effects. The following expression is obtained in terms of  $r/s$  and taper for wings of uniform taper.

$$K_{W(B)} = \frac{\frac{1}{2}(1+\lambda) - \frac{\lambda r}{s} - \frac{r^2(1-\lambda)}{s^2-r^2} \ln \left( \frac{s}{r} \right)}{\frac{1}{2} \left( \frac{s-r}{s+r} \right) (1+\lambda)} \quad (17)$$

It is notable that  $K_{W(B)}$  does not depend on aspect ratio.

Equation (17) was used to determine  $K_{W(B)}$  for  $\lambda=0, \frac{1}{2}$ , and 1, and these results are compared to those of slender-body theory in figure 2. It is seen that the effect of taper is small compared to the effect of  $r/s$ . Both theories give nearly the same values at both high and low  $r/s$ , but the upwash-theory values are, in all instances, greater than those of slender-body theory. Nowhere is the difference of great significance. Although account has been taken of the upwash induced along the wing span by the body in the determination of  $K_{W(B)}$  by upwash theory, no account has been taken of the loss of lift due to interaction between the wing and the body of the winged part of the combination. For this reason,  $K_{W(B)}$  will be too large. Therefore, the slender-body-theory values of  $K_{W(B)}$  should be used for all combinations.

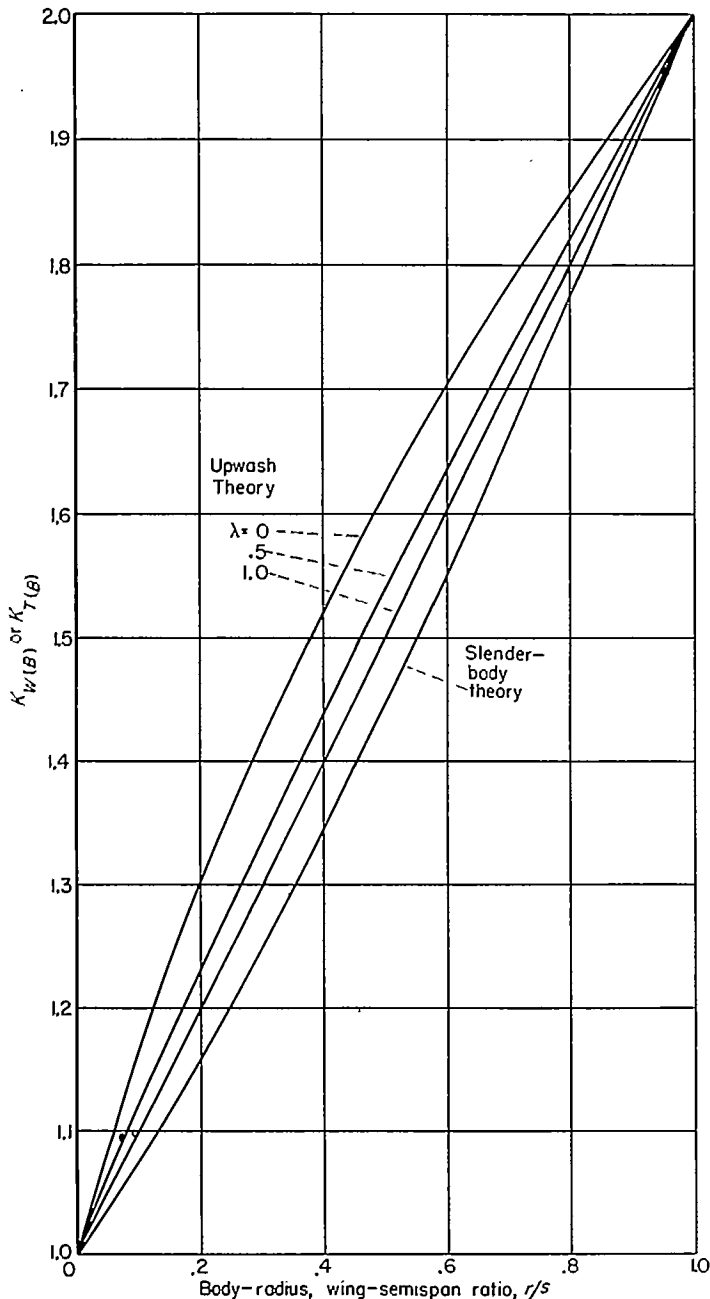


FIGURE 2.—Comparison of  $K_{W(B)}$  or  $K_{T(B)}$  determined by slender-body and upwash theories.

For wing and body combinations with large-aspect-ratio rectangular wings the linear-theory solution for  $K_{W(B)}$  is available (ref. 18). These results are presented in chart 2 where they are compared with the slender-body-theory results. Since a graphical integration was required for the determination of the linear-theory values, there is a small uncertainty in the result, represented by the cross-hatched area. For a fixed value of  $r/s$  and for the range  $2 \leq \beta A \leq 6$ , the effect of  $\beta A$  is less than the uncertainty of the calculation. No linear-theory values are available for  $\beta A < 2$ . The close agreement (within 5 percent) between linear theory for the present case and slender-body theory is noteworthy since the rectangular wing and body combinations represented are not slender.

**Wing-incidence angle.**—The method for estimating the values of  $C_{LW(B)}$  for the wing-incidence case is analogous to the method for the angle-of-attack case. From equation (8)

$$C_{LW(B)} = k_{W(B)} (C_{L\alpha})_w \delta_w \quad (18)$$

when  $\alpha=0$ .

There are several solutions available for determining  $k_{W(B)}$ ; slender-body theory for slender triangular wing and body combinations, and an exact linear theory solution for rectangular wing and body combinations. The slender-body result based on the load distribution given in Appendix A gives the following expression for  $k_{W(B)}$  in terms of  $\tau$ , the semispan-radius ratio,  $s/r$ :

$$k_{W(B)} = \frac{1}{\pi^2} \left[ \frac{\pi^2 (\tau+1)^2}{4 \tau^2} + \frac{\pi(\tau^2+1)^2}{\tau^2(\tau-1)^2} \sin^{-1} \frac{\tau^2-1}{\tau^2+1} - \frac{2\pi(\tau+1)}{\tau(\tau-1)} + \frac{(\tau^2+1)^2}{\tau^2(\tau-1)^2} \left( \sin^{-1} \frac{\tau^2-1}{\tau^2+1} \right)^2 - \frac{4(\tau+1)}{\tau(\tau-1)} \sin^{-1} \frac{\tau^2-1}{\tau^2+1} + \frac{8}{(\tau-1)^2} \log \frac{\tau^2+1}{2\tau} \right] \quad (19)$$

The value of  $k_{W(B)}$  so obtained is presented in chart 1 and is strictly applicable only to slender wing-body combinations. The exact linear-theory results for rectangular wing and body combinations, taken from reference 3, are presented in chart 3 where they are compared with the preceding slender-body results. There is generally a small difference between the two predictions, never exceeding about 10 percent for values of  $\beta A$  of 2 or greater. For the range of  $\beta A$  between 0 and 2 linear-theory results for  $k_{W(B)}$  are not available. However, as  $\beta A$  approaches zero the rectangular wing and body combination becomes more slender, until at  $\beta A=0$  slender-body theory is exact for the combination. Therefore, slender-body theory values of  $k_{W(B)}$  are used for rectangular wing-body combinations when  $\beta A < 2$ . When rectangular wings of effective aspect ratio 2 or greater are involved and when  $M_\infty > 1$ , then  $k_{W(B)}$  from linear theory should be used.

It might be surmised that the present method of determining the lift on a wing in the presence of the body is applicable at subsonic speeds since the slender-body-theory values of  $K_{W(B)}$  and  $k_{W(B)}$  on which it is based are not dependent on Mach number and the effect of Mach number enters only through  $(C_{L\alpha})_w$ . This supposition is subsequently borne out by experimental data. Spreiter made the observa-

tion in reference 13 that the loading on the minimum drag wing-body combination of Lennertz (ref. 1) is identical at low speeds to that of a slender wing-body combination with a body of uniform diameter. The division of lift between wing and body based on this loading is shown in figure 3. Since the present method is based on the division of lift as given by Spreiter, the equality of the results of Spreiter and Lennertz is further evidence of the applicability of the present method to subsonic speeds.

At this point, it is desirable to consider the effects of span loading on the division of lift between wing and body because this information has bearing on the validity of the vortex model used in determining some later results. Besides his result for minimum drag, Lennertz also determined the division of load between wing and body for uniform span loading. This result, which corresponds to replacing each side of the combination by a horseshoe vortex, is shown in figure 3, wherein the part of the lift carried by the body is shown as a function of the ratio of body radius to vortex semispan. For the same value of the abscissa there is not much difference between the fractions of the lift acting on the body for the two cases. Generally, the span of a horseshoe vortex replacing a wing is less than the wing span. If account is taken of this fact in the comparison, the existing difference would largely disappear. Thus, the representation of the wing-body combination by a horseshoe vortex on each side is compatible with the present method of determining the division of lift between wing and body.

#### LIFT ON BODY DUE TO WING

Angle of attack.—From equation (4)

$$C_{L_{B(W)}} = K_{B(W)} (C_{L_{\alpha}})_{W} \alpha \quad (20)$$

when  $\delta=0$ . The slender-body theory value of  $K_{B(W)}$  is

$$K_{B(W)} = \frac{\left(1 - \frac{r^2}{s^2}\right)^2 - \frac{2}{\pi} \left\{ \left(1 + \frac{r^4}{s^4}\right) \left[ \frac{1}{2} \tan^{-1} \frac{1}{2} \left( \frac{s-r}{r-s} \right) + \frac{\pi}{4} \right] - \frac{r^2}{s^2} \left[ \left( \frac{s-r}{r-s} \right) + 2 \tan^{-1} \frac{r}{s} \right] \right\}}{\left(1 - \frac{r}{s}\right)^2} \quad (21)$$

This function is plotted in chart 1. In the limiting case of  $r/s=0$  the combination is all wing and  $K_{B(W)}=0$ . As  $r/s$  approaches unity, there is a very small exposed wing. For this small wing the lift on the body due to the wing is the same as the lift on the wing itself. Thus,  $K_{B(W)}=K_{W(B)}=2$ .

To determine the applicability of the slender-body-theory values of  $K_{B(W)}$  to nonslender combinations,  $K_{B(W)}$  is now determined by an independent method. On the basis of slender-body theory, nonexpanding sections of a body in a uniform flow develop no lift. Therefore, the lift on a straight portion of a body on which a wing is mounted is due principally to lift transmitted from the wing to the body. A point on the wing is thought of as a source of lifting disturbances which move in all directions in the downstream Mach cone from the point. Some of these disturbances traverse the body. The assumption is made that the sole effect of the body (regardless of cross section) is to displace these pulses downstream without diminishing their lifting potential. This is the so-called delayed reaction of Lager-

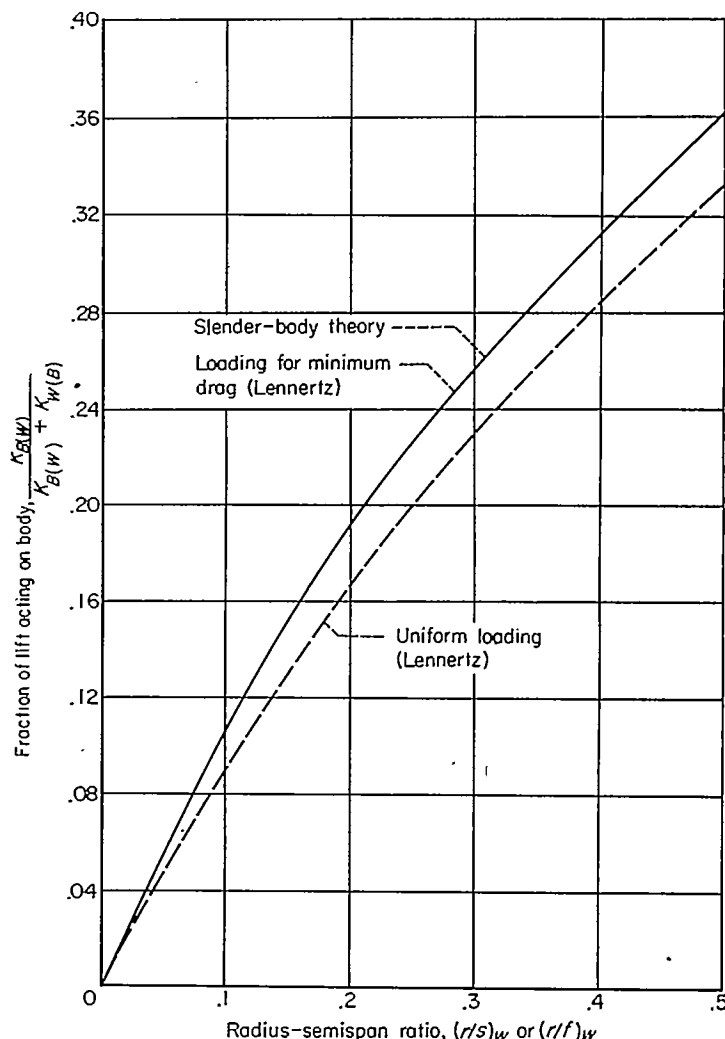


FIGURE 3.—Comparison of slender-body theory and theory of Lennertz for fraction of lift carried by body.

strom and Van Dyke in reference 19, which was substantiated for a particular family of rectangular wing-body combinations in reference 3. Downstream of the wing, the flow returns to the free-stream direction. The effect of this change in flow direction is felt on the surface of the afterbody behind the Mach helix originating at the trailing-edge, root-chord juncture. In this region, the reaction tends to cancel the lift transmitted from the wing onto the body. The effective resultant lifting area on the body for one half-wing can thus be approximated by the shaded area shown in figure 4(a).

While a nonplanar model has been set up to represent the lift transmitted to the body from the wing, further simplification to an equivalent planar case is desirable before calculations are performed. The body is imagined now to be collapsed to a plane and the Mach helices of figure 4(a) become the Mach lines of figure 4(b). The lifting area of the body is the shaded area of figure 4(b) which is at zero angle of attack. This area is equal to the horizontal projection of the lifting area of the actual body surface (fig. 4(a)). The lift on

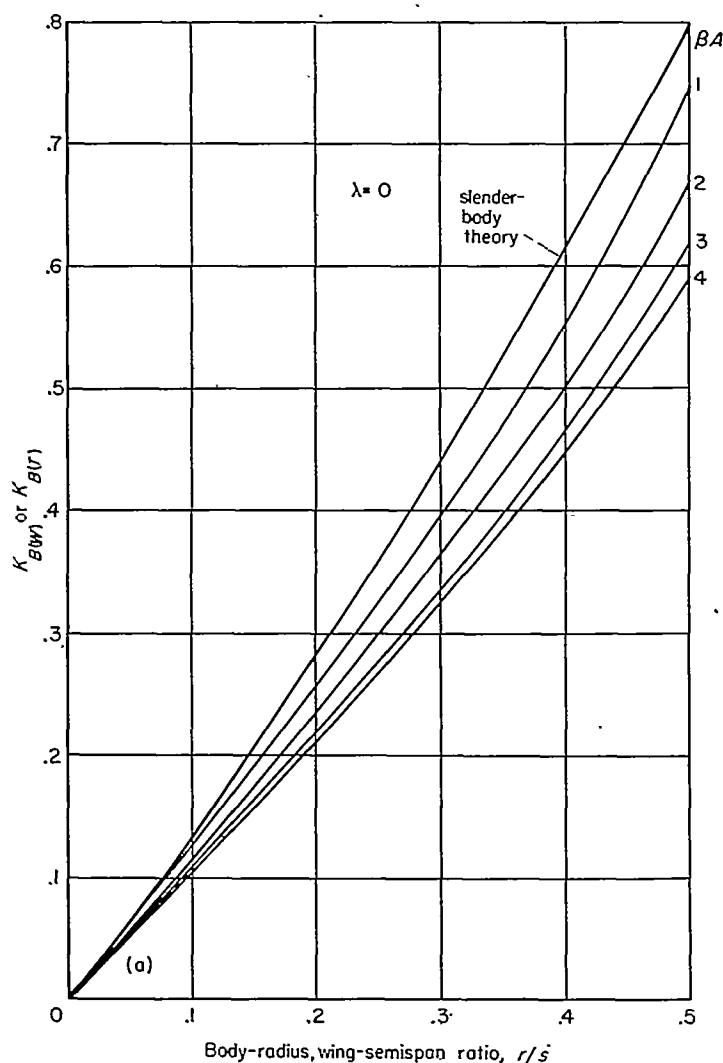


wings (fig. 5 (b)), and  $\lambda=1/2$  to trapezoidal wings (fig. 5 (c)). For triangular wings, the curve of  $K_{B(w)}$  by the present theory for  $\beta A=0$  is slightly greater than  $K_{B(w)}$  as given by slender-body theory and has not been included in the figures, since for such small values of  $\beta A$  slender-body theory is the more valid. Incidentally, the restriction of equation (22) is met by all triangular wings with no trailing-edge sweep. An examination of figure 5 (b) for rectangular wings shows good agreement between slender-body theory and the present theory at  $\beta A=2$ , the lowest aspect ratio for which the present theory is applicable to rectangular wings. In the case of the trapezoidal wings (fig. 5 (c)), the restriction of equation (22) imposes the condition that  $\beta A \geq 4/3$ . For a value of  $\beta A$  of  $4/3$  there is no appreciable difference between

slender-body  $K_{B(w)}$  and the value of  $K_{B(w)}$  by the present theory.

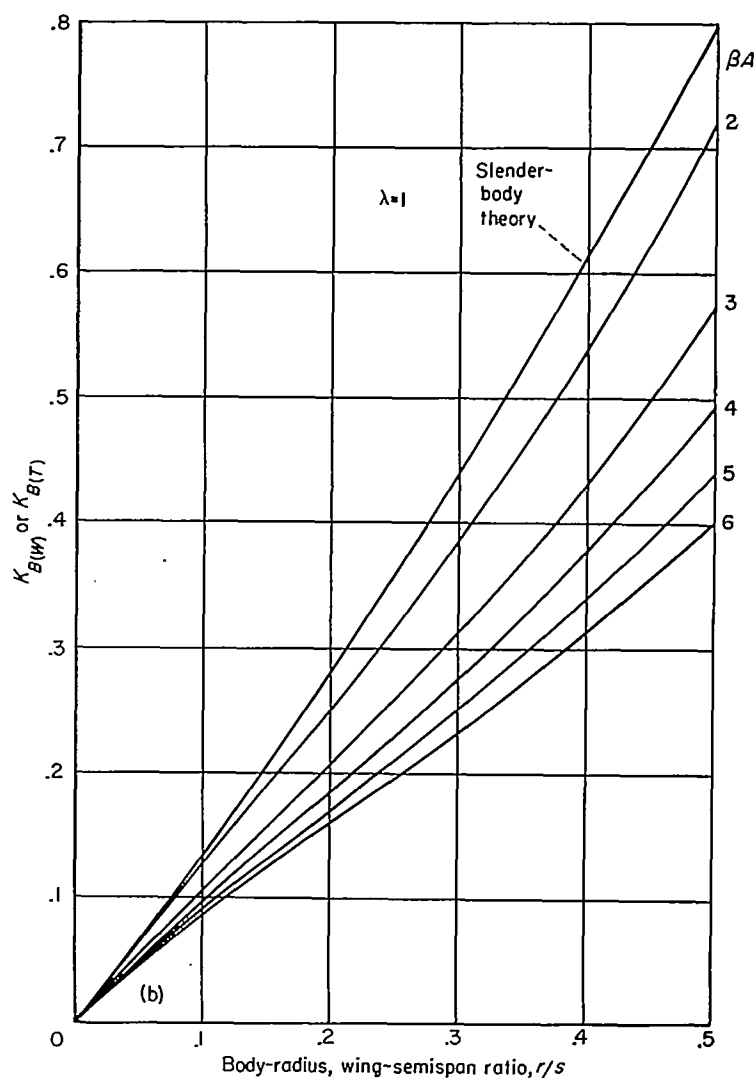
On the basis of figures 5 (a), 5 (b), and 5 (c), and since wing tip effects invalidate equations (24) and (26) for  $\beta A(1+\lambda)\left(\frac{1}{m\beta}+1\right) < 4$ , the following selection rule should be used: If  $\beta A(1+\lambda)\left(\frac{1}{m\beta}+1\right) \leq 4$ , use the slender-body theory  $K_{B(w)}$ ; and if  $\beta A(1+\lambda)\left(\frac{1}{m\beta}+1\right) > 4$ , use  $K_{B(w)}$  from chart 4.

Since rectangular and triangular wings are very common, and since  $(\beta C_{L\alpha})_w$  is known in closed form for these plan forms, specialized results can readily be obtained from



(a) Triangular wing-body combinations.

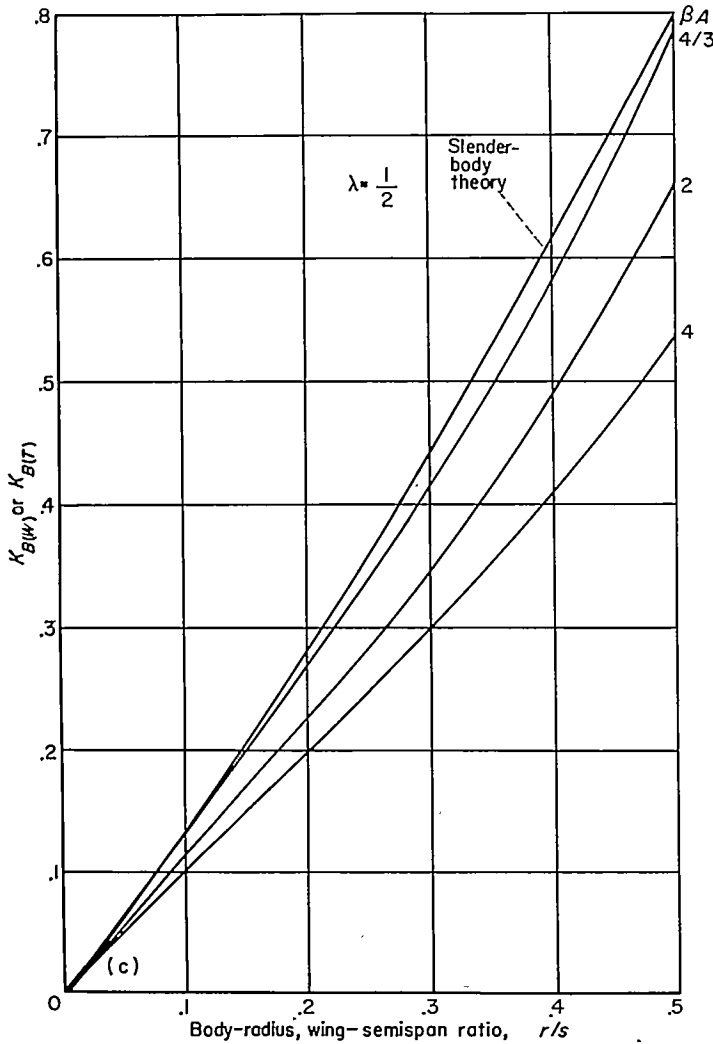
FIGURE 5.—Comparison of  $K_{B(w)}$  or  $K_{B(r)}$  determined by slender-body theory and present theory for wings with no trailing-edge sweep.



(b) Rectangular wing-body combinations.

FIGURE 5.—Continued.





(c) Trapezoidal wing-body combinations.

FIGURE 5.—Concluded.

equations (24) and (26) for  $K_{B(w)}$ . For rectangular wing-body combinations,  $K_{B(w)}$  is

$$K_{B(w)} = \frac{2}{\pi} \frac{1}{\left(\beta A - \frac{1}{2}\right)} \left\{ \frac{1}{2} \left[ 1 + \frac{\beta A \frac{r}{s}}{1 - \frac{r}{s}} \right]^2 \cos^{-1} \left[ \frac{\beta A}{\beta A + \frac{s}{r} - 1} \right] - \frac{1}{2} \left[ \frac{\beta A \frac{r}{s}}{1 - \frac{r}{s}} \right]^2 \cosh^{-1} \left[ 1 + \frac{1 - \frac{r}{s}}{\beta A \frac{r}{s}} \right] - \frac{1}{2} \frac{\pi}{4} + \frac{1}{2} \sqrt{1 + \frac{2\beta A \frac{r}{s}}{1 - \frac{r}{s}}} \right\} \quad (27)$$

For triangular wing-body combinations with subsonic leading edges,  $K_{B(w)}$  is

$$K_{B(w)} = \frac{8E \left( \sqrt{1 - \left(\frac{\beta A}{4}\right)^2} \right)}{\pi^2 \left(\frac{\beta A}{4}\right)^2} \left\{ \frac{\left(\frac{\beta A}{4}\right)^2}{2 \left(\frac{\beta A}{4} + 1\right)^2} \left[ 1 + \frac{2 \left(1 + \frac{\beta A}{4}\right) \frac{r}{s}}{1 - \frac{r}{s}} \right]^{\frac{3}{2}} - \left(\frac{\beta A}{\beta A + 4}\right)^2 + \frac{\left(\frac{\beta A}{4}\right)^2}{2 \left(\frac{\beta A}{4} + 1\right)^2} \left[ 1 + \frac{2 \left(1 + \frac{\beta A}{4}\right) \frac{r}{s}}{1 - \frac{r}{s}} \right]^{\frac{3}{2}} - 2 \left(\frac{\beta A}{4}\right)^2 \left[ \frac{\frac{r}{s}}{1 - \frac{r}{s}} \right]^2 \tanh^{-1} \sqrt{1 + \frac{2 \left(1 + \frac{\beta A}{4}\right) \frac{r}{s}}{\left(1 - \frac{r}{s}\right)}} \right\} \quad (28)$$

and for supersonic leading edges

$$K_{B(w)} = \frac{1}{\pi \sqrt{\left(\frac{\beta A}{4}\right)^2 - 1}} \left\{ \left(\frac{\beta A}{\beta A + 4}\right) \left[ 1 + \frac{2 \left(1 + \frac{\beta A}{4}\right) \frac{r}{s}}{1 - \frac{r}{s}} \right]^2 \cos^{-1} \left[ \frac{1 + \frac{\beta A}{2} \left(1 + \frac{\beta A}{4}\right) \frac{r}{s}}{1 - \frac{r}{s}} \right] + \frac{\sqrt{\left(\frac{\beta A}{4}\right)^2 - 1}}{\left(1 + \frac{\beta A}{4}\right)} \sqrt{1 + \frac{\beta A \frac{r}{s}}{1 - \frac{r}{s}}} - \frac{\beta A}{4} + \frac{\left(1 + \frac{\beta A}{4}\right) \frac{\beta A}{2} \left(\frac{r}{s}\right)}{1 - \frac{r}{s}} \right\} \\ + \frac{\frac{\beta A}{4}}{1 + \frac{\beta A}{4}} \cos^{-1} \frac{4}{\beta A} \sqrt{\left(\frac{\beta A}{4}\right)^2 - 1} \times \beta A \frac{\left(\frac{r}{s}\right)^2}{\left(1 - \frac{r}{s}\right)^2} \cosh^{-1} \left[ 1 + \frac{2 \left(1 - \frac{r}{s}\right)}{\beta A \frac{r}{s}} \right] - \frac{\sqrt{\left(\frac{\beta A}{4}\right)^2 - 1}}{\left(\frac{\beta A}{4} + 1\right)} \right\} \quad (29)$$

The case for no afterbody behind the wing can also be calculated for the high-aspect-ratio range at supersonic speeds. The method for determining  $K_{B(W)}$  without afterbody is the same as with afterbody except that the upper limit of integration in equations (23) and (25) is  $c_r$  rather than  $c_r + \beta\eta$ . Carrying out these integrations multiplying by 2 and dividing by the lift of the wing alone yields for the case of no afterbody

$$K_{B(W)} [\beta(C_{L_a})_W] (\lambda + 1) \left( \frac{s}{r} - 1 \right) =$$

$$\frac{8}{\pi \sqrt{\beta^2 m^2 - 1}} \left( \frac{\beta d}{c_r} \right) \left[ \left( 1 + \frac{m c_r}{d} \right)^2 \cos^{-1} \left( \frac{m \beta + \frac{c_r}{\beta d}}{1 + \frac{m c_r}{d}} \right) - \right.$$

$$m^2 \beta^2 \left( \frac{c_r}{\beta d} \right)^2 \cos^{-1} \left( \frac{1}{m \beta} \right) + m \beta \left( \frac{c_r}{\beta d} \right)^2 \sqrt{m^2 \beta^2 - 1} \sin^{-1} \frac{\beta d}{c_r} -$$

$$\left. \sqrt{m^2 \beta^2 - 1} \cosh^{-1} \frac{c_r}{\beta d} \right]; \beta m > 1, \frac{c_r}{\beta} > d \quad (30)$$

$$K_{B(W)} [\beta(C_{L_a})_W] (\lambda + 1) \left( \frac{s}{r} - 1 \right) =$$

$$\frac{16 \sqrt{m \beta}}{\pi (m \beta + 1)} \left( \frac{\beta d}{c_r} \right) \left\{ \left( 1 + \frac{m c_r}{d} \right) \sqrt{\left( \frac{c_r}{\beta d} - 1 \right) \left( \frac{m c_r}{d} + 1 \right)} - \right.$$

$$\left( \frac{c_r}{\beta d} \right)^2 (m \beta)^{3/2} + m \beta \left( \frac{c_r}{\beta d} \right)^2 (\beta m + 1) \left[ \tan^{-1} \sqrt{\frac{1}{\beta m}} - \right.$$

$$\tan^{-1} \sqrt{\left( \frac{c_r}{\beta d} - 1 \right) \left( \frac{m c_r}{d} + 1 \right)} \left. \right] - \frac{(m \beta + 1)}{\sqrt{m \beta}} \tanh^{-1}$$

$$\sqrt{m \beta \left( \frac{c_r}{\beta d} - 1 \right) \left( \frac{m c_r}{d} + 1 \right)} \left. \right\}; \beta m < 1, \frac{c_r}{\beta} > d \quad (31)$$

The restriction that  $\frac{c_r}{\beta} > d$  is not a serious one. For  $d > \frac{c_r}{\beta}$  it is clear that the lift transmitted to the body is the same as for  $d = \frac{c_r}{\beta}$  so that  $K_{B(W)}$  is constant. The value of the parameter  $K_{B(W)} [\beta(C_{L_a})_W] (\lambda + 1) \left( \frac{s}{r} - 1 \right)$  is plotted as a function of  $m \beta$  and  $2 \beta r / c_r$  in chart 4 (b).

A comparison of  $K_{B(W)}$  as determined from chart 4 (a) with that from chart 4 (b) gives an indication of the importance of the afterbody for any particular configuration. For small values of the ratio  $2 \beta (r/c_r)_W$  there is very little effect of the afterbody on  $K_{B(W)}$  but, for large values, the effect can be as large as several hundred percent. At subsonic speeds no distinction is made between the afterbody and no-afterbody cases. The difference between the two, which is usually small in terms of total lift at supersonic speeds, is further reduced at subsonic speeds because of the lesser tendency of lift to be carried downstream.

**Wing-incidence angle.**—From equation (7)

$$C_{L_{B(W)}} = k_{B(W)} (C_{L_a})_W \delta_W \quad (32)$$

The only general method for determining  $k_{B(W)}$  is slender-body theory. It has been shown in reference 22 by use of a

reciprocal theorem that for combinations with cylindrical bodies the following equality is valid under the assumptions of slender-body theory:

$$k_{B(W)} = K_{W(B)} - k_{W(B)} \quad (33)$$

The values of  $k_{B(W)}$  as given by equation (33) are included in chart 1.

An interesting approximation that gives some insight into the interrelationships between  $K_{B(W)}$ ,  $K_{W(B)}$ ,  $k_{B(W)}$ , and  $k_{W(B)}$  can be made. If it is assumed that the wing transmits a certain fraction of its lift to the body irrespective of whether the lift is developed by angle of attack or wing-incidence angle, an approximate value for  $k_{B(W)}$ , namely,  $k'_{B(W)}$ , is

$$k'_{B(W)} = k_{W(B)} \frac{K_{B(W)}}{K_{W(B)}} \quad (34)$$

The values of  $k_{B(W)}$  and  $k'_{B(W)}$  as determined from equations (33) and (34) do not differ by more than 0.01, a quantity that is practically indistinguishable in chart 1. This small difference is due to the difference in the forms of the load distribution on the wing for lifts due to angle of attack and wing-incidence angle.

#### LIFT ON TAIL SECTION DUE TO WING VORTICES

Wing-tail interference results from downwash in the region of the tail caused by the wing vortices. The problem of determining wing-tail interference breaks down into the problems, first, of determining the number, strengths, and positions of the wing vortices at the tail and, second, of determining the reaction of the tail section to the nonuniform flow field induced by the wing vortices. This component of the combination lift is the most laborious to calculate. The same method is used for subsonic and supersonic speeds.

Line-vortex theory is used in the solution of the wing-tail interference problem following the general lines of other investigators. The model to be used is illustrated in figures 6 and 7. This model of the wing is the same as the Lennertz model for uniform loading previously discussed and is thus compatible with the method used here for calculating wing-body interference. Only one trailing vortex per wing panel is considered although more vortices per panel could be used to obtain greater accuracy at the expense of greater complication. The wing trailing vortices stream backward but undergo lateral and vertical deflections as a result of the body crossflow field and the interaction between vortices. Image vortex lines are introduced inside the body at the image position of the trailing vortices to satisfy the boundary condition for a circular body. Sufficiently far downstream the external vortices approach an asymptotic spacing.

**Vortex characteristics.**—For ease of calculation it is assumed that one fully rolled-up vortex is discharged from each wing panel. While this model simulates the flow behind the wing panels of many combinations, there are cases where it does not. As examples, some results obtained by Spahr and Dickey in the Ames 1- by 3-foot supersonic wind tunnel are presented as the solid curves in figures 8, 9, and 10. These data were obtained by the vapor-screen technique described in reference 15. Figure 8 shows that for a

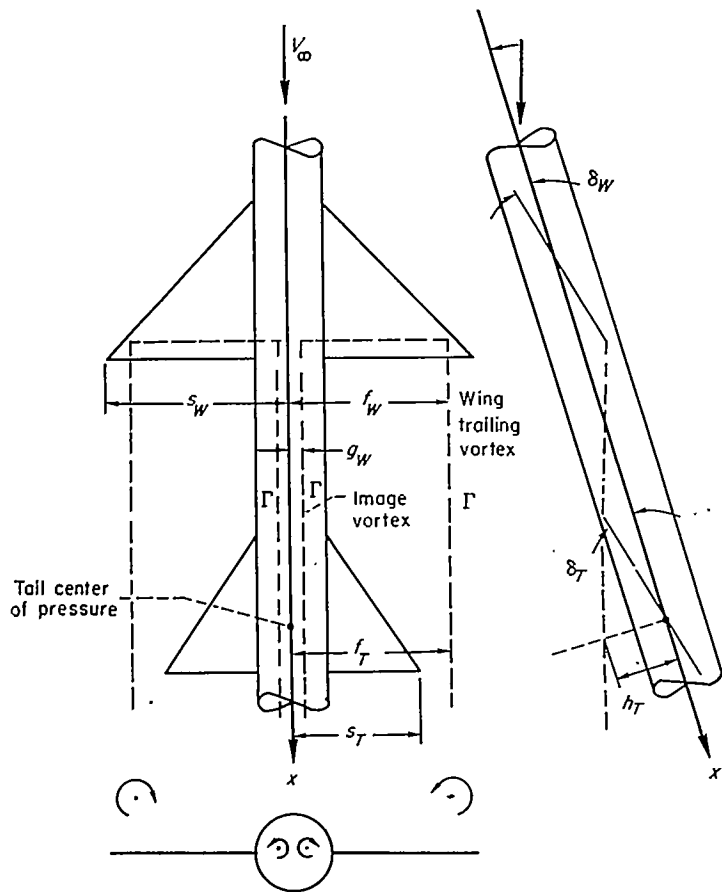


FIGURE 6.—Vortex model used in determination of wing-tail interference.

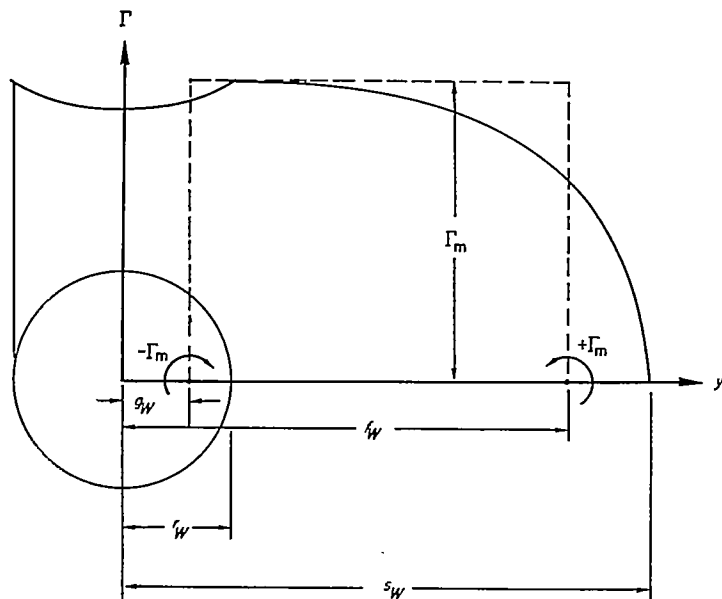


FIGURE 7.—Circulation distribution at wing trailing edge and equivalent horseshoe vortex.

low-aspect-ratio triangular wing in combination with a body at low angles of attack, only one tip vortex is present as assumed. However, as the angle of attack is increased a body vortex appears, and as the wing aspect ratio is increased (figs. 9 and 10) an additional vortex appears from the inboard sections of the wing. Thus, the simplified model of one vortex per wing panel is not always an adequate basis for

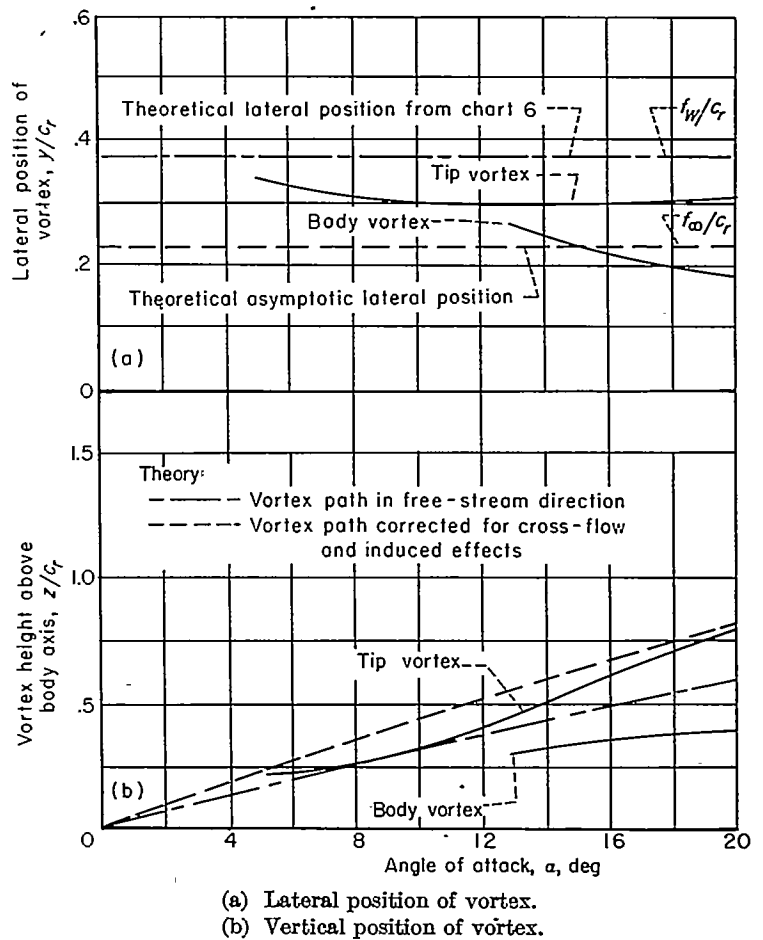


FIGURE 8.—Comparison between theory and experiment for lateral and vertical positions of wing vortex 1.8  $c_r$  behind wing of aspect ratio 2/3 triangular wing and body combination;  $M_\infty=2.0$ ,  $r/s=0.60$ .

computing downwash. However, several investigators have successfully applied this simplified model to the computation of tail loads. These results indicate that the total tail load of each of the configurations investigated is insensitive to the details of the vortex flow although the downwash behind the wing and the spanwise distribution of tail load are not. This conjecture is substantiated in part by the theoretical work of Morikawa, reference 9, who has calculated the tail lifts of slender wing-body-tail combinations using one fully rolled-up vortex per wing panel and using a flat vortex sheet. Only for fully rolled-up vortices in the immediate vicinity of the tail tip does any appreciable difference between the two cases occur. The results of Lomax and Byrd, reference 10, for a family of swept wing-body-tail combinations are in accord with the findings of Morikawa. It was on the basis of this evidence and because of its great simplicity that the use of one wing vortex per panel was adopted. The adequacy of this assumption and its range of application is subsequently determined by comparison between experiment and theory.

The circulation distribution at the wing trailing edge determines the strength  $\Gamma_m$  and the spanwise position  $f_W$  of the vortex at the trailing edge. The actual circulation distribution is replaced by an equivalent horseshoe vortex corresponding to the Lennertz model for uniform loading. Figure 7 illustrates this model. Note that figure 7 contains the tacit assumption that the maximum value of the circu-

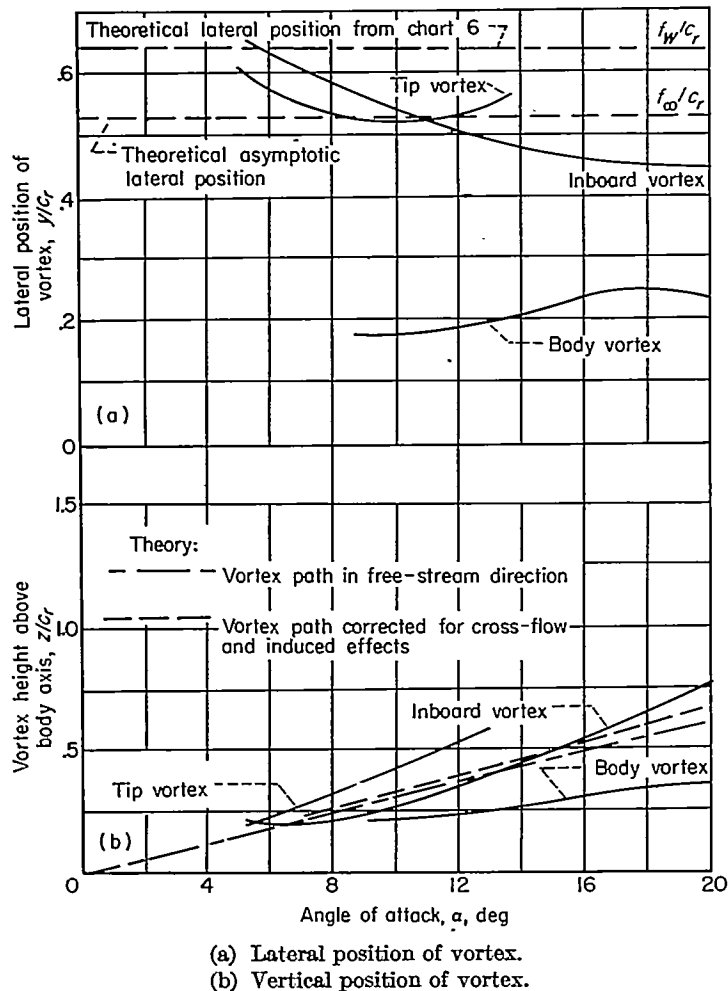


FIGURE 9.—Comparison between theory and experiment for lateral and vertical positions of wing vortex  $1.8 c_r$  behind wing of aspect ratio 2 triangular wing and body combination;  $M_\infty=2.0$ ,  $r/s=0.33$ .

lation is at the wing-body juncture. Since the lift of the bound vortex is  $\rho_\infty V_\infty \Gamma_m$  per unit span, the value of  $\Gamma_m$  can be estimated from the following series of equations:

$$\Gamma_m = \frac{L_{W(B)}}{2\rho_\infty V_\infty (f_W - r_W)} = \frac{L_{B(W)}}{2\rho_\infty V_\infty (r_W - g_W)} = \frac{L_{W(B)} + L_{B(W)}}{2\rho_\infty V_\infty (f_W - g_W)} \quad (35)$$

To satisfy the boundary condition that the body is circular

$$f_W g_W = r_W^2 \quad (36)$$

The first form of equation (35) is used for determining  $\Gamma_m$ . Since

$$C_{L_{W(B)}} = [K_{W(B)}\alpha + k_{W(B)}\delta_W] (C_{L_a})_W \quad (37)$$

it follows that

$$\Gamma_m = \frac{V_\infty [K_{W(B)}\alpha + k_{W(B)}\delta_W]}{4(f_W - r_W)} (C_{L_a})_W S_W \quad (38)$$

The problem of determining the lateral positions of the wing vortices must be solved before the foregoing equation can be used to evaluate  $\Gamma_m$ . The assumption is made that the vortices of the wing in combination are discharged at the center of vorticity of the panels of the wing alone as

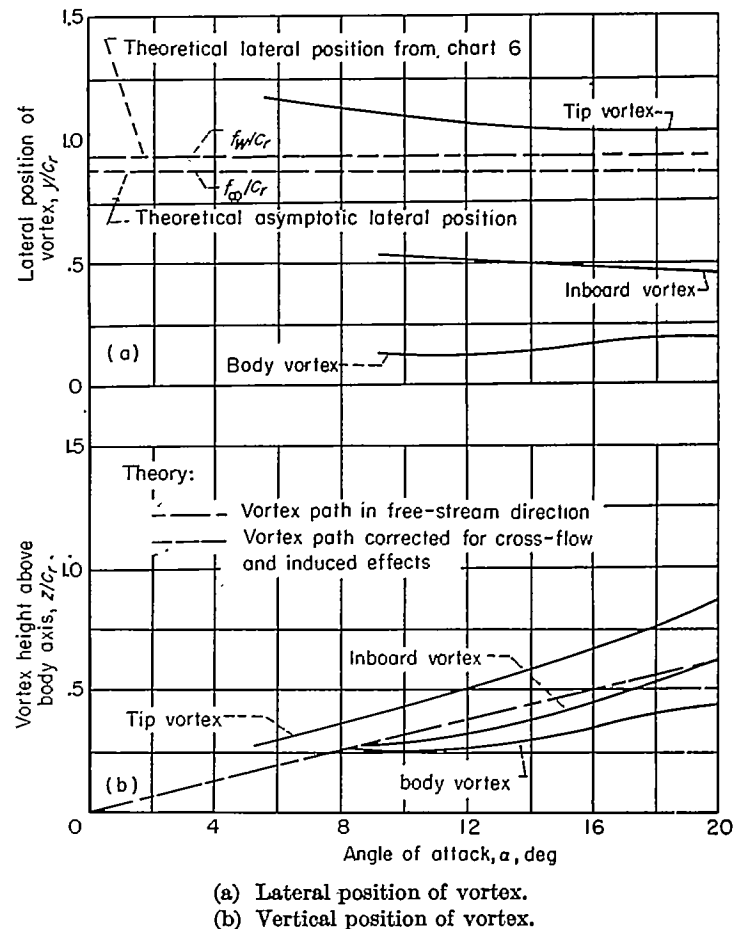


FIGURE 10.—Comparison between theory and experiment for lateral and vertical positions of wing vortex  $1.8 c_r$  behind wing of aspect ratio 4 triangular wing and body combination;  $M_\infty=2.0$ ,  $r/s=0.20$ .

determined by lifting-line theory or linear theory. This assumption is necessary because the circulation distribution is not generally known for the wing-body combination. The validity of this assumption can be examined for slender wing-body combinations for which the span loading is known and from which the lateral position of the vortex can be determined. In fact, the lateral vortex position on the basis of slender-body theory is

$$\left(\frac{f-r}{s-r}\right)_W = \frac{\frac{\pi}{4} \frac{\pi}{4} \left(\frac{r}{s}\right)_W^2 - \left(\frac{r}{s}\right)_W + \frac{\left[1 + \left(\frac{r}{s}\right)_W^2\right]^2}{2 \left[1 - \left(\frac{r}{s}\right)_W^2\right]} \sin^{-1} \left[ \frac{1 - \left(\frac{r}{s}\right)_W^2}{1 + \left(\frac{r}{s}\right)_W^2} \right]}{2 \left[1 - \left(\frac{r}{s}\right)_W^2\right]} \quad (39)$$

This equation gives the lateral position of the vortex as a fraction of the semispan of the exposed wing panel and as a function of the radius-semispan ratio. The maximum deviation between the values given by this equation and the wing-alone value of 0.786 (or  $\pi/4$ ) is about 3 percent. This result is independent of the plan form of the wing or body in front of the maximum span position since in slender-body theory the potential and, hence, the circulation depends only on the crossflow plane under consideration.

For nonslender wing-body combinations the lateral position can easily be determined if the lift coefficient and

the loading at the root chord are known for the wing alone. The necessary equation is

$$f_w = \frac{(C_L)_w S_w}{2(c_x c)} \quad (40)$$

In this equation  $(c_x c)$  is the product of the section lift coefficient at the midsection of the wing and the chord at that position. Inherent in the equation is the assumption that the maximum circulation occurs at the midsection of the wing.

A series of charts has been prepared for wings of unswept leading edges, midchord lines, and trailing edges to give the vortex location as a fraction of the wing-alone semispan and as a function of the effective aspect ratio with taper ratio as parameter. Chart 5, for subsonic speeds, is based on results of DeYoung and Harper, reference 23. It is noteworthy that for low aspect ratios the lateral positions of the vortices all tend toward the slender-body value of  $\pi/4$ . No systematic set of lift charts similar to those of DeYoung and Harper is available for supersonic speeds. However, where linear-theory results are available, they were used to obtain the curves shown solid in chart 6. The solid curves have been continued as dashed curves to the slender-body value of  $\pi/4$  at zero aspect ratio for the cases in which it was felt that the extrapolation could be made safely. For the  $\lambda=0$  case with no leading-edge sweep, there is a possibility that the circulation distribution does not have its maximum at the center line of the wing as assumed in equation (40). The linear-theory solution for the load distribution for the reversed triangular wing is unknown for  $\beta A_w < 4$ .

While the foregoing charts give the vortex lateral position at the wing, the lateral position at the tail,  $f_T$ , is required for calculating wing-tail interference. The simplest assumptions would be to set  $f_T$  equal to  $f_w$  or  $f_\infty$ , the asymptotic vortex lateral position, as determined from reference 11. To determine which of these approximations is more accurate, both  $f_w$  and  $f_\infty$  are compared with the experimental lateral and vertical positions of the wing-tip vortex in figures 8 (a), 9 (a), and 10 (a). On the basis of this comparison and because of the occurrence of the additional vortices, neither  $f_w$  nor  $f_\infty$  is superior for predicting the vortex spacing at the tail. Until more data are available on vortex positions to justify a more elaborate estimate, the value of  $f_w$  from charts 5 and 6 or reference 24 can be used for  $f_T$ .

The vertical position of the vortex at the tail can be estimated by the step-by-step calculative procedure described in reference 25, but the process is generally too lengthy. Two alternate methods are considered. In the first, the vortex is assumed to stream backward in the free-stream direction from the wing trailing edge. The second method, suggested by Lagerstrom and Graham, reference 11, is to ignore the effects of the image vortices, which are nearly equal and opposite, but to consider crossflow and the mutual effects of the external vortices. A comparison between the two positions predicted by these methods and the positions measured by Spahr and Dickey are shown in figures 8 (b), 9 (b), and 10 (b). Because of the occurrence of more than one wing vortex per panel and of body vortices, neither theoretical method appears superior. Therefore, it seems best to use the simpler

of the two methods which assumes that the vortices stream back from the trailing edge in the free-stream direction. This assumption leads to the following equation for vortex vertical location:

$$h_T = -(c_T - x_h)_w \sin \delta_w + [l_T + \bar{x}_T - l_w - (c_T)_w] \sin \alpha \quad (41)$$

The height is measured above the body axis and normal to it at the center of pressure of the tail panels.

**Lift due to wing vortices.**—For estimating the loads on the tail section, strip theory is generally applicable but the method of Alden and Schindel, reference 12, can be applied when the necessary theoretical span loadings are known. In specifying the tail load, use is made of a tail interference factor

$$i = \frac{L_T(\gamma)/(L_T)_\alpha}{\Gamma_m/2\pi\alpha V_\infty (s_T - r_T)} \quad (42)$$

where  $(L_T)_\alpha$  is the lift of the tail alone at angle of attack  $\alpha$ . The interference factor represents a nondimensional quantity useful for computing tail loads. The factor  $i$  depends on the parameters  $\lambda_T$ ,  $(r/s)_T$ ,  $(c/\beta s)_T$ ,  $(f/s)_T$ , and  $(h/s)_T$ . For a fixed body-tail configuration, the factor depends only on the vortex positions in the crossflow plane of the tail.

Whether the factor  $i$  is calculated by strip theory or by the Alden-Schindel technique, several simplifying assumptions are required regarding the wing-tail interference. The first assumption is one already used in determining  $K_{B(w)}$  for large aspect ratios at supersonic speeds—that the nonplanar tail section can be reduced to an equivalent planar model similar to that shown in figure 4. The body is assumed to be flat and to act at zero angle of attack, while the tail angle of attack  $\alpha_T$  varies spanwise. The second assumption is that the lift on the tail section due to wing-tail interference is all developed by the tail panels, even though part of it is transferred to the body. In the application of strip theory to determine this lift, Lagerstrom and Van Dyke in reference 19 have shown that an exact value (within the realm of linear theory) is obtained for the over-all lift of the planar model if the leading edge is supersonic and the trailing edge is straight, as for a triangular wing of effective aspect ratio greater than 4. It is to be noted that the second assumption circumvents the question of whether an afterbody occurs behind the tail. Generally, the lift acting on the body is only a small fraction of that acting on the tail section due to wing-tail interference, so that no precise consideration of the tail afterbody is usually required.

Strip theory has been used to calculate a series of design charts for the estimation of  $i$ . The details of the calculations are given in Appendix B, and the results are presented in chart 7. These charts show contours of constant values of  $i$  in the crossflow plane of the tail with the parameters  $\lambda_T$  and  $(r/s)_T$  varying from chart to chart. It is to be noted that strip theory is independent of the chord-span ratio  $(c/\beta s)_T$ . In fact, strip theory represents the limiting case of linear theory as  $(c/\beta s)_T \rightarrow 0$ . The charts give an immediate idea of the regions wherein wing-tail interference is most important. For triangular tails ( $\lambda_T = 0$ ) it is to be noted that the interference is a finite maximum when the vortex

is in the plane of the tail and slightly inboard of the tip. For all other taper ratios, however, an infinite maximum effect occurs when the vortex is at the tail tip. Strip theory is, thus, not accurate for positions of the vortex near the tail tip, except in the case of triangular wings with supersonic leading edges, in which case it is accurate to the order of linear theory.

An alternate method for the determination of  $i$  is the method of Alden and Schindel, which serves as a basis for assessing the accuracy of strip theory. The essential result of the method is that the lift of a lifting surface with supersonic edges in a nonuniform flow field that varies spanwise can be evaluated to the accuracy of linear theory by the equation

$$L = \int_{\text{span}} w(y) F(y) dy \quad (43)$$

where  $w(y)$  is the vertical velocity at the spanwise position  $y$  and  $F(y)$  is proportional to the span loading of the tail at uniform angle of attack in reversed flow. Heaslet and Spreiter in reference 22 have extended the range of equation (43) to include surfaces with subsonic edges. For triangular tails with supersonic leading edges, the reversed tail is uniformly loaded so that  $F(y)$  is proportional to the local chord. Thus, strip theory and the Alden-Schindel method give identical results for this case. Generally speaking, the Alden-Schindel technique is not suited for an analytical determination of  $i$  because, in some cases, the necessary function  $F(y)$  is not known or leads to complicated integrations. The Alden-Schindel method leads to results in closed form for rectangular tail and body combinations, and the calculation has been carried out in Appendix C. The values of  $i$  for the vortex in the plane of a rectangular tail and for a radius-semispan ratio of 0.2 are given in figure 11 for four values of  $(c/\beta s)_T$ . For a value of  $(c/\beta s)_T = 0$  the Alden-Schindel technique and strip theory are identical. Thus, a comparison of the curves for other values of  $(c/\beta s)_T$  with those for zero gives an indication of the error due to the use of strip theory for large chord-span ratios. The first result is that the infinity at  $(f/s)_T = 1$  (for values of

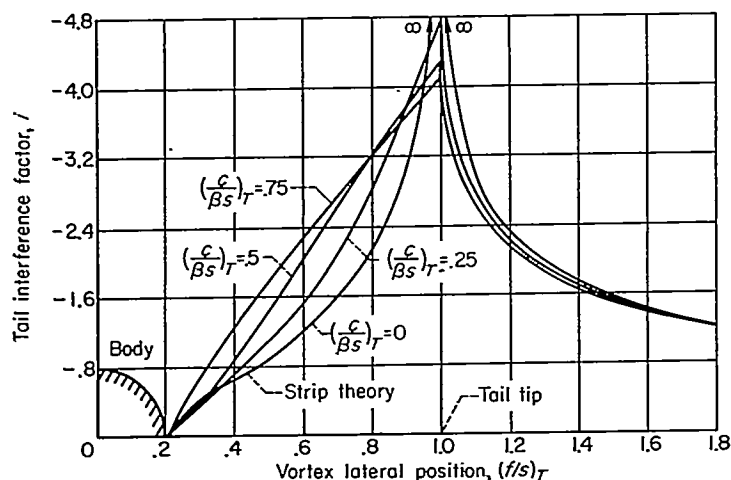


Figure 11.—Effect of chord-span ratio on lift of rectangular tail due to wing vortex as determined by Alden-Schindel technique for vortex in plane of tail;  $(r/s)_T = 0.2$ .

$(c/\beta s)_T$  not equal to zero) has been eliminated by using the Alden-Schindel technique. For vortex positions outboard of the tail tip, the effect of  $(c/\beta s)_T$  is very small. However, for vortex positions inboard of the tip, a larger effect of  $(c/\beta s)_T$  is indicated. To obtain an idea of where the discrepancy due to the use of strip theory is large and where small, a figure has been prepared showing the ratio of  $(i_{AS} - i_{ST})/i_{AS}$  as a measure of the error incurred in using strip theory for  $(c/\beta s)_T = 0.5$ . This ratio is shown as a function of vortex position in figure 12. For positions of the

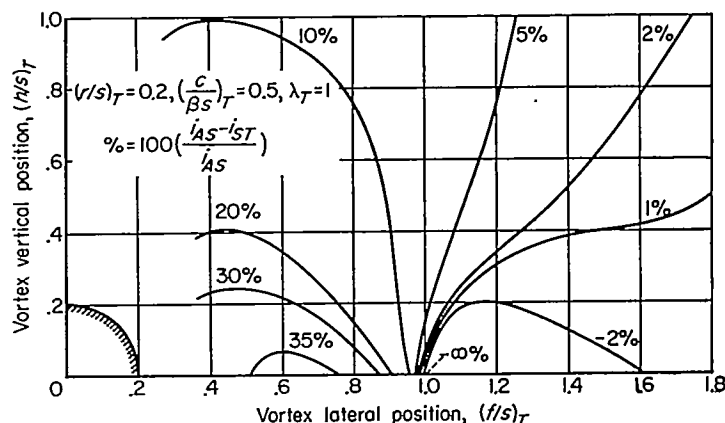


FIGURE 12.—Error due to use of strip theory in estimation of loads on rectangular tail section due to wing vortices.

vortex outboard of the tail tip, the error is generally very small except in the immediate vicinity of the tip. For positions of the wing vortex inboard of the tail tip, a maximum error of about 35 percent can be incurred by the use of strip theory. This error decreases with increasing vortex distance from the tail. The reason that larger errors are incurred for positions of the vortex inboard of the tail tip is that here the net effect of the vortex is the small difference of large positive and negative lifts, while for outboard positions the vortex induces negative lift across the entire tail. It is believed that the use of strip theory is more accurate for tapered wings than for rectangular wings since it is known to be exact for triangular wings with supersonic edges. Despite the fact that strip theory does not possess the accuracy of linear theory for purposes of estimating tail loads, it has several decisive advantages over the linear theory (exemplified at supersonic speeds by the Alden-Schindel method). First, the necessary theoretical information is not available for using linear theory in some cases at supersonic speeds. Second, separate determinations would be required for different  $(c/\beta s)_T$  values and for subsonic and supersonic speeds, making the construction of design charts extremely difficult. For these reasons and because of its great simplicity, strip theory is used in this report for computing the tail interference factors except for rectangular tails at supersonic speeds.

The contribution of wing-tail interference to the lift coefficient is now derived. The contribution is by definition

$$C_{L_{T(V)}} = \frac{L_{T(V)}}{q_\infty S_W} \quad (44)$$

with the aid of equations (38) and (42) there is obtained

$$C_{L_{T(V)}} = \frac{(C_{L_a})_W (C_{L_a})_T [K_{W(B)}\alpha + k_{W(B)}\delta_W] i(s_T - r_T)}{2\pi A_T (f_W - r_W)} \quad (45)$$

The values of  $K_{W(B)}$  and  $k_{W(B)}$  are obtained from chart 1, the value of  $i$  from chart 7, and the value of  $f_W$  from chart 5 or 6. For rectangular tails at supersonic speeds the value of  $i$  calculated by use of the Alden-Schindel technique is recommended.

#### LIFT ON WING AFTERBODY DUE TO WING VORTICES

In the previous work it was assumed that no change in lateral vortex spacing occurred between the wing and tail because, for the purposes of this report, the extra work to compute the change is usually not warranted. However, if for some reason a step-by-step calculation of the vortex path is made, the lift on the wing afterbody can be estimated. The model shown in figure 6 is used in the estimation. The lift represented by a horseshoe vortex is  $\rho_\infty V_\infty \Gamma_m$  per unit span. The lift represented by the vortex system at the wing trailing edge is thus  $2\rho_\infty V_\infty \Gamma_m (f_W - g_W)$  and at the tail location is  $2\rho_\infty V_\infty \Gamma_m (f_T - g_T)$ . The net lift retained on the body between the wing and the tail is thus

$$L_{B(V)} = -2\rho_\infty V_\infty \Gamma_m [(f_W - g_W) - (f_T - g_T)] \quad (46)$$

With the aid of the relationships

$$g_W = \frac{r_W^2}{f_W} \quad (47)$$

$$g_T = \frac{r_T^2}{\sqrt{f_T^2 + h_T^2}} \quad (48)$$

equation (46) becomes in lift coefficient form

$$C_{L_{B(V)}} = -\frac{4\Gamma_m}{S_W V_\infty} \left[ \frac{(f_W^2 - r_W^2)}{f_W} - f_T + \frac{r_T^2}{\sqrt{f_T^2 + h_T^2}} \right] \quad (49)$$

Lagerstrom and Graham (ref. 11) have derived this same result using a different method. Generally, the change in  $f$  between wing and tail is not known unless the step-by-step solution mentioned in reference 25 is performed. In this case both the total lift and distribution of lift on the body due to the trailing vortices is known. However, if only an upper bound on the value of  $C_{L_{B(V)}}$  is desired, then the value of  $f_\infty$  can be used for  $f_T$  in equation (49).

#### SUMMARY OF LIFT COMPONENTS OF WING-BODY-TAIL COMBINATIONS

The seven components of the lift acting on a wing-body-tail combination are outlined as follows:

1. Lift on body nose,

$$(C_L)_N = K_N (C_{L_a})_W \alpha \quad (50)$$

2. Lift on wing in presence of body,

$$(C_L)_{W(B)} = [K_{W(B)}\alpha + k_{W(B)}\delta_W] (C_{L_a})_W \quad (51)$$

3. Lift on body due to wing,

$$(C_L)_{B(W)} = [K_{B(W)}\alpha + k_{B(W)}\delta_W] (C_{L_a})_W \quad (52)$$

4. Lift on tail in presence of body (neglecting wing vortices),

$$(C_L)_{T(B)} = [K_{T(B)}\alpha + k_{T(B)}\delta_T] (C_{L_a})_T \left( \frac{S_T}{S_W} \right) \quad (53)$$

5. Lift on body due to tail (neglecting wing vortices),

$$(C_L)_{B(T)} = [K_{B(T)}\alpha + k_{B(T)}\delta_T] (C_{L_a})_T \left( \frac{S_T}{S_W} \right) \quad (54)$$

6. Lift on tail section due to wing vortices,

$$(C_L)_{T(V)} = \frac{(C_{L_a})_W (C_{L_a})_T [K_{W(B)}\alpha + k_{W(B)}\delta_W] i(s_T - r_T)}{2\pi A_T (f_W - r_W)} \quad (55)$$

7. Lift on wing afterbody due to wing vortices,

$$(C_L)_{B(V)} = -\frac{4\Gamma_m}{S_W V_\infty} \left[ \frac{(f_W^2 - r_W^2)}{f_W} - f_T + \frac{r_T^2}{\sqrt{f_T^2 + h_T^2}} \right] \quad (56)$$

An example of the use of these equations is presented in a subsequent numerical computation for a specific wing-body-tail combination. Chart 8, which summarizes the lift-curve slopes of wings at supersonic speeds as determined from linear theory, is included for use with these formulas.

#### LONGITUDINAL CENTER-OF-PRESSURE THEORY

In the section on lift theory the differences between subsonic and supersonic speeds were given only passing attention since the lift theory as developed applies in the same form to both speed ranges. The primary affect of Mach number was manifest through the quantities  $(C_{L_a})_W$  and  $(C_{L_a})_T$ . However, in the center-of-pressure theory the Mach number has a direct effect on the centers of pressure of several of the lift components, and a definite distinction must be made between the subsonic and supersonic cases for these components.

Several conventions are adopted with regard to center-of-pressure position in this report. All positions for the complete configuration are ultimately given in fractions of the body length behind the most forward point of the body. In the design charts, the centers of pressure of  $L_{B(W)}$ ,  $L_{W(B)}$ ,  $L_{T(B)}$ , and  $L_{B(T)}$  are given in fractions of the root chord behind the juncture of the leading edge with the body. All length symbols having bars over them represent center-of-pressure lengths.

#### CENTER OF PRESSURE OF BODY NOSE

For most purposes the center of pressure of the body nose can be estimated with sufficient accuracy by slender-body theory. The result is obtained that

$$\bar{l}_N = l_s \left( 1 - \frac{V_s}{\pi r_N^2 l_s} \right) \quad (57)$$

wherein  $V_s$  and  $l_s$  are the volume and length of that portion of the body nose forward of the shoulder. For bodies with noses of small fineness ratio or even for bodies with slender noses at high Mach numbers, some lift is carried over onto the body behind the nose, tending to make  $\bar{l}_N$  greater than the value given by equation (57). If the lift on the nose is a

substantial fraction of the total lift, the effect can be significant. In such cases linear theory is better than slender-body theory, although experimental values of  $\bar{l}_N$  are always preferred. In this report, the theoretical values used will be those of slender-body theory. The centers of pressure of ogival noses as determined from slender-body theory are presented in chart 9.

#### CENTER OF PRESSURE OF WING IN PRESENCE OF BODY

**Angle of attack.**—The center of pressure of a triangular wing in the presence of an infinite cylindrical body as given by slender-body theory (ref. 13), in percent of the exposed wing root chord measured from the leading edge of the wing-body juncture, is

$$\left(\frac{\bar{x}}{c_r}\right)_{W(B)\alpha} = \frac{1}{\left(1 - \frac{r}{s}\right)} \times \frac{2\left(\frac{1}{3} + \frac{r^4}{s^4}\right) \tan^{-1}\left(\frac{s}{r}\right) + \frac{2}{3} \frac{r^3}{s^3} \ln \left[ \frac{(s^2 + r^2)^2 \frac{s}{r}}{2s^2} \right] - \frac{1}{3} \frac{r^3}{s^3} \left(2\pi - 1 + \frac{s^2}{r^2}\right)}{\left(1 + \frac{r^2}{s^2}\right) \tan^{-1}\left(\frac{s}{r}\right) - \frac{r^2}{s^2} \left[ \pi + \left(\frac{s}{r} - \frac{r}{s}\right) \right]} \quad (58)$$

$$\frac{r}{s} \left(1 - \frac{r}{s}\right)$$

An alternate method for evaluating center-of-pressure location of a triangular wing-body combination is to suppose that the exposed wings are operating in the upwash field of the body alone and then to calculate the resultant center-of-pressure location using strip theory. The procedure to be followed is similar to that used in the lift-theory section. The upflow angle due to the body varies spanwise on the horizontal plane of symmetry as

$$\alpha_y = \alpha_B \left(1 + \frac{r^2}{y^2}\right) \quad (59)$$

where  $y$  is the lateral distance from the body axis. The wing is thus effectively twisted by the body-alone flow. If now the upwash angle given by equation (59) is taken into account by using strip theory, an approximate value of lift is given as

$$L_{W(B)\alpha} = \frac{4}{\beta} q_\infty \int_r^s \alpha_y c_y dy \quad (60)$$

The moment about the leading edge of the root chord is

$$M_{W(B)\alpha} = \frac{4}{\beta} q_\infty \int_r^s \alpha_y \bar{x}_y c_y dy \quad (61)$$

It is assumed that the center of pressure of the strip is at the midchord. Dividing moment by lift then gives for the center-of-pressure location for the wing of a triangular wing-body combination

$$\left(\frac{\bar{x}}{c_r}\right)_{W(B)\alpha} = \frac{1}{2} + \frac{\frac{1}{6} \frac{1}{2} \frac{r}{s} \frac{3}{2} \frac{r^2}{s^2} + \frac{11}{6} \frac{r^3}{s^3} + \left(1 + \frac{r}{s}\right) \frac{r^2}{s^2} \ln \frac{s}{r}}{2 \left(1 - \frac{r}{s}\right) \left[ \frac{1}{2} \left(1 - \frac{r^2}{s^2}\right) - \frac{r^2}{s^2} \ln \left(\frac{s}{r}\right) \right]} \quad (62)$$

The results of equations (58) and (62) are presented in figure 13 as a function of  $r/s$ . In addition, the value of center of pressure of the wing alone as determined by linear theory is indicated. It is significant that all three methods give essentially the same result for the center-of-pressure location of the wing in presence of the body. It may be concluded that  $(\bar{x}/c_r)_w$  for wing alone (defined as exposed wing panels joined together), although independent of  $r/s$ , gives a sufficiently accurate representation of  $(\bar{x}/c_r)_{W(B)}$  for triangular wings in presence of the body.

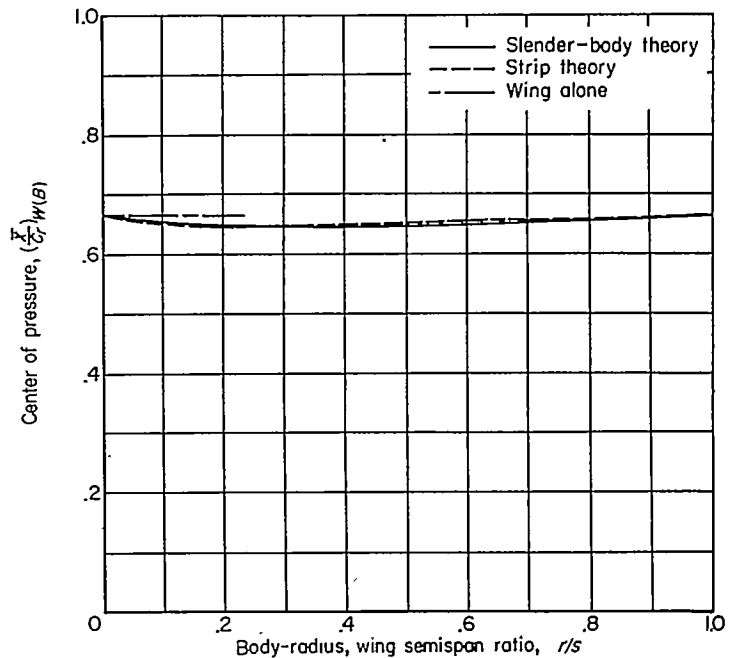


FIGURE 13.—Comparison of theoretical values of  $(\bar{x}/c_r)_{W(B)}$  for triangular wing with no trailing-edge sweep.

If slender-body theory is applied to rectangular wings in combination, the erroneous result is obtained that all lift, and therefore the center of pressure, is at the wing leading edge. While this result is valid for vanishing aspect ratio, it is obviously not valid in general. On the other hand, by strip theory, the center of pressure is given at the midchord and is independent of the aspect ratio. This value is exact only in the case of vanishing chord and is approximately true for moderate to high aspect ratios. The center-of-pressure location of wing alone as predicted by linear theory exhibits a shift toward the leading edge from the midchord position with decreasing aspect ratio.

$$\left(\frac{\bar{x}}{c_r}\right)_w = \frac{3\beta A - 2}{6\beta A - 3} \quad (63)$$

Equation (63) is valid for  $\beta A > 1$ . For  $\beta A < 1$ , negative lifting pressures due to tip effects develop on rearward areas of the wing, moving the center of pressure nearer the wing leading edge. Thus, the wing-alone center-of-pressure location as predicted by linear theory approaches the value given by strip theory for wings (in presence of body) of high aspect ratios and shows a location more in accordance with slender-body-theory results at low aspect ratios. It is therefore concluded that for rectangular wings the center of



pressure of the wing alone for all aspect ratios is more representative of the center of pressure of the lift on the wing in presence of a body than the result given by either slender-body theory or strip theory.

For trapezoidal wings of no trailing-edge sweep, slender-body theory gives all the lift, and hence center of pressure, on the portions of the wing forward of the leading edge of the tip chord. In general, however, lift is known to exist over the entire wing and the slender-body result for center-of-pressure location is too far forward at high aspect ratios. Strip theory, on the other hand, principally by not accounting for tip effects, generally gives a center-of-pressure location too far aft of the wing leading edge particularly at low aspect ratios. For large aspect ratios wing-alone theory is in good accord with strip theory, and at low aspect ratios, with slender-body theory. Since strip theory is reliable only at high aspect ratios, it can be concluded that wing-alone theory is best for the entire aspect-ratio range.

On the basis of the foregoing comparison of wing-alone theory with slender-body theory and strip theory for triangular, rectangular, and trapezoidal wings in combination with a body, it is concluded that of these three theories wing-alone theory is the best for representing the center of pressure of the exposed wing panels throughout the aspect-ratio range. Some simple charts to assist in estimating these center-of-pressure positions are now presented. For supersonic speeds, charts 10 (a), 10 (b), and 10 (c) give the variation of  $(\bar{x}/c_r)_w$  with  $\beta A$  for wings of no leading-edge sweep, no midchord sweep, and no trailing-edge sweep, respectively, for taper ratios of  $\lambda=0$ ,  $1/2$ , and 1. The curves giving  $(\bar{x}/c_r)_w$  are extrapolated to the limiting values given by slender-body theory at  $\beta A=0$ , for which case slender-body theory is valid. The value of  $(\bar{x}/c_r)_w$  for any given wing of this family can be found by suitable interpolation. For subsonic speeds the charts of DeYoung and Harper, reference 23, can be used for estimating  $(\bar{x}/c_r)_w$  for a wide range of aspect ratios, taper ratios, and sweep angles. The results are presented in chart 11. Again the results have been extrapolated from values of  $\beta A=2$  to the slender-body values at  $\beta A=0$ . Crossplotting aided in the extrapolation.

The distance from the most forward point of the body to the wing center of pressure is

$$\bar{l}_{w(B)\alpha} = l_w + (c_r)_w (\bar{x}/c_r)_{w(B)\alpha} \quad (64)$$

$$M_{B(W)} = \frac{4q_\infty \alpha_w m}{3\pi\beta} c_r^3 \left\{ \sqrt{1 + \frac{2\beta d}{c_r}} \left[ \frac{2m\beta + 5}{3(m\beta + 1)^2} + \frac{\beta d/c_r}{3(m\beta + 1)} - \frac{(\beta d/c_r)^2}{\beta m} \right] + \frac{1}{\sqrt{m^2\beta^2 - 1}} \left[ \left(1 + \frac{\beta d}{c_r}\right)^3 - \frac{(\beta d/c_r)^3}{m^2\beta^2} - \frac{1}{(1 + m\beta)^2} \right] \cos^{-1} \left[ \frac{1 + \frac{\beta d}{c_r}(m\beta + 1)}{m\beta + \frac{\beta d}{c_r}(m\beta + 1)} \right] + \left(\frac{\beta d}{c_r}\right)^3 \frac{1}{m^2\beta^2} \cosh^{-1} \left(1 + \frac{c_r}{\beta d}\right) - \left[ \frac{2m\beta + 5}{3(m\beta + 1)^2} - \frac{1 - \left(\frac{1}{m\beta + 1}\right)^2}{\sqrt{m^2\beta^2 - 1}} \right] \cos^{-1} \frac{1}{m\beta} \right\} \quad (67)$$

**Wing-incidence angle.**—No general method for estimating  $(\bar{x}/c_r)_{w(B)\delta}$  exists, but specialized results are available for rectangular wing and body combinations for which  $\beta A \geq 2$  or for slender triangular wing and body combinations. For the rectangular wing and body combinations, values of  $(\bar{x}/c_r)_{w(B)\delta}$  based on linear theory obtained from reference 3 are presented in chart 12. The values of  $(\bar{x}/c_r)_{w(B)\delta}$  are lower than the wing-alone ( $r/s=0$ ) values by a few percent of the root chord. The results for slender triangular-wing and body combinations as determined from slender-body theory in Appendix A are shown in chart 13. The deviation of  $(\bar{x}/c_r)_{w(B)\delta}$  from the wing-alone value of  $2/3$  is only a fractional percent of the root chord. For the combination to which they apply, the results of charts 12 and 13 are to be used. For other combinations,  $(\bar{x}/c_r)_w$  provides a good approximation to  $(\bar{x}/c_r)_{w(B)\delta}$  until more accurate values are available.

The center-of-pressure position with reference to the body is

$$\bar{l}_{w(B)\delta} = l_w + (c_r)_w (\bar{x}/c_r)_{w(B)\delta} \quad (65)$$

#### CENTER OF PRESSURE ON BODY DUE TO WING

The center of pressure acting on the body due to the wing is determined by different methods, depending on whether subsonic or supersonic flow is considered. The assumption is made that the center of pressure of the lift transferred from the wing to the body is not sensitive to whether the lift is developed by angle of attack or by wing deflection. Then there is no appreciable difference between  $(\bar{x}/c_r)_{B(W)\alpha}$  and  $(\bar{x}/c_r)_{B(W)\delta}$ , and these two cases are not treated separately.

**Supersonic flow.**—For the supersonic case the planar model of figure 4 is used. This is the same model that was used for the determination of the lift on the body in the presence of the wing. The moment of the lift (eq. (23)) carried onto the body by a wing with a supersonic leading edge is

$$M_{B(W)} = \frac{4q_\infty \alpha_w \beta m}{\beta \pi \sqrt{\beta^2 m^2 - 1}} \int_0^d d\eta \int_{\beta\eta}^{c_r + \beta\eta} \xi \cos^{-1} \frac{\xi + \beta m \eta}{\eta + m \xi} d\xi \quad (66)$$

in terms of the coordinate system of figure 4(b). This result, doubled to account for the lift of two half-wings, gives

The center-of-pressure location is then found using  $K_{B(W)}$  from equation (24) and the moment from equation (67) as follows:

$$\left(\frac{\bar{x}}{c_r}\right)_{B(W)} = \frac{M_{B(W)}}{L_{B(W)}c_r} = \frac{M_{B(W)}}{K_{B(W)}L_Wc_r} \quad (68)$$

$$M_{B(W)} = \frac{4q_\infty\alpha_W}{\pi\beta^2}c_r^3 \left\{ \frac{\sqrt{m^2\beta^2 + m\beta(m\beta+1)}\frac{\beta d}{c_r}}{9m\beta(m\beta+1)^3} \left[ (8m\beta+24)m^2\beta^2 + (14m\beta+6)(m\beta+1)m\beta\frac{\beta d}{c_r} + \right. \right. \\ \left. \left. 3(m\beta-3)(m\beta+1)^2\left(\frac{\beta d}{c_r}\right)^2 \right] - \frac{(8m\beta+24)m^3\beta^3}{9m\beta(m\beta+1)^3} - \frac{(m\beta-3)}{3m\beta}\left(\frac{\beta d}{c_r}\right)^3 \cosh^{-1} \sqrt{\frac{m\beta+(m\beta+1)\frac{\beta d}{c_r}}{(m\beta+1)\frac{\beta d}{c_r}}} \right\} \quad (70)$$

The moment of equation (70) with  $K_{B(W)}$  of equation (26) is used in equation (68) to give the center of pressure of the lift on an infinite cylindrical body due to the wing. The results for center of pressure for both supersonic and subsonic leading edges are presented as a function of  $\beta d/c_r$  with  $m\beta$  as the parameter in chart 14(a). It is notable that the effect of  $m\beta$  is small.

The case for no afterbody is approximated by integrating equations (66) and (69) with  $c_r$  as the upper limit. This is analogous to the determination of  $K_{B(W)}$  for the no afterbody case in the lift-theory section. The results for both supersonic and subsonic leading edges are presented in chart 14(b).

While chart 14 can be used for an approximation to  $(\bar{x}/c_r)_{B(W)}$  for the low-aspect-ratio range, a somewhat more accurate form can be presented for this range (chart 15). In the more accurate chart the independent variables are taken to be aspect ratio and taper ratio, with radius-semispan ratio as parameter. The values of  $(\bar{x}/c_r)_{B(W)}$  for  $\beta A=0$  are those given by slender-body theory, and the values for  $(r/s)=0$  are those for the wing alone as given by linear theory. On the basis of this information it is possible to extrapolate the high-aspect-ratio theory to  $\beta A=0$ , as has been done in chart 15 for the afterbody case. This is to serve as a design chart for the low-aspect-ratio range. A similar chart can easily be formulated for the no-afterbody case by use of the results of chart 14(b). In establishing the slender-body values at  $\beta A=0$ , it was assumed that no lift was developed downstream of the maximum wing span. The extrapolation was not attempted for  $\lambda=0$  and no leading-edge sweep.

The center-of-pressure positions as obtained by the planar-model method for the afterbody and the no-afterbody cases are compared with the slender-body theory centers of pressure in figure 14. For the case of the subsonic-leading-edge wing,  $m\beta=0.2$ , for which slender-body theory would be expected to be the most applicable, the agreement with the no-afterbody case is very good for the entire range of  $2\beta r/c_r$ . However, the agreement between the slender-body theory and the afterbody case is poor. The latter result is to be anticipated by a consideration of figure 4(a). For a given geometry, an increase in Mach number causes a primary portion of the pressure disturbance carried onto

Similarly for wings with subsonic edges there is obtained

$$M_{B(W)} = \frac{8q_\infty\alpha_W(m\beta)^{3/2}}{\pi\beta(\beta m+1)} \int_0^d d\eta \int_{\beta\eta}^{c_r+\beta\eta} \frac{\xi \sqrt{\frac{\xi}{\beta} - \eta}}{\sqrt{m\xi + \eta}} d\xi \quad (69)$$

giving

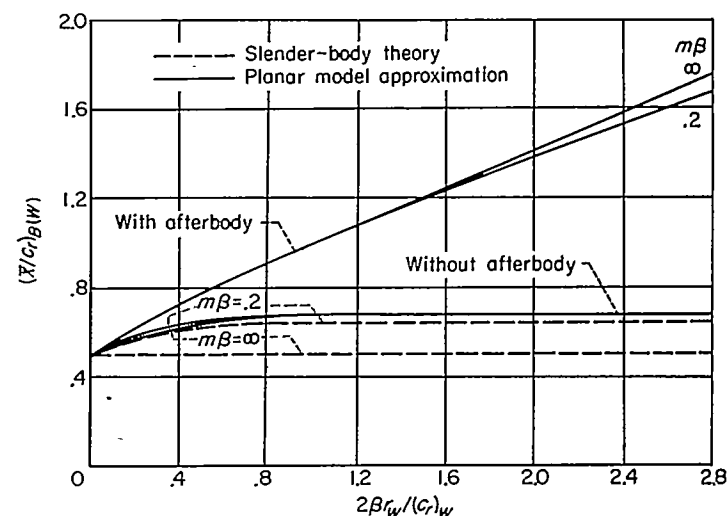


FIGURE 14.—Comparison of planar model values of  $(\bar{x}/c_r)_{B(W)}$  with slender-body theory values.

the body to sweep beyond the wing trailing edge. Similarly, a decrease in chord with a given Mach number and body diameter moves the wing trailing edge ahead of the primary portion of the lift disturbance carried onto the body. Since the present method agrees very well with slender-body theory where slender-body theory is expected to be applicable, and since slender-body theory does not properly account for the afterbody, the present method of determining  $(\bar{x}/c_r)_{B(W)}$  is applied to all combinations.

**Subsonic flow.**—Hitherto, no method seems to have been available for estimating  $(\bar{x}/c_r)_{B(W)}$  at subsonic speeds. For this purpose, the lifting-line model shown in figure 15 has been used. The lifting line is placed along the quarter-chord line of the wing and its image is introduced inside the body. The external lifting line is divided into a number of bound vortices, the strengths of which are proportional to the circulation distribution. The lifting line is not uniformly loaded although each of the horseshoe vortices is. The external vortices have their internal images which produce the lift on the body, this lift being produced at the bound part of the horseshoe vortex. Since the lift on the body due to each elemental image horseshoe vortex is proportional to the product of its strength times the length of its bound element, and since its lift acts at the bound

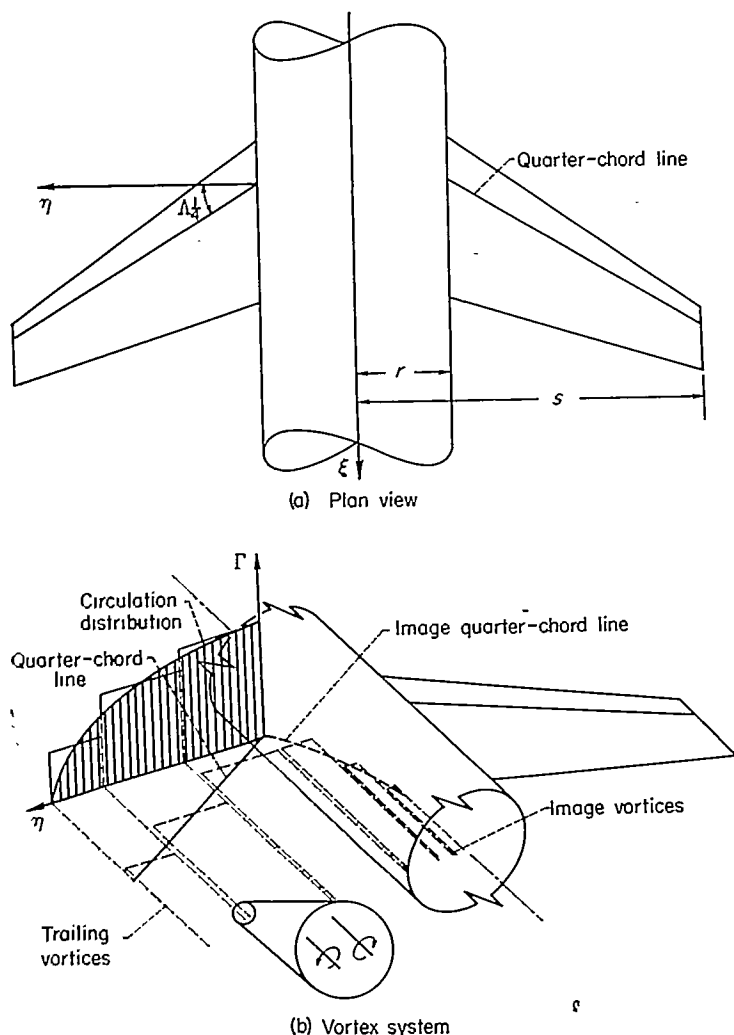


FIGURE 15.—Vortex model for determining center of pressure of body in presence of wing or tail at subsonic speeds.

element, it is easy to determine the center of lift of all the image horseshoe vortices. The formulas for the calculation are presented in Appendix D and the results for  $(\bar{x}/c_r)_{B(W)}$  at subsonic speeds are presented in chart 16. In Appendix D, the lifting line was assumed to be elliptically loaded. This assumption should be valid for most cases since the calculation is not sensitive to the span loading and since efficient wings tend to be elliptically loaded. No difference between  $(\bar{x}/c_r)_{B(W)\alpha}$  and  $(\bar{x}/c_r)_{B(W)s}$  has been considered since any such differences will be small and are beyond the scope of available theory.

Chart 16 gives results for unswept leading edges, midchord lines, and trailing edges as a function of  $\beta A$  and  $r/s$ . The results for  $\beta A \geq 4$  represent the results of lifting-line theory. It is to be noted that no dependence on aspect ratio is found on the basis of lifting-line theory. It is known that at low aspect ratios the loading on the wing-body combination approaches the slender-body loading for which the center of pressure on the body is known. The value from slender-body theory is plotted on the chart at  $\beta A = 0$ . Furthermore, for  $r/s = 0$  it is clear that  $(\bar{x}/c_r)_{B(W)}$  equals the center of pres-

sure of the loading at the root chord of the wing alone. This quantity has been obtained from the work of reference 26 for rectangular and triangular wings of low aspect ratio. The results of reference 26 agree with good accuracy with the lifting-line-theory results for  $r/s = 0$  at about  $\beta A = 4$ . Therefore, lifting-line theory has been adopted for  $\beta A > 4$ , and for  $\beta A < 4$  the curves have been extrapolated to the slender-body values at  $\beta A = 0$  with the  $r/s = 0$  results used as a guide. The extrapolated curves are shown dotted in chart 16. The distance of the center of pressure from the most forward point of the body is

$$\bar{l}_{B(W)} = l_W + (c_r)_W \left( \frac{\bar{x}}{c_r} \right)_{B(W)} \quad (71)$$

#### CENTER OF PRESSURE OF TAIL IN PRESENCE OF BODY

The center of pressure of the tail in the presence of the body (wing-tail interference being neglected) is given by the same procedure as that for the wing. For supersonic speeds the value of  $(\bar{x}/c_r)_T$  as determined from chart 10 is used as an approximation to  $(\bar{x}/c_r)_{T(B)}$ . For subsonic speeds the charts of reference 23 or those of chart 11 are available for estimating  $(\bar{x}/c_r)_T$ . The distance from the most forward point of the body to the tail center of pressure is thus

$$\bar{l}_{T(B)} = l_T + (c_r)_T \left( \frac{\bar{x}}{c_r} \right)_{T(B)} \quad (72)$$

#### CENTER OF PRESSURE ON BODY DUE TO TAIL

The center of pressure on the body due to the tail, wing-tail interference being neglected, is determined by the same procedure as that due to the wing. For supersonic speeds charts 14 and 15 are used. For subsonic speeds chart 16 is used in estimating  $(\bar{x}/c_r)_{B(T)}$ . From these values the distance from the foremost point of the body to the center of pressure is

$$\bar{l}_{B(T)} = l_T + (c_r)_T \left( \frac{\bar{x}}{c_r} \right)_{B(T)} \quad (73)$$

#### CENTER OF PRESSURE OF TAIL SECTION DUE TO WING VORTICES

The flow over the tail due to the wing vortices varies greatly as the position of the vortex varies with respect to the tail. It follows that the center of pressure of the lift due to the effect of the vortices on the tail section is also dependent on the position of the vortices with respect to the tail. It is possible on the basis of strip theory to take account of this effect. However, the refinement is hardly warranted in view of the fact that the distance from the center of moments to the tail is usually large so that great precision in the location of the center of pressure of the load on the tail section due to the wing vortices is unnecessary. A good approximation is to take the center of pressure as that for the tail panels in combination with the body. Thus

$$\bar{l}_{T(V)} = \bar{l}_{T(B)} \quad (74)$$

## SUMMARY OF CENTER-OF-PRESSURE POSITIONS OF WING-BODY-TAIL COMBINATION

The components of the lift, with the exception of the lift on the wing afterbody due to the wing vortices, have center-of-pressure positions estimated as follows:

1. Center of pressure of body nose,

$$\bar{l}_N = l_N \left( 1 - \frac{V_s}{\pi r_N^2 l_s} \right) \quad (75)$$

2. Center of pressure of wing in presence of body,

$$\bar{l}_{W(B)} = l_W + \left( \frac{\bar{x}}{c_r} \right)_{W(B)} (c_r)_W \quad (76)$$

with

$$\left( \frac{\bar{x}}{c_r} \right)_{W(B)} = \frac{K_{W(B)} \alpha \left( \frac{\bar{x}}{c_r} \right)_{W(B)\alpha} + k_{W(B)} \delta_W \left( \frac{\bar{x}}{c_r} \right)_{W(B)\delta}}{K_{W(B)} \alpha + k_{W(B)} \delta_W} \quad (77)$$

$$\bar{l}_c = \frac{l_N(C_L)_N + \bar{l}_{W(B)}(C_L)_{W(B)} + \bar{l}_{B(W)}(C_L)_{B(W)} + \bar{l}_{B(T)}(C_L)_{B(T)} + \bar{l}_{T(B)}(C_L)_{T(B)} + \bar{l}_{T(V)}(C_L)_{T(V)}}{(C_L)_N + (C_L)_{W(B)} + (C_L)_{B(W)} + (C_L)_{B(T)} + (C_L)_{T(B)} + (C_L)_{T(V)}} \quad (82)$$

## HINGE-MOMENT THEORY

The methods for estimating  $(\bar{x}/c_r)_{W(B)\alpha}$  and  $(\bar{x}/c_r)_{W(B)\delta}$  for the complete combination contain within themselves the methods for obtaining  $C_{h_\alpha}$  and  $C_{h_\delta}$ . However, it should be pointed out that, in general, greater accuracy is needed in the value of  $(\bar{x}/c_r)_{W(B)}$  for estimating hinge moments than for estimating the moment characteristics of the complete combination. Consider, for instance, a triangular, all-movable control which has a nearly constant center-of-pressure position through the speed range, and the hinge line of which is located close to the center-of-pressure location. For such a control, small changes in center-of-pressure position represent large changes in hinge-moment coefficient so that accurate values of  $(\bar{x}/c_r)_{W(B)}$  are desired.

The values of  $C_{h_\alpha}$  and  $C_{h_\delta}$  are given very simply by the following expressions:

$$C_{h_\alpha} = -(c_r/\bar{c}) K_{W(B)} [(\bar{x}/c_r)_{W(B)\alpha} - (x_h/c_r)] (C_{L_\alpha})_W \quad (83)$$

$$C_{h_\delta} = -(c_r/\bar{c}) k_{W(B)} [(\bar{x}/c_r)_{W(B)\delta} - (x_h/c_r)] (C_{L_\alpha})_W \quad (84)$$

wherein the coefficients are based on the mean aerodynamic chord as the reference length. For triangular-wing and body combinations the values of  $(\bar{x}/c_r)_{W(B)\alpha}$  and  $(\bar{x}/c_r)_{W(B)\delta}$  can be obtained from chart 13, and for rectangular-wing and body combinations  $(\bar{x}/c_r)_{W(B)\delta}$  can be obtained from chart 12.

To estimate the hinge moment, the effect of wing section must be considered in the determination of  $(\bar{x}/c_r)_{W(B)}$ . If experimental results are available, the best method for doing this is to add the theoretical center-of-pressure shift due to interference as given by the present method to the experimental center-of-pressure position of the wing alone. If the experimental wing-alone center of pressure is not available, it can be estimated by adding the second-order theory or shock-expansion theory center-of-pressure shift for the two-dimensional wing section to the three-dimensional linear-theory center-of-pressure position.

3. Center of pressure on body due to wing,

$$l_{B(W)} = l_W + (c_r)_W \left( \frac{\bar{x}}{c_r} \right)_{B(W)} \quad (78)$$

4. Center of pressure of tail in the presence of body,

$$\bar{l}_{T(B)} = l_T + (c_r)_T \left( \frac{\bar{x}}{c_r} \right)_{T(B)} \quad (79)$$

5. Center of pressure on body due to tail,

$$\bar{l}_{B(T)} = l_T + (c_r)_T \left( \frac{\bar{x}}{c_r} \right)_{B(T)} \quad (80)$$

6. Center of pressure of tail section due to wing vortices,

$$\bar{l}_{T(V)} = l_{T(B)} \quad (81)$$

The center of pressure for the entire combination is thus

## COMPUTATIONAL TABLE FOR DETERMINING LIFT COMPONENTS AND CENTERS OF PRESSURE

To organize and illustrate the calculations of the lift and center-of-pressure characteristics of wing-body-tail combinations, a computational table, based on the equations and charts already presented, is presented as table I. A numerical example (combination 101) is included in the table, which is self-explanatory. The reference area and moment reference point and length are arbitrary. Angular measures are always in degrees.

A possible confusion in the use of the computing table is the manner of using chart 7 when interpolations must be made with respect to  $\lambda$  and  $r/s$ . Normally, one can interpolate at constant values of the vortex lateral and vertical positions. However, for positions of the vortex near the body, the interpolation in  $r/s$  can carry the vortex inside the body. Under such circumstances, it is recommended that the interpolation be made at constant values of  $(h/s)_T$  and  $(f_T - r_T)/(s_T - r_T)$ , the vortex lateral position as a fraction of the span of the exposed tail panel. Again it is advocated that experimental values of the lift-curve slopes  $(C_{L_\alpha})_W$ ,  $(C_{L_\alpha})_T$ , and  $(C_{L_\alpha})_B$  be used if available. If the experimental values of  $(C_{L_\alpha})_W$  and  $(C_{L_\alpha})_T$  are unavailable, chart 8 can be used for supersonic speeds and the charts of reference 23 can be consulted for subsonic speeds. It is to be noted that in the calculative form, the body radius can be variable since the quantities  $r_N$ ,  $r_W$ , and  $r_T$  are all considered separately. If the body radius is varying at the wing or tail location, an average radius should be used at each location. The assumption has been used in determining the vertical vortex position at the tail that the wing vortex streams back in the free-stream direction. For variable body radius the assumption is made that in the plan view, the wing vortex streams back parallel to the side of the body. This assumption is incorporated into the computing table. The center of pressure of ogival noses presented in chart 9 is used in the computing table.

## EXPERIMENTAL VERIFICATION

To test the method of this report, a series of calculations have been performed to estimate the characteristics of a number of combinations, and these characteristics have been compared with experiment. The geometric and aerodynamic characteristics of these combinations for which the comparisons have been made are summarized in table II for wing-body combinations and in table III for wing-body-tail combinations.

For the most part the correlations are made on the basis of the lift and moments of the entire combination since the division of lift and moment between the components is not generally given by available experimental data. It should be borne in mind that correlation between the method and experiment on the basis of total lift does not necessarily imply that the distribution of lift between body and wing has been correctly predicted by the method.

Some difficulty was met in trying to determine lift- and moment-curve slopes from published curves since slight nonlinearities near  $\alpha=0$  were occasionally present. For these instances the curves were generally linear for  $\pm 2^\circ$ , and the average over this range was used. However, some of the moment characteristics for wing-body-tail combinations were so nonlinear that it was impossible to determine the center-of-pressure position at  $\alpha_B=0$  accurately, and in these cases the information was not entered in table III. The values of the lift-curve slope for the bodies alone were in some instances also difficult to obtain accurately because of the small slopes of the curves. Furthermore, the reliability of the experimental lift-curve slopes was sometimes questionable. In one case, data on similar configurations from different testing facilities (and at different Reynolds numbers) gave a difference of the order of 10 percent in the lift-curve slopes. Also, generally speaking, the data have not been corrected for any flow irregularities that may exist in the various wind tunnels. In view of these difficulties, together with the approximations made in the method, it was felt that a correlation of  $\pm 10$  percent would be a realistic accuracy to expect for the lift-curve slopes.

## LIFT

**Wing-body combinations.**—Figure 16 is a correlation between the estimated and experimental values of  $\beta(dC_L/d\alpha)_c$  for wing-body combinations at supersonic speeds. Configurations with triangular, rectangular, and trapezoidal wing plan forms are included. These may be identified by referring to table II. Included in figure 16 are the line of perfect agreement and dashed lines indicating  $\pm 10$  percent deviation from perfect agreement. It is readily apparent from this figure that the present method estimates the lift-curve slope within  $\pm 10$  percent for most of the combinations, and thus properly accounts for the first-order effects of wing-body interference.<sup>2</sup> The scatter about the lines of perfect agreement is apparently random and is due to second-order effects that will subsequently be discussed. The flagged symbols

<sup>2</sup> In this connection, it is significant to ask how much error can be introduced by neglecting interference. For the triangular wings of this report it was determined that the sums of the wing-alone and body-alone lift-curve slopes were, on the average, 20 percent greater than the corresponding experimental lift-curve slopes for the combinations when the wing alone is taken as the triangular wing that includes the blanketed area. For very small wings the sum can approach twice the experimental value.

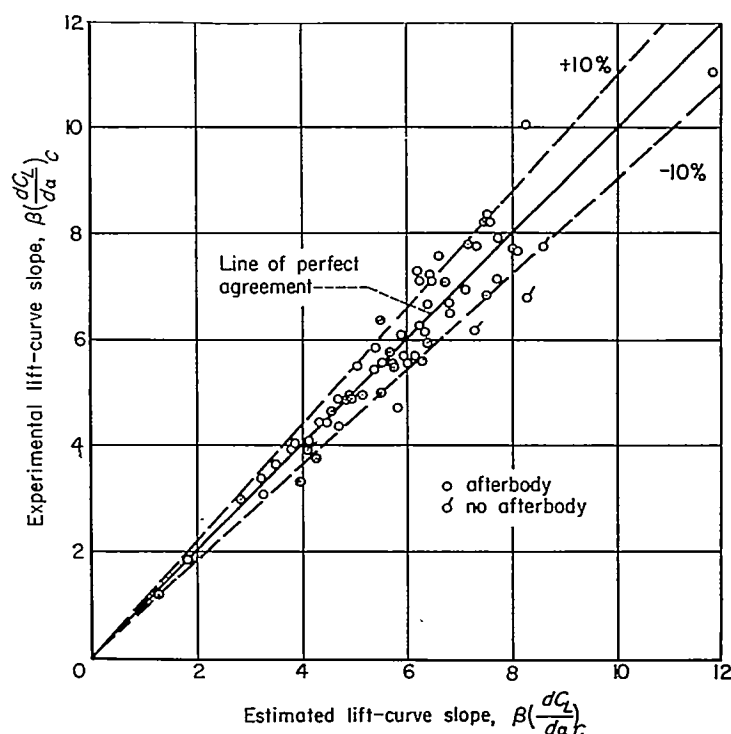


FIGURE 16.—Correlation between experimental and estimated lift-curve slopes for wing-body combinations at supersonic speeds;  $\alpha=0$ .

represent values calculated by afterbody theory for the configurations with no afterbody. On the average, the estimated lift-curve slopes for these points are larger than the experimental, as would be expected since the theory includes non-existent afterbody lift. When the no-afterbody theory is used, these points fall more in line with the other correlation points. In some instances, the effect of afterbody is large.

With regard to triangular wing-body combinations the present method is not substantially different from that of reference 6, which was found to be valid for such combinations. Thus, correlation for the triangular wing-body combinations was assured.

For the rectangular wing-body combinations, a point of interest is furnished by the fact that slender-body theory should be inapplicable. Consider the slender-body combination that includes the area  $OA'A$  in figure 17. According to

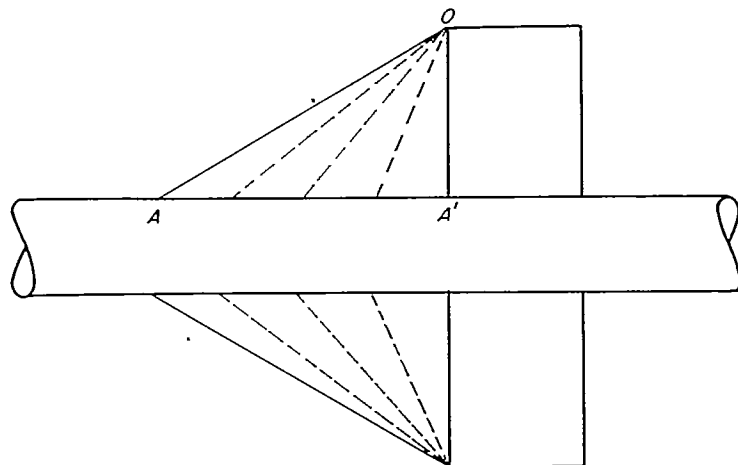


FIGURE 17.—Formation of rectangular wing-body combination from a slender combination.

slender-body theory the entire lift is developed on  $OAA'$ . If  $A$  approaches  $A'$ , the slender combination becomes non-slender and, on the basis of slender-body theory, the lift remains unchanged and is concentrated on the leading edge of the rectangular half-wing. This application of slender-body theory to rectangular wing-body combinations represents a degenerate case of the theory. It is thus interesting that slender-body theory values of  $K_{WB}$  produce correlation for rectangular wing-body combinations. The good correlation of the trapezoidal wing-body combinations is more significant than that for the triangular or rectangular wing-body combinations because generally four quantities are necessary to describe the geometry of trapezoidal combinations, whereas only two are necessary for the latter combinations.

In figure 18 the subsonic experimental values of  $\beta(dC_L/d\alpha)_c$  for wing-body combinations are plotted against the estimated values. Certain of the correlation points have flags to indicate that they represent the Mach number range 0.9 to 1.0. It is apparent that the present method of predicting  $\beta(dC_L/d\alpha)_c$  is accurate to within about  $\pm 10$  percent for wing-body combinations at subsonic speeds, as well as supersonic speeds.

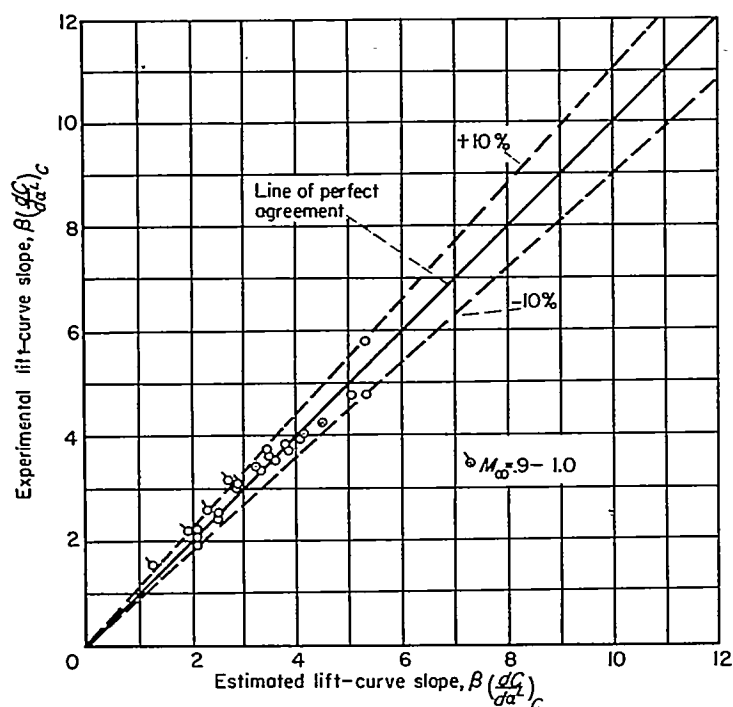
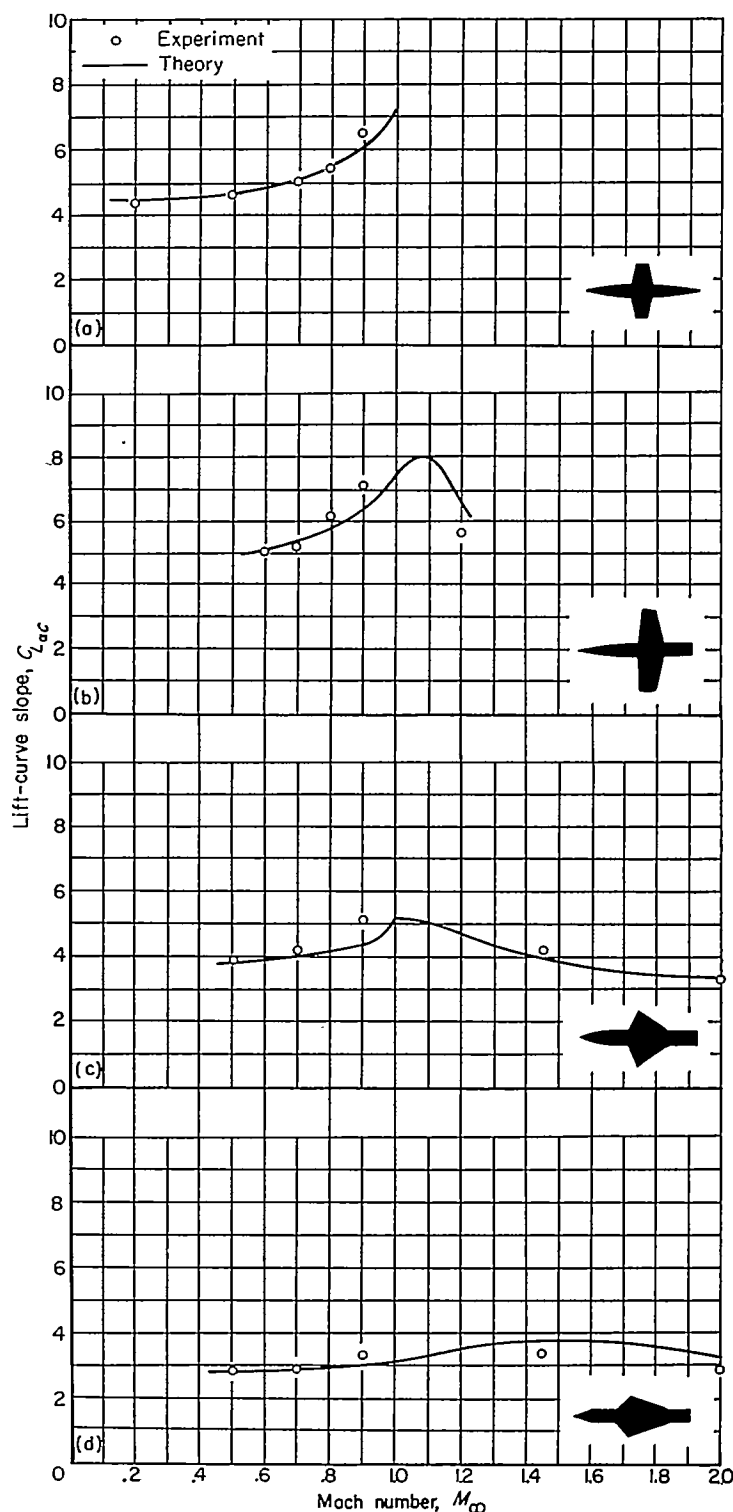


FIGURE 18.—Correlation between experimental and estimated lift-curve slopes for wing-body combinations at subsonic speeds;  $\alpha=0$ .

Figure 19 is presented to indicate how the present method predicts the trend with Mach number of the lift-curve slopes of wing-body combinations. For these examples the trends are well represented by the theory. However, in the transonic range the estimated magnitudes tend to be too small because of nonlinear transonic effects. Linear theory was used to compute the wing-alone lift-curve slope for the theory. McDevitt (ref. 27) has shown that for rectangular wings having NACA 65A0XX sections, good agreement between linear theory and experiment is obtained for lift near  $M_\infty=1$  if the transonic similarity parameter  $A(t/c)^{1/2}$



(a) Wing-body combination 1. (c) Wing-body combination 5.  
(b) Wing-body combination 4. (d) Wing-body combination 6.

FIGURE 19.—Variation with Mach number of lift-curve slope of several wing-body combinations at  $\alpha=0$ .

is less than unity. However, no well-defined dependence of the agreement between experiment and theory on this parameter was noted for the four plan forms represented in figure 19.

For some combinations the theory shows a peak in the lift-coefficient variation at  $M_\infty=1$ , while for other combinations the peak occurs on the supersonic side. For  $M_\infty=1$ ,

the effective aspect ratio is zero, and the slender-body value of the lift-curve slope,  $(\pi/2)A$ , has been used in the theory. On the supersonic side of  $M_\infty=1$  the values of  $\beta A$  are small and the wing lift-curve slope has been obtained from low-aspect-ratio linear theory. If the lift-curve slope so obtained is greater than that obtained from slender-body theory, then the maximum lift-curve slope occurs on the supersonic side of  $M_\infty=1$ . The behavior of the lift variation with Mach number around  $M_\infty=1$  thus depends on the low-aspect-ratio lift characteristics of the wing alone.

While the agreement between the estimated and experimental lift-curve slopes for the combinations compared is evidence suggesting that the division of lift between wing and body is correctly given by the present method; nevertheless, more direct evidence is needed to prove the point. Some such evidence is presented for supersonic speeds in figure 20 and table II. The experimental and estimated

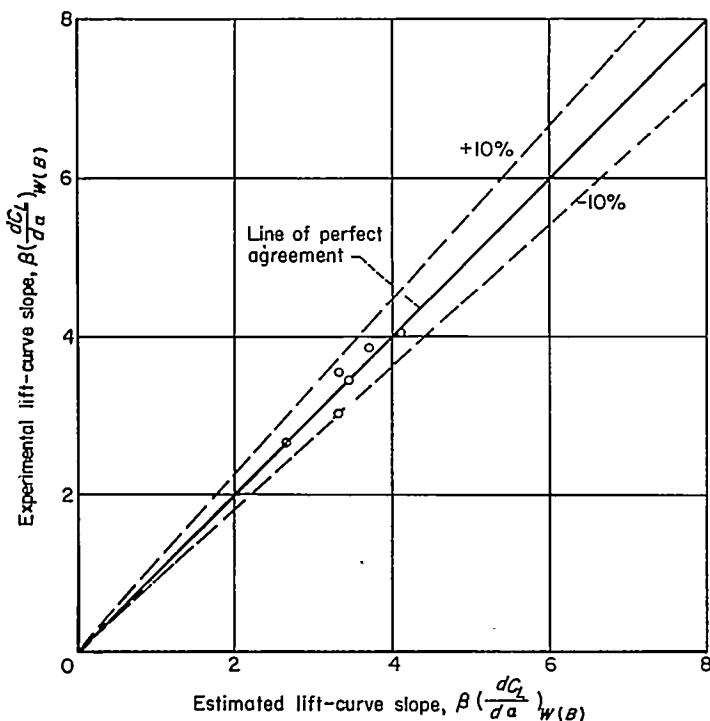


FIGURE 20.—Comparison of experimental and estimated lift-curve slopes for wings in the presence of the body at  $\alpha=0$ .

values of  $\beta(dC_L/d\alpha)_{W(B)}$  for the wing in the presence of the body are in good accord. At subsonic speeds data in reference 2 give the same division of lift between wing and body as a function of diameter-span ratio as the present method. The comparison of the data in this report is with the theoretical division as given by the Lennertz theory which, as previously pointed out, is numerically the same as that given by slender-body theory on which the present method is based.

The effects of wing-incidence angle on lift have been studied in a manner similar to the effects for angle of attack. Comparison is made between the experimental and theoretical values of  $\beta(C_{L_s})_C$  in figure 21. A group of three combinations corresponding to flagged symbols for which the wing-alone experimental values of  $(C_{L_s})_W$  are available are indi-

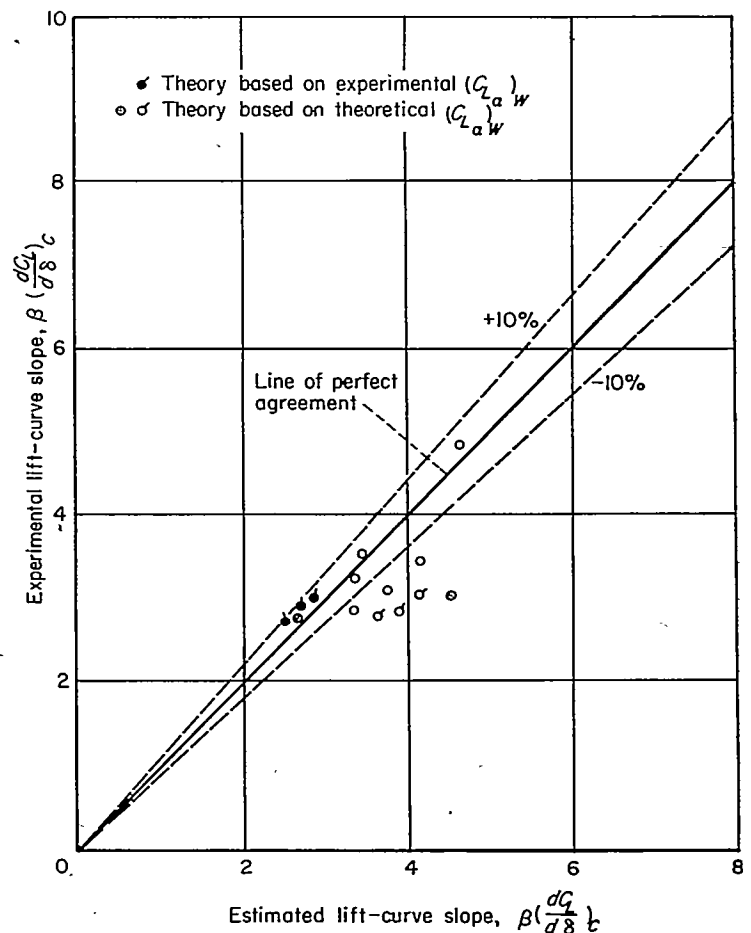


FIGURE 21.—Comparison of experimental and estimated lift-curve slopes for wing-body combinations at  $\delta=0$ .

cated. If, for the same combinations, the theoretical values of  $\beta(C_{L_s})_C$  are based on the experimental values of the wing-alone lift-curve slope, then the flagged points of figure 21 become the flagged solid points which are in good correlation with experiment. Generally the predicted values of  $\beta(C_{L_s})_C$  tend to be somewhat too large for the data correlated. There are not sufficient data to determine whether this effect is due to inaccuracies in the theory or to a tendency of the experimental wing-alone lift-curve slopes to be less than the theoretical slopes.

Experimental results available for the lift on the wing in the presence of the body due to variation in  $\delta$  are compared with the estimated results in figure 22 and table II. With the exception of three points, the agreement between theory and experiment is considered good. These three points are for a wing-body configuration for which the wing-alone lift-curve slope is not properly predicted by linear theory. When the experimental value of the wing-alone lift-curve slope is used in the estimation, the correlation between theoretical and estimated values is good.

**Wing-body-tail combinations.**—The values of  $\beta(dC_L/d\alpha)_C$  at  $\alpha=0$  obtained from experiment are plotted against the estimated values in figure 23 for subsonic speeds and in figure 24 for supersonic speeds (values are also presented in table III). To illustrate the importance of wing-tail interference, the points are shown as squares for no wing-tail

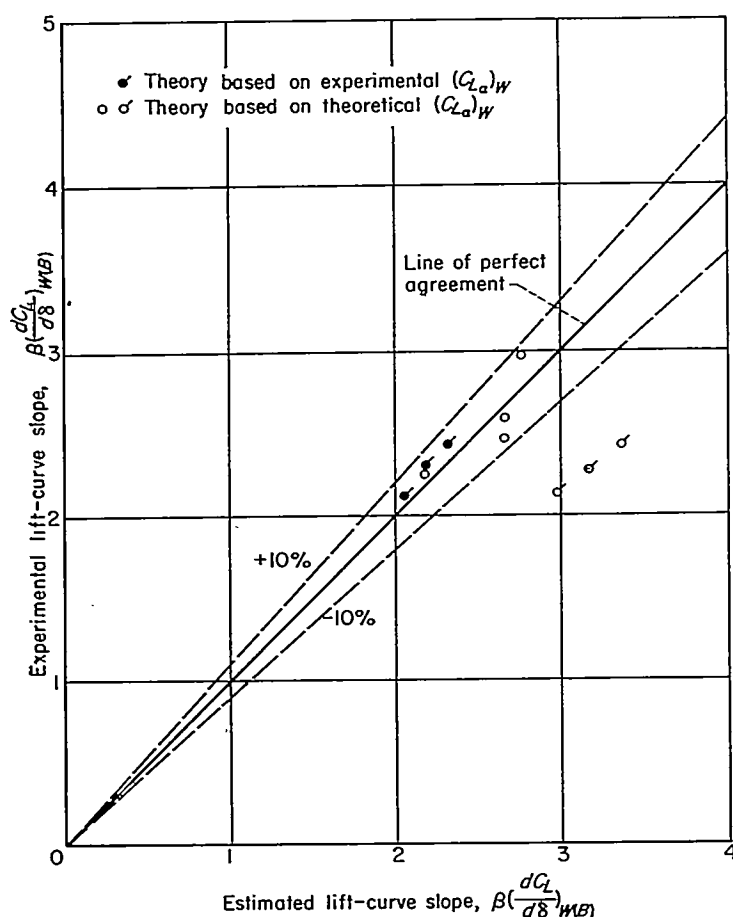


FIGURE 22.—Comparison of experimental and estimated lift-curve slopes for wings in the presence of the body at  $\delta=0$ .

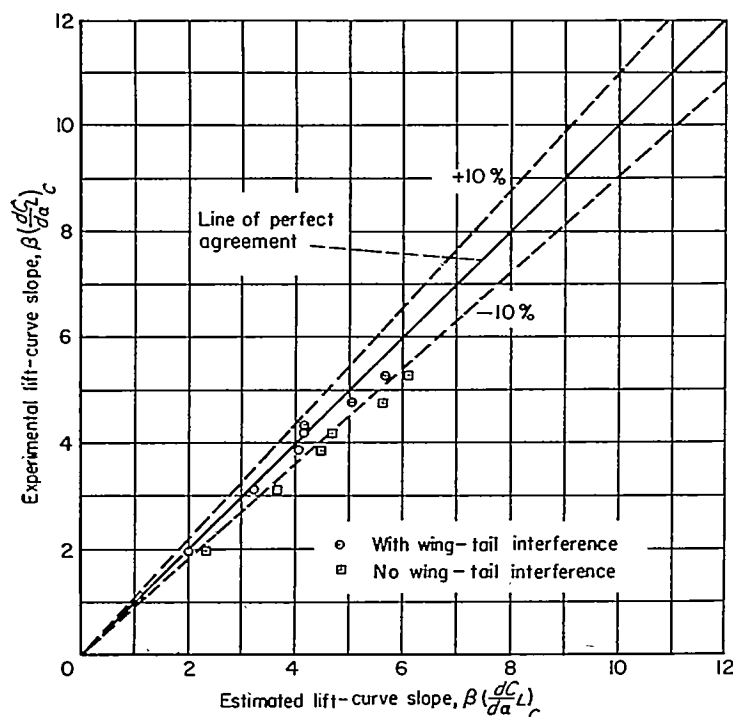


FIGURE 23.—Correlation between experimental and estimated lift-curve slopes for wing-body-tail combinations at subsonic speeds;  $\alpha=0$ .

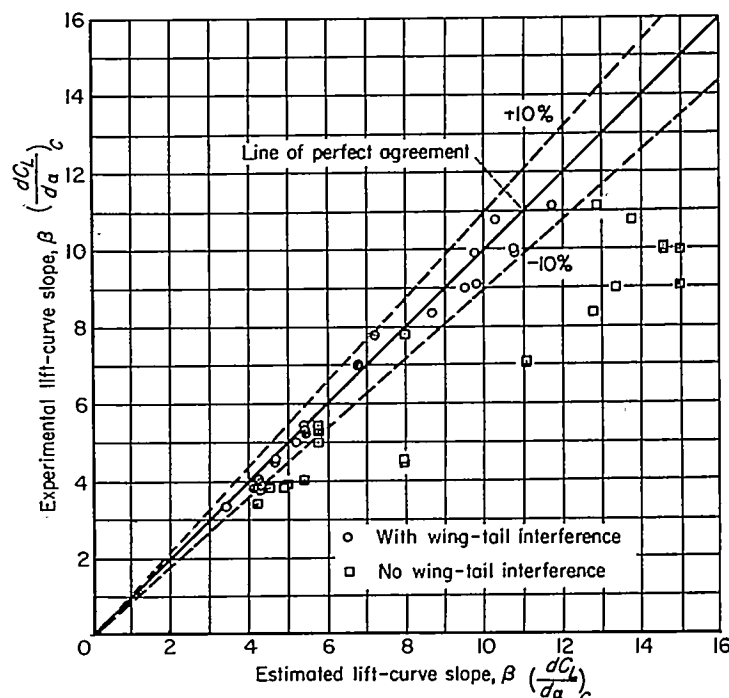


FIGURE 24.—Correlation between experimental and estimated lift-curve slopes for wing-body-tail combinations at supersonic speeds;  $\alpha=0$ .

interference considered in the estimates and as circles for wing-tail interference included in the estimated values. It is apparent that effects of wing-tail interference can be very large on a percentage basis, 30 to 40 percent. However, after the effects of wing-tail interference have been included in the theory, the errors are generally within  $\pm 10$  percent. Therefore, the accuracy of prediction of the wing-tail interference in the worst cases must be within about  $\pm 25$  to 30 percent.

The nonlinear variations of  $C_L$  with  $\alpha$  for two wing-body-tail combinations at subsonic speeds are shown in figure 25. The theory with and without wing-tail interference is shown. For these low angles of attack the theory including wing-tail interference is in good accord with the experiment. For higher angles of attack the body crossflow theory of reference 15 predicts that the lift is greater than that estimated by the theory of this report. A comparison is made between experiment and theory for a supersonic speed in figure 26. Again in the low angle-of-attack range the agreement between the experimental and theoretical values of the lift coefficient is good. The variations of lift-curve slope with Mach number for zero angle of attack are shown in figure 27 for two combinations. Although insufficient data are presented for a conclusive evaluation of the theory in the transonic range, the trends with Mach number are well predicted for the combinations considered.

#### LONGITUDINAL CENTER OF PRESSURE

**Wing-body combinations.**—The method of this report has been applied to the calculation of the centers of pressure of wing-body combinations of widely varying plan form. The results for the angle-of-attack case are compared with the



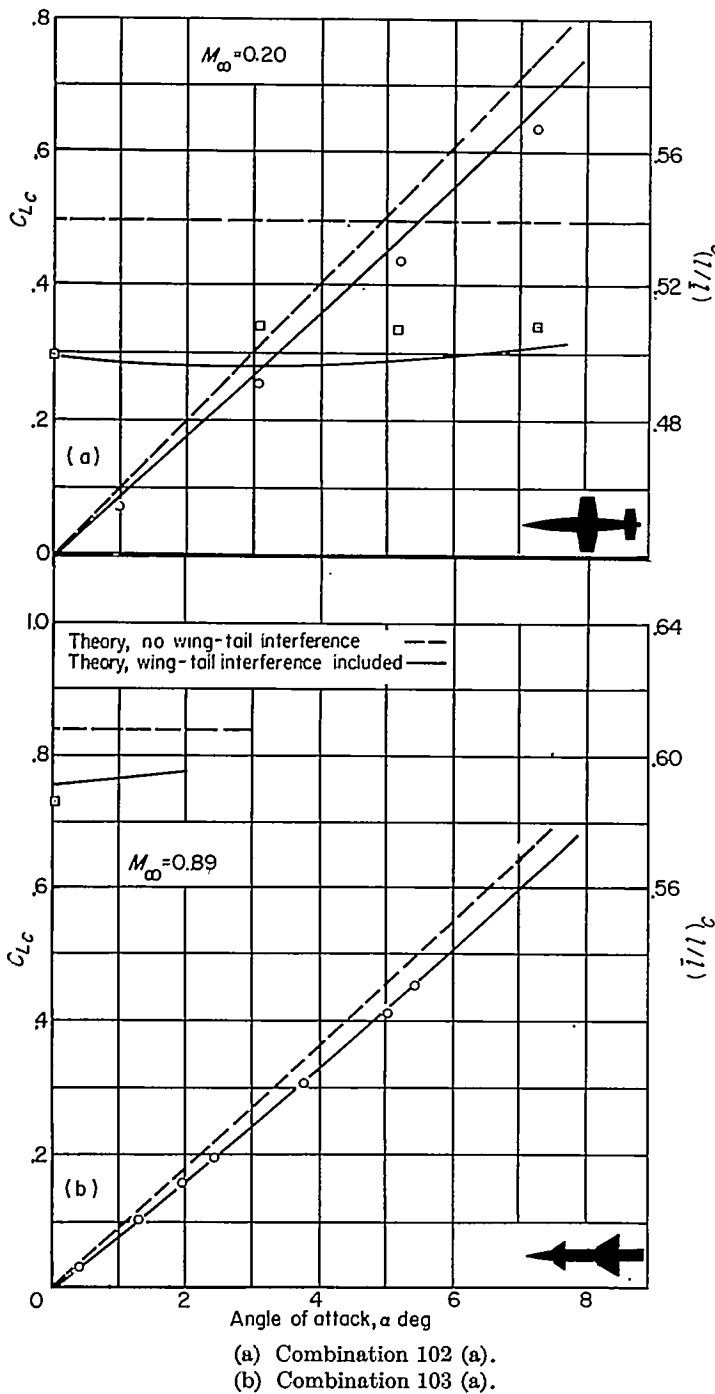


FIGURE 25.—Lift and center-of-pressure characteristics of wing-body-tail combinations at subsonic speeds.

experimental centers of pressure found by putting the experimental values of  $C_{L\alpha}$  and  $C_{m\alpha}$  into the expression

$$\left(\frac{l}{l}\right)_{C\alpha} = \frac{l_M - (C_{m\alpha}/C_{L\alpha})l_R}{l}$$

where  $l_R$  is the moment reference length in inches. The results summarized in table II and in figure 28 show the correlation between the experimental and theoretical results for supersonic speeds. Included in figure 28 is a line of perfect agreement and the lines of  $\pm 0.05 l$  deviation from perfect agreement. The flagged symbols represent points for configurations with no afterbody for which the afterbody theory

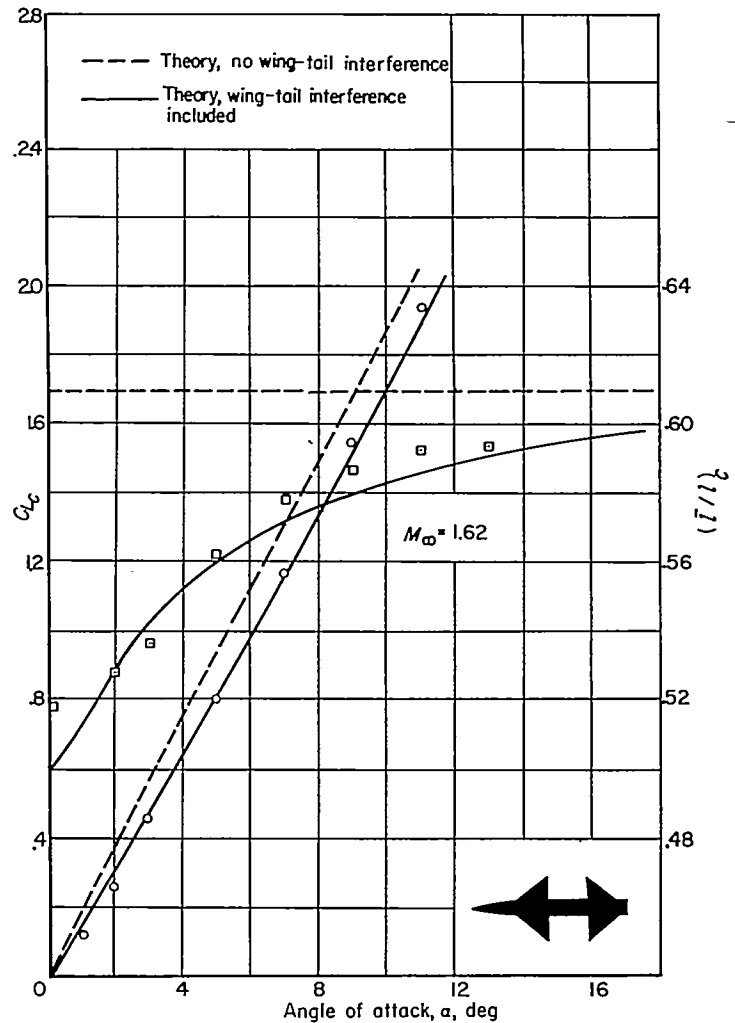


FIGURE 26.—Lift and center-of-pressure characteristics of wing-body-tail combination 117.

was used. When the no-afterbody theory is used, these points fall more in line with the other correlation points. As in the case of lift, the effect of afterbody on center of pressure can be large.

In general, the estimated centers of pressure are too far aft. Analysis of a number of wing-body combinations showed that this result is more pronounced for the rectangular wings than for the triangular wings and that the error in the estimation for trapezoidal wings is intermediate. To be specific, the line of mean correlation is displaced 0.009 body length from the line of perfect agreement for the triangular wings, 0.017 body length for the trapezoidal wings, and 0.026 body length for the rectangular wings. A possible explanation for the difference in correlation between the triangular and rectangular wing-body combinations can be made by consideration of the wing tip. It can be seen that the lift carry-over from a rectangular wing onto the shaded area of the body shown in figure 4 (b) is independent of span, provided that  $\beta\lambda \geq 2$ , and can be considered that due to an infinite wing. In order to form a finite wing, a "canceling wing" must be superposed on the infinite wing to form a wing tip. This canceling wing generates a negative lift which is transmitted in part onto the body aft of the trailing edge of the wing at a distance which depends primarily on the Mach number

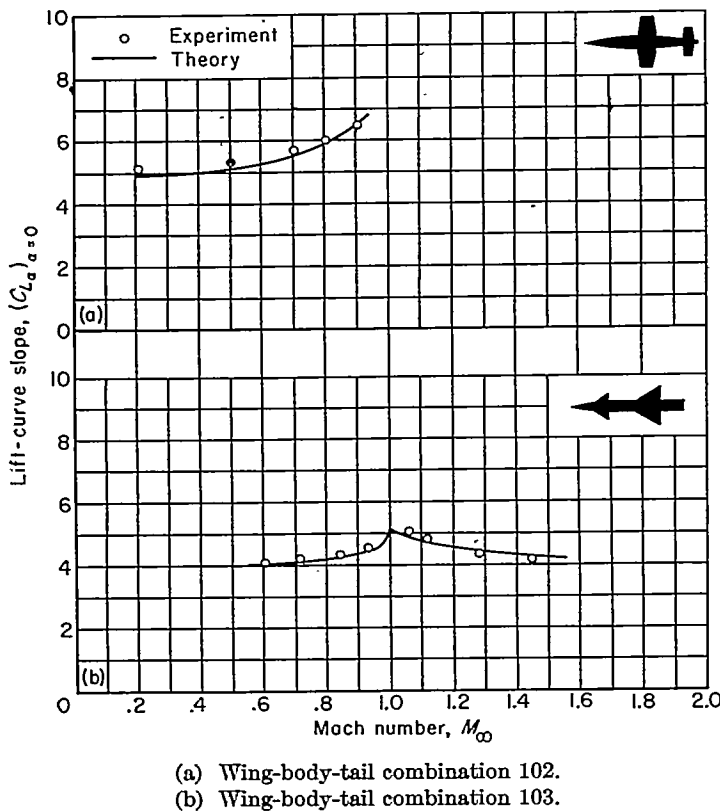


FIGURE 27.—Variation with Mach number of lift-curve slope of wing-body-tail combinations at  $\alpha=0$ .

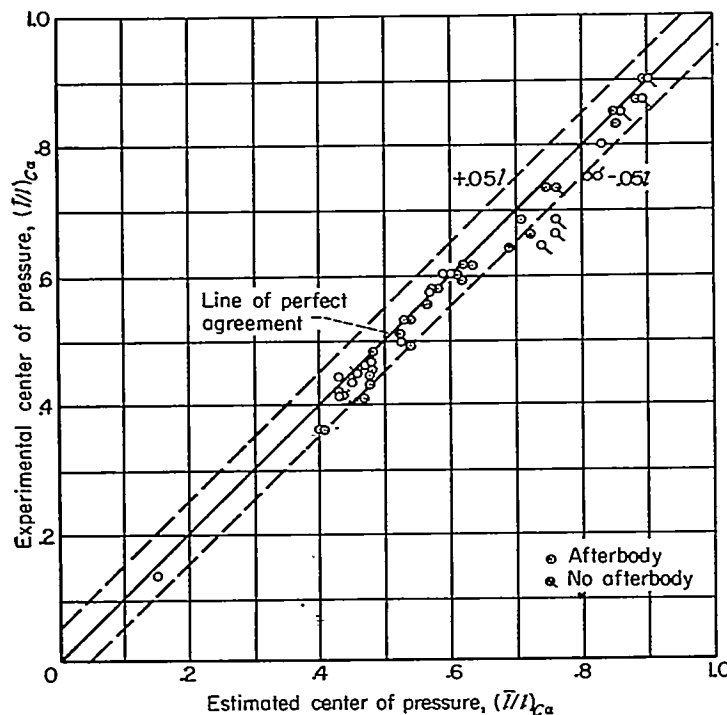


FIGURE 28.—Correlation between experimental and estimated centers of pressure for wing-body combinations at supersonic speeds;  $\alpha=0$ , no empirical corrections.

and wing semispan. While this negative lift carry-over is probably small, its effect on the over-all moment and center-of-pressure position of the combination might be appreciable due to the large moment arm involved. Since no account was taken of this decreased lift on the afterbody, the calculated

centers of pressure for the rectangular wing-body combinations are too far aft. Triangular wings, having no tip chord, might be expected to have less wing-tip effects than rectangular wings. In view of these facts it is suggested that the aforementioned displacements of the lines of mean correlation be applied as an empirical correction for each of the three classes of plan forms considered. The result of applying this correction to the data in figure 28 is shown in figure 29. The center-of-pressure positions for the combinations are now estimated within  $\pm 0.02 l$  for the angle-of-attack case. This empirical correction has been applied to the theoretical values of  $\bar{l}_{Ca}/l$  in table II.

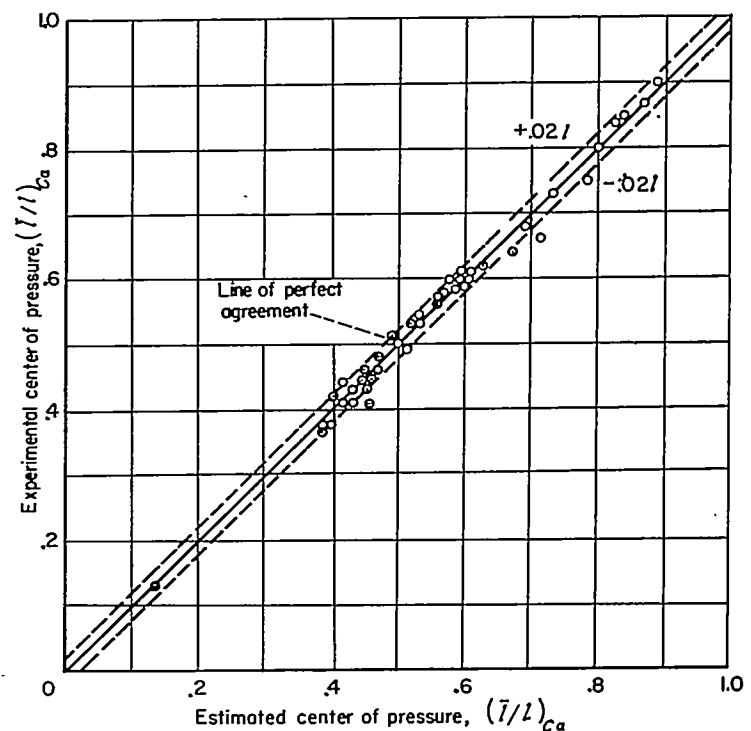


FIGURE 29.—Correlation between experimental and estimated centers of pressure for wing-body combinations at supersonic speeds;  $\alpha=0$ , with empirical corrections.

The center-of-pressure positions at subsonic speeds for wing-body combinations as determined experimentally have been plotted as a function of the estimated positions in figure 30. Lines of  $\pm 0.02 l$  error have been included in the figure. Generally speaking, the configurations correlated lie within the  $\pm 0.02 l$  error limits. It is to be noted that the errors are randomly distributed about the line of perfect agreement. Comparison is made between theory and experiment for subsonic and supersonic speeds in figure 31 in which the variation with Mach number of the centers of pressure is presented for four wing-body combinations. The theory for supersonic speeds has been presented in two manners. The solid line represents the theory without empirical correction, while the dashed lines represent the theory with the empirical corrections advocated. Generally speaking, the variation with Mach number of the center-of-pressure movement is not large so long as the transonic range is not traversed. However, through the transonic range, changes in center of pressure of appreciable magnitude can occur. The

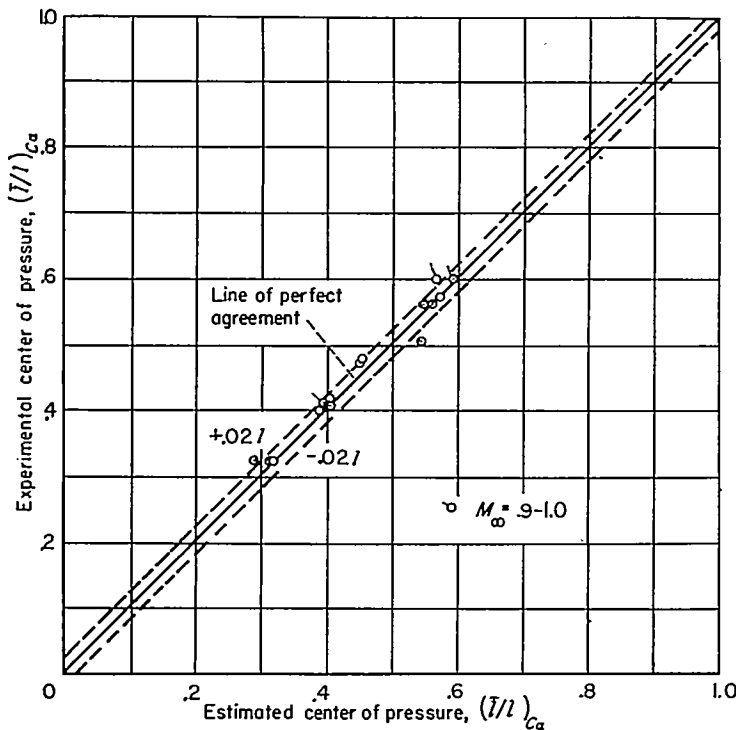


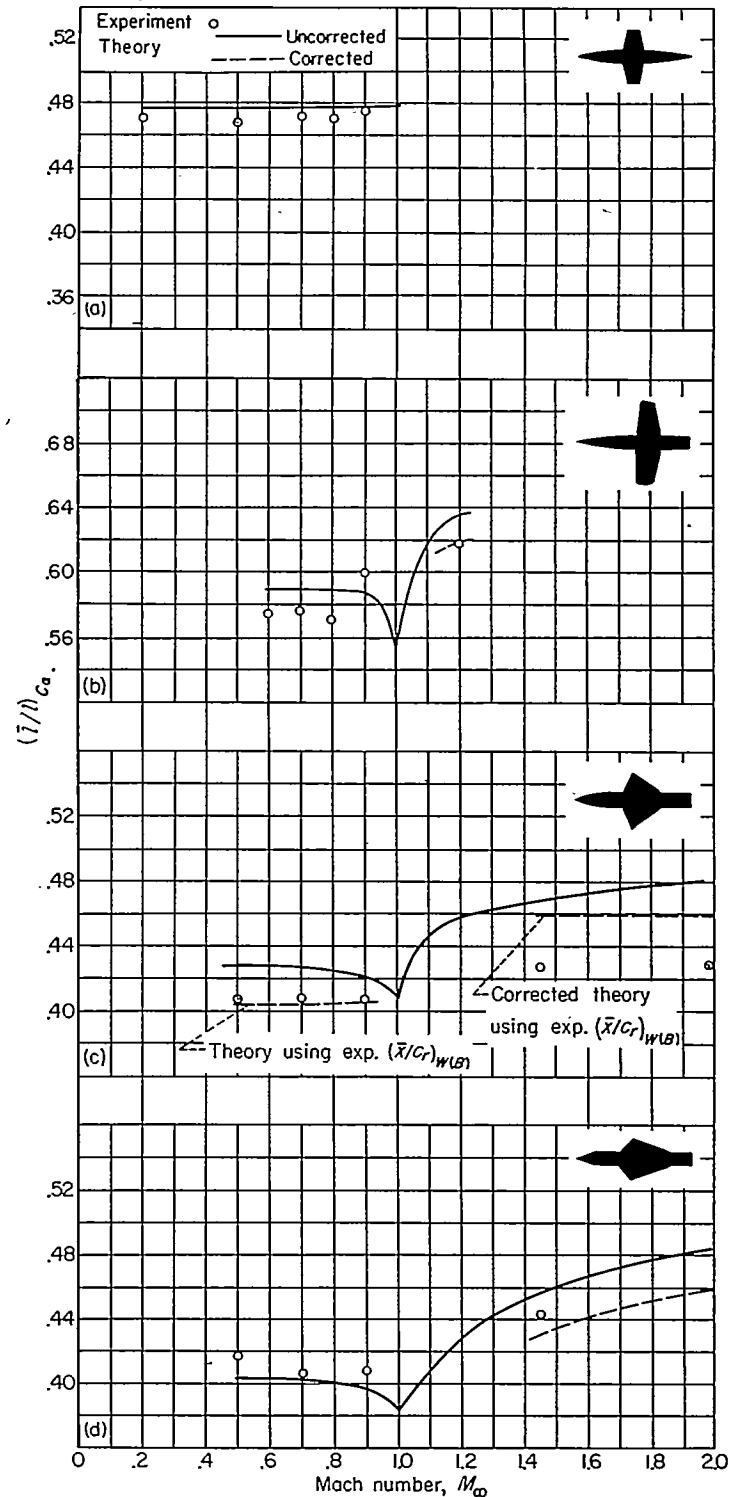
FIGURE 30.—Correlation between experimental and estimated centers of pressure for wing-body combinations at subsonic speeds;  $\alpha=0$ .

magnitudes of the shift are fairly well predicted when the empirical correction is made. It should be remembered that the correction applies only to wing-body combinations at supersonic speeds.

A comparison of the experimental values of  $(\bar{l}/l)_{Cp}$  with the theoretical values is presented in figure 32 and table II. The correction mentioned in connection with the angle-of-attack case is included in the estimated values. The present method, in conjunction with the empirical corrections, gives a means of estimating  $(\bar{l}/l)_{Cp}$  to within about  $\pm 0.02 l$ .

**Wing-body-tail combinations.**—A correlation of the center-of-pressure positions for  $\alpha=0$  at subsonic speeds, as determined experimentally and as estimated, are presented in figure 33 for wing-body-tail combinations. It is clear that inclusion of the effects of wing-tail interference is sufficient to move the points into the correlation band for almost all cases. The results for supersonic speeds are shown in figure 34. The effects of wing-tail interference are larger, generally, than for the subsonic wing-body-tail combinations. The correlation is accurate to within  $\pm 0.02 l$  for nearly all the combinations.

The effects of Mach number and angle of attack on the center-of-pressure position of wing-body-tail combinations can be very large. The effects of angle of attack are illustrated in figure 25 for subsonic speeds and in figure 26 for a supersonic speed. The theory with and without wing-tail interference is shown. The effects of wing-tail interference are generally large for the combinations illustrated. One important observation from figure 26 is that a large rearward change in center-of-pressure location with angle of attack is observed and predicted, a change that is comparable in magnitude to the effects of wing-tail interference itself. The rearward shift is due to a decrease in the tail



(a) Wing-body combination 1. (c) Wing-body combination 5.  
(b) Wing-body combination 4. (d) Wing-body combination 6.

FIGURE 31.—Variation with Mach number of center-of-pressure positions for wing-body combinations at  $\alpha=0$ .

download caused by the wing vortices as the angle of attack increases.

One of the important problems of aircraft and missile design, the center-of-pressure travel in the transonic range, is considered in figure 35. Although insufficient data are presented for a conclusive evaluation of the theory, the trends with Mach number are well predicted for the data considered and the absolute values of the center-of-pressure

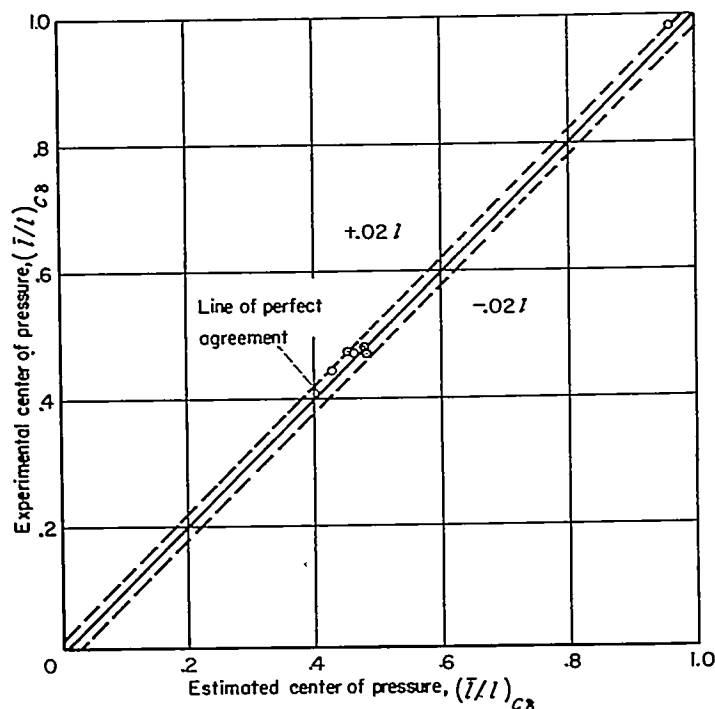


FIGURE 32.—Correlation between experimental and estimated centers of pressure for wing-body combinations at supersonic speeds;  $\delta=0$ .

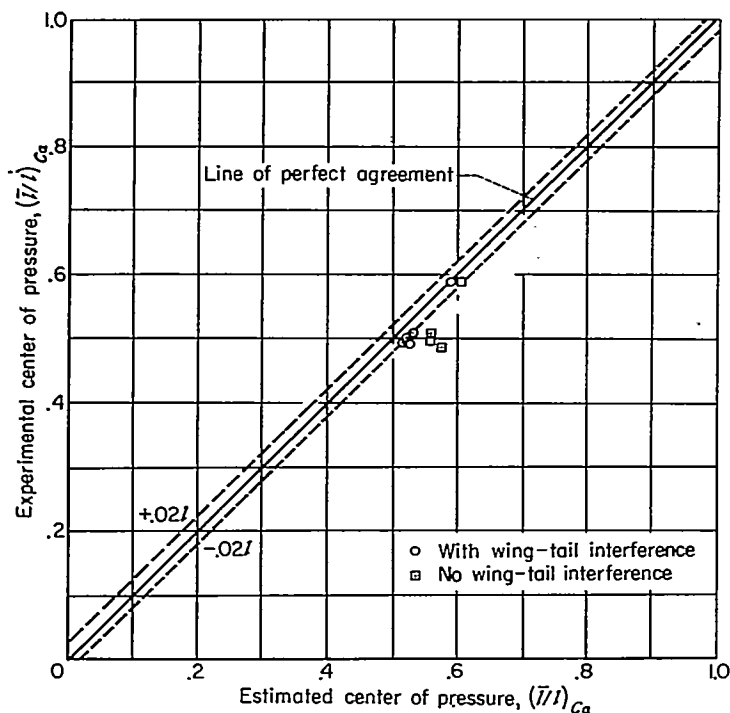


FIGURE 33.—Correlation between experimental and estimated centers of pressure for wing-body-tail combinations at subsonic speeds;  $\alpha=0$ .

position are within the  $\pm 0.02 l$  given as the accuracy of the method by the correlation curves.

There remain to discuss the effects of wing deflection on wing-tail interference. A positive deflection of a wing normally causes an upload on the wing, but the resulting wing vortex causes a download on the tail. As a result, a considerable pitching moment is developed. For slender wing-body-tail combinations with tail spans greater than the wing span, Morikawa, in reference 9, pointed out that the lift on

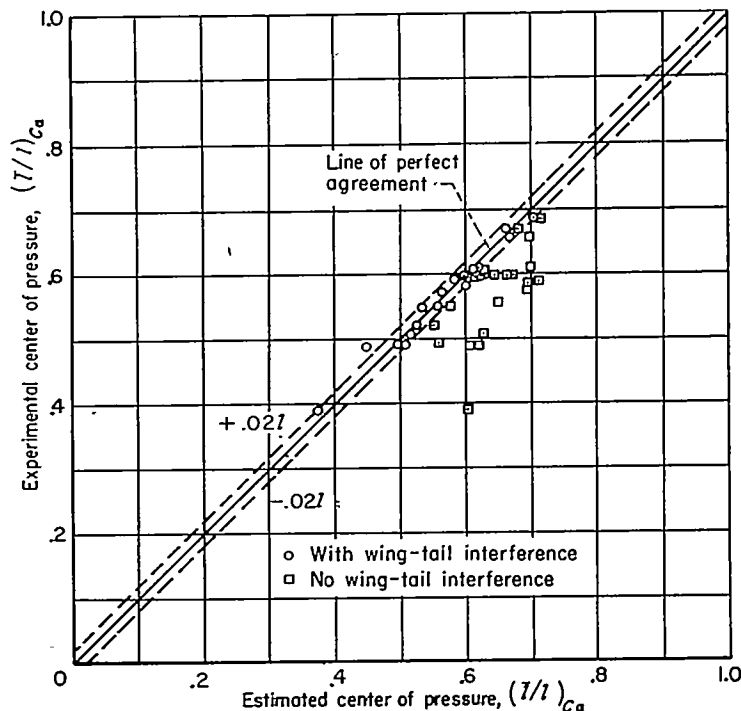
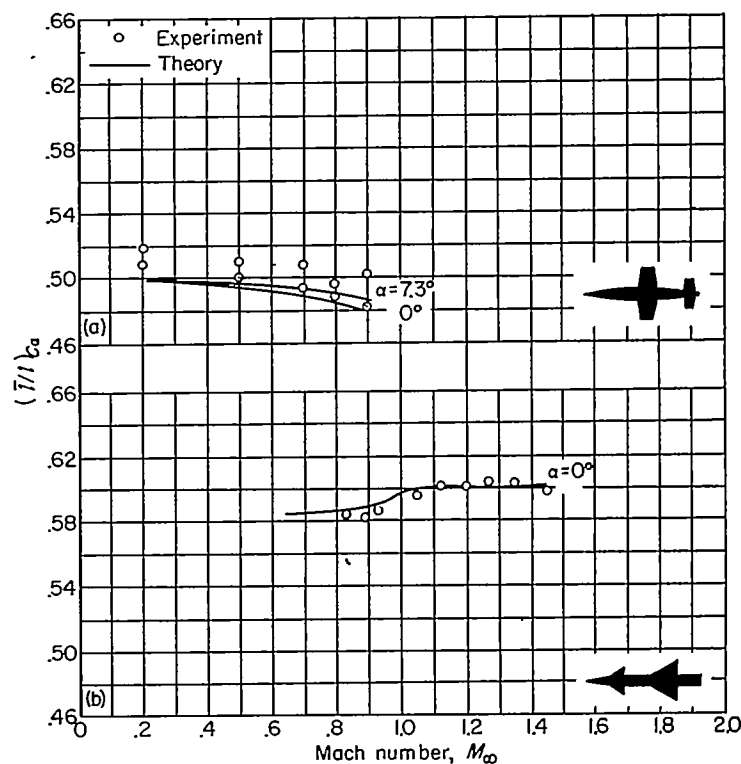


FIGURE 34.—Correlation between experimental and estimated centers of pressure for wing-body-tail combinations at supersonic speeds;  $\alpha=0$ .



(a) Wing-body-tail combination 102.  
(b) Wing-body-tail combination 103.

FIGURE 35.—Variation with Mach number of center-of-pressure location of wing-body-tail combinations at  $\alpha=0$ .

the tail due to interference is equal and opposite to that on the wing. Under these circumstances a pure couple is developed on the airplane due to wing deflection so that the center of pressure moves forward. The forward movement can be large.

To determine the validity of the present computational method for estimating the effects of wing incidence on the lift and moment interference of complete configurations, estimates are made of the lift and moment characteristics of those combinations for which data for variable wing incidence are available. The estimated and experimental characteristics are compared in figures 36 and 37 for two combinations having different wing and tail planforms. Both combinations exhibit the forward movement of the center of pressure. In the low angle-of-attack range where the theory applies, the agreement between theory and

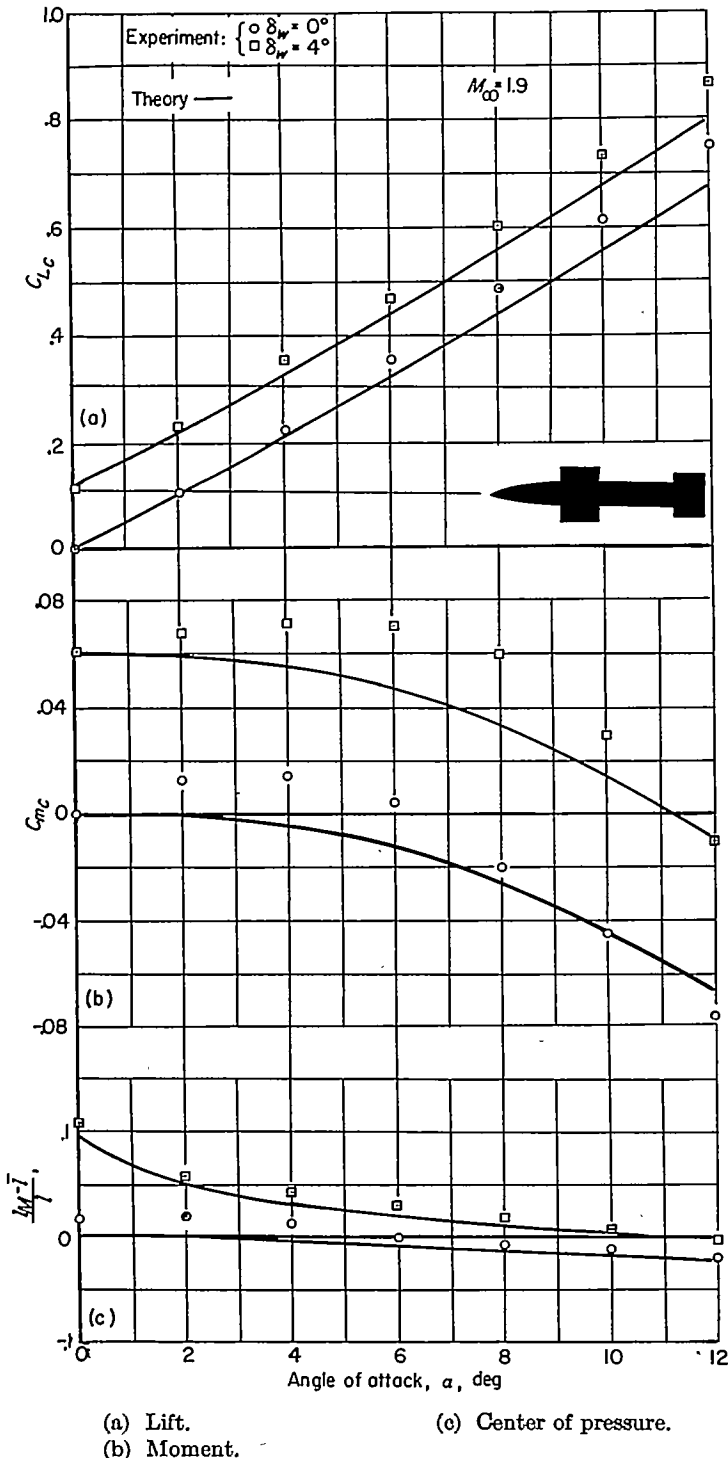


FIGURE 36.—Comparison between estimated and experimental effects of wing incidence for combination 104.

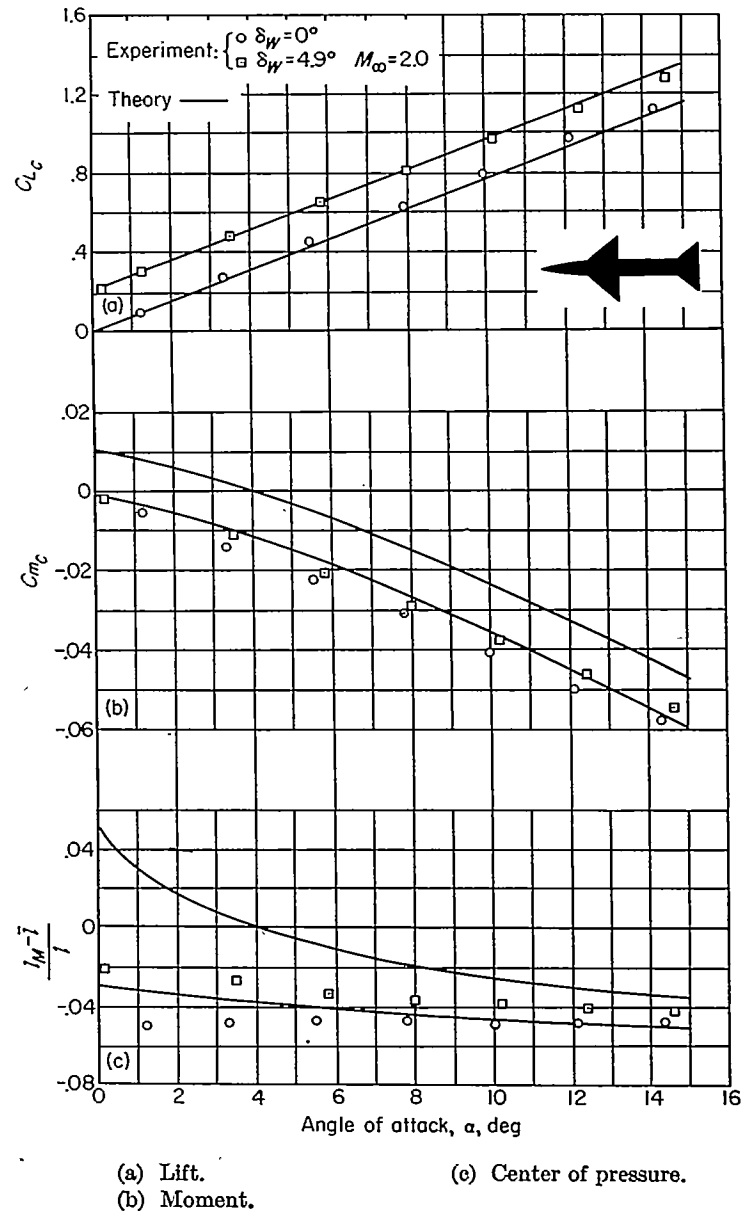


FIGURE 37.—Comparison between estimated and experimental effects of wing incidence for combination 101.

experiment is good for the combination of figure 36 but not for the combination of figure 37. This combination, which was tested at supersonic speeds and which has a triangular wing with supersonic leading edges, exhibits a behavior which is not explainable in terms of the theoretical model with one fully rolled-up vortex per wing panel. Figure 37 shows that the predicted lift due to wing deflection is in good agreement with experiment, but the predicted moment is not realized. Since the predicted moment is due primarily to tail download, it follows that the tail download is not developed. This behavior is explainable in terms of span loading. Experimental and theoretical results (ref. 3) indicate that for rectangular wings of sufficiently large aspect ratio, the span loading at the juncture of the wing and body is considerably below the maximum span loading on the wing for variable wing incidence at zero angle of attack. This means that the shed vorticity inboard has the opposite sense of rotation of that shed outboard, and upwash is generated inboard. Under these circumstances it appears

that two vortices per wing panel are the least number that can adequately represent the trailing-vortex system. The combination of figure 37 possesses a triangular rather than a rectangular wing, but its effective aspect ratio is 6.8 so that the foregoing effect might be anticipated. A complicating factor is that the shock wave is detached from the wing for all angles greater than about  $3^\circ$  so that the flow is, in part, transonic. Also, the tail span is considerably less than the wing span so that the tail is located largely behind the inboard portions of the wing. For these reasons it is felt that the theoretical model of one vortex per wing panel is inapplicable and that two vortices per wing panel are the minimum number that can describe the gross effects. However, more experimental work must be done before an accurate theory can be developed to cover this case.

#### HINGE-MOMENT COEFFICIENT

The hinge moments of an all-movable wing depend on the lift developed by the wing in the presence of the body as well as the center-of-pressure position of the wing. While a given percentage error in determining the value of  $(C_L)_{W(B)}$  causes the same percentage error in  $C_h$ , the same cannot be said for center-of-pressure position. Consider an all-movable wing with the center of pressure displaced 5 percent of the mean aerodynamic chord from the hinge line. An error of 1 percent of the mean aerodynamic chord in center-of-pressure position causes an error of 20 percent in hinge-moment coefficient. The necessity of having accurate estimates of center-of-pressure position to obtain accurate hinge-moment estimates is thus apparent. Furthermore, any effects such as Reynolds number, airfoil section, or slight wind-tunnel flow irregularities which would otherwise be inconsequential may well have important effects on hinge moments.

Unfortunately, an insufficient amount of data is available to determine the degree of correlation between experimental values of the hinge-moment coefficient and the values estimated by the present method. The data that are available (primarily for triangular-wing planforms) indicate that for both the angle-of-attack and the wing-incidence cases the predicted center-of-pressure positions are too far aft for the wing in the presence of the body. However, the predicted wing-alone center-of-pressure positions are too far aft by about the same amount. This means that the difference between  $(\bar{x}/c_r)_W$  and  $(\bar{x}/c_r)_{W(B)}$ , which represents the interference, is given fairly well by the theory. Therefore, the most accurate method of estimating the value of  $(\bar{x}/c_r)_{W(B)}$  would be to add to the measured value of  $(\bar{x}/c_r)_W$  the theoretical difference between  $(\bar{x}/c_r)_{W(B)}$  and  $(\bar{x}/c_r)_W$ . For the few cases checked, the center of pressure was estimated to within 0.02 of the root-chord length by this method. Although sufficient data are not available to make a thorough check on the validity of this procedure, the desirability of knowing the experimental wing-alone characteristics is clear.

#### LIMITATIONS AND EXTENSIONS OF THE METHOD

In the application of any method such as the present one, the important question of its limitations arises. Because of the very large number of variables specifying a wing-body-tail

combination, it is not practical to present correlations covering all possible combinations. For this reason the limitations and possible extensions of the method are best determined by an examination of the assumptions made with regard to certain parameters.

#### ANGLE OF ATTACK

It has already been stated that the assumption of linearity in the present method limits the useful angle-of-attack and wing-deflection ranges of the theory. At high angles of attack the wing-tail interference theory is invalidated by the appearance of body vortices and more than one vortex per wing panel. Also, the viscous crossflow of the type discussed by Allen and Perkins in reference 15 is sufficiently important to invalidate at high angles of attack any theory of wing-body combinations based solely on frictionless flow considerations.

#### MACH NUMBER

The present method is applicable to subsonic, transonic, and supersonic speeds. However, in the transonic range the nonlinearities exhibited by some combinations may cause the method to fail. For the cases for which nonlinearities exist, the ratio of the lift on the wing to the lift on the body of a wing-body combination can be properly predicted by the theory.

#### WING AND TAIL GEOMETRY

The only assumptions made for the wing planform are that the leading edges are not swept forward and that the trailing edges are not swept back. For sweptforward leading edges or sweptback trailing edges, the solution of slender-body theory used to determine  $K_{W(B)}$  and  $K_{B(W)}$  is not applicable because no account is taken of the additional vortices that exist for these conditions. The use of the correct cross-flow solution, determined by the method of Lomax and Byrd in reference 10, should circumvent this difficulty. However, some successful preliminary correlations between data for combinations with sweptback trailing edges and the estimates of the present method (ignoring the sweep of the trailing edges) indicate that the effect might not be large. While the present method is worked out only for unbanked configurations with two wing panels, it is possible by use of the appropriate slender-body-theory solution to extend the method to banked configurations with any number of wing panels. For interdigitated or high tails the method can be easily generalized. For differential incidence of the wing panels, the method is still applicable if a step-by-step calculation of the type discussed in reference 25 is used to determine the vortex position at the tail. The model on which the present method is based assumes maximum circulation at the wing-body juncture. A violation of this assumption invalidates the model. Such a condition could conceivably arise through the use of inverse taper, sweptforward wings, high-aspect-ratio deflected wing panels with supersonic leading edges, or wing panels having twist or camber, or from large gaps between wing and body.

#### BODY GEOMETRY

The method is formulated on the assumption of slender, pointed bodies having wings and tails mounted on body sections of uniform diameter, but the method can give good

estimated values for other conditions. If the wing is located close to the nose, the upwash field varies chordwise and spanwise instead of only spanwise as assumed in equation (15). The wing of the combination is thus effectively cambered as well as twisted, and the wing-body interference as well as the lift due to upwash is altered. However, this effect is not large for most practical cases. For the few cases for which varying body diameters were encountered in the data correlation, an average constant radius was assumed, and it was found that the estimated values correlated with the experimental values within  $\pm 10$  percent.

If the nose of a combination is not slender, the lift and center of pressure, as predicted by slender-body theory, is inapplicable. For such cases a more exact theory or preferably experimental body-alone results should be used. Theoretically, boattailing of the afterbody should have the effect of decreasing the lift of the combination if the flow follows the body. Because of flow separation, it is expected that little, if any, lift will be lost.

### CONCLUSIONS

On the basis of the comparison between predicted and measured lifts and center-of-pressure positions of a number of wing-body and wing-body-tail combinations for subsonic, transonic, and supersonic speeds, the following conclusions can be drawn:

1. The present method predicts lift-curve slope to within

$\pm 10$  percent for most combinations through the speed range considered. However, in the transonic range, nonlinear effects can reduce the accuracy of the lift prediction. The method takes account of the wing-tail interference which can change the combination lift by as much as 35 to 40 percent.

2. For wing-body and wing-body-tail combinations, the center-of-pressure positions are predicted to within  $\pm 0.02$  body length. However, in the transonic range nonlinear effects can reduce the accuracy of the center-of-pressure prediction. The method takes account of the wing-tail interference which can change the center-of-pressure position by as much as 10 to 20 percent of the body length.

3. Due to the sensitive dependence on center-of-pressure position on the wing, accurate values of the hinge-moment coefficient are not predicted by the present method. However, estimates of hinge-moment coefficient can be obtained by adding to the experimental center-of-pressure position of the wing alone the theoretical shifts due to interference as determined by the present method.

4. The nonlinear effects of angle of attack on center-of-pressure position and lift can be as important as those of Mach number.

AMES AERONAUTICAL LABORATORY

NATIONAL ADVISORY COMMITTEE FOR AERONAUTICS

MOFFETT FIELD, CALIF., July 8, 1953

## APPENDIX A

## WING-PANEL CENTER OF PRESSURE DUE TO DEFLECTING WINGS OF WING AND BODY COMBINATIONS

In reference 13, Spreiter has given the loading and center-of-pressure positions for the wing of a wing and body combination with zero wing incidence. However, for all-movable wings the problem of the center of pressure of the wing in the deflected state with the body at zero angle of attack is of importance. This result is readily obtained by methods similar to those used by Spreiter. In fact, the wing loading is given in reference 28 as

$$\left(\frac{\Delta p}{q_\infty \delta}\right)_{W(B)} = \frac{2 \tan \epsilon (\eta^4 - r^4) \left(\pi + 2 \cos^{-1} \frac{2r}{\eta + r^2/\eta}\right)}{\pi \eta^3 \sqrt{(\eta + r^2/\eta)^2 - (y + r^2/y)^2}} \quad (A1)$$

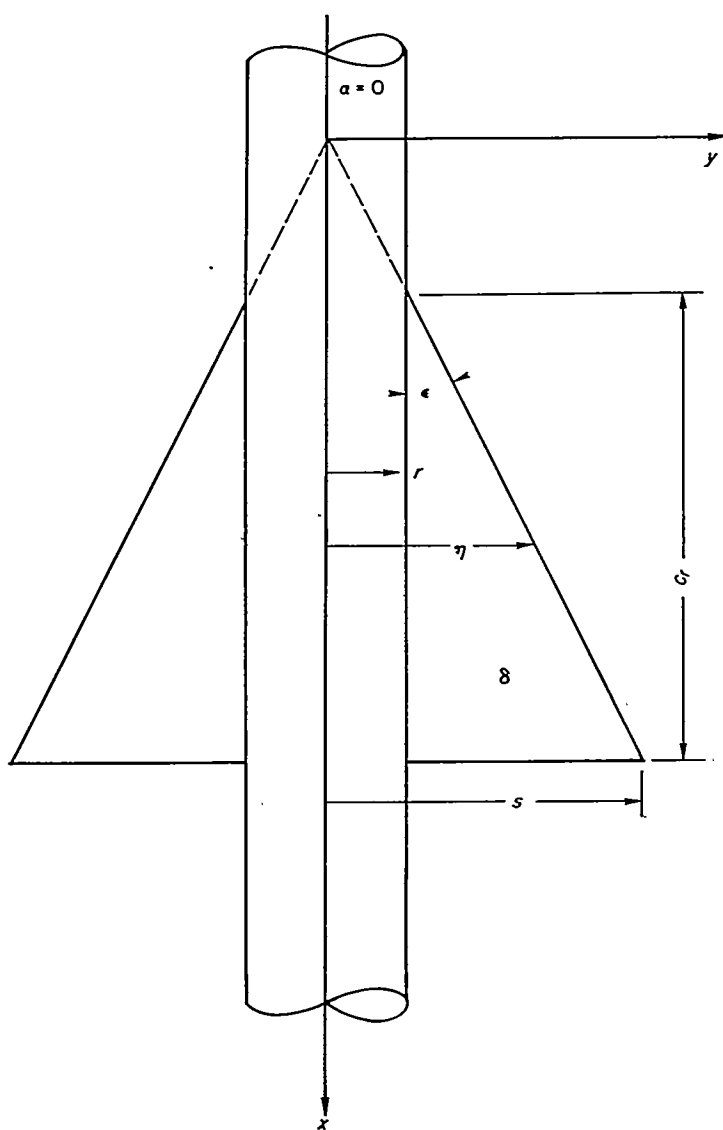


FIGURE 38.—Coordinate system and symbols for determination of center of pressure due to wing-deflection angle.

wherein the symbols are defined in figure 38. If  $M_{W(B)}$  is the moment developed by both wing panels about the  $y$  axis, it

is readily shown that this moment is given by

$$\frac{M_{W(B)}}{q_\infty \delta} = 2 \int_r^s \frac{\eta}{\tan \epsilon} \int_r^\eta \left(\frac{\Delta p}{q_\infty \delta}\right)_{W(B)} \frac{d\eta}{\tan \epsilon} \quad (A2)$$

One integration yields the result

$$\frac{M_{W(B)}}{q_\infty \delta} = \frac{1}{\pi \tan \epsilon} \int_r^s \frac{(\eta^4 - r^4)}{\eta^2} \left(\pi + 2 \cos^{-1} \frac{2r\eta}{\eta^2 + r^2}\right)^2 d\eta \quad (A3)$$

The second integration caused some difficulty because the integrals could not be expressed in terms of tabulated functions. Instead, it was found necessary to introduce two functions defined by the following rapidly convergent series:

$$\chi(x) = x + \frac{1}{2} \left(\frac{x^3}{3^2}\right) + \frac{1 \cdot 3}{2 \cdot 4} \left(\frac{x^5}{5^2}\right) + \frac{1 \cdot 3 \cdot 5}{2 \cdot 4 \cdot 6} \left(\frac{x^7}{7^2}\right) + \dots \quad (A4)$$

$$\psi(x) = x - \frac{x^3}{3^2} + \frac{x^5}{5^2} - \frac{x^7}{7^2} + \dots \quad (A5)$$

In terms of these functions, the moment is given by

$$\begin{aligned} \frac{\pi \tan \epsilon}{q_\infty \delta} M_{W(B)} = & \frac{16(s^4 + 3r^4)}{3s} (\tan^{-1} s/r)^2 - \frac{16r}{3} (s^2 + r^2) \tan^{-1} s/r - \\ & \frac{4\pi^2 r^3}{3} + \frac{16r^2}{3} (s-r) + \frac{8\pi r^3}{3} - 16\pi r^3 \log(s/r) + \\ & \frac{32\pi r^3}{3} \log \frac{s^2 + r^2}{2r^2} - 32r^3 [\psi(r/s) - \psi(1)] - \\ & \frac{128r^3}{3} [\chi(1/\sqrt{2}) - \chi(r/\sqrt{s^2 + r^2})] \end{aligned} \quad (A6)$$

If the moment is divided by the lift of the exposed wing panels as given in terms of  $k_{W(B)}$  (eq. (19)), the moment arm is obtained. It is convenient to express this moment arm in fractions of the root chord behind the leading edge of the wing-body juncture in the following equation wherein  $\tau$  is the radius-semispan ratio,  $r/s$ :

$$\begin{aligned} \left(\frac{\bar{x}}{c_r}\right)_{W(B)s} = & \frac{1}{2\pi^2 k_{W(B)} (1-\tau)^3} \left\{ \frac{16(1+3\tau^4)}{3} \left(\tan^{-1} \frac{1}{\tau}\right)^2 - \right. \\ & \frac{16\tau}{3} (1+\tau^2) \tan^{-1} \frac{1}{\tau} - \frac{4\pi^2 \tau^3}{3} + \frac{16\tau^2}{3} (1-\tau) + \frac{8\pi \tau^3}{3} + \\ & 16\pi \tau^3 \log \tau + \frac{32\pi \tau^3}{3} \log \frac{1+\tau^2}{2\tau^2} - 32\tau^3 [\psi(\tau) - \psi(1)] - \\ & \left. \frac{128\tau^3}{3} \left[\chi(1/\sqrt{2}) - \chi\left(\frac{\tau}{\sqrt{1+\tau^2}}\right)\right] \right\} - \frac{\tau}{1-\tau} \end{aligned} \quad (A7)$$

The quantity  $(\bar{x}/c_r)_{W(B)s}$  has been plotted as a function of  $r/s$  in chart 13.



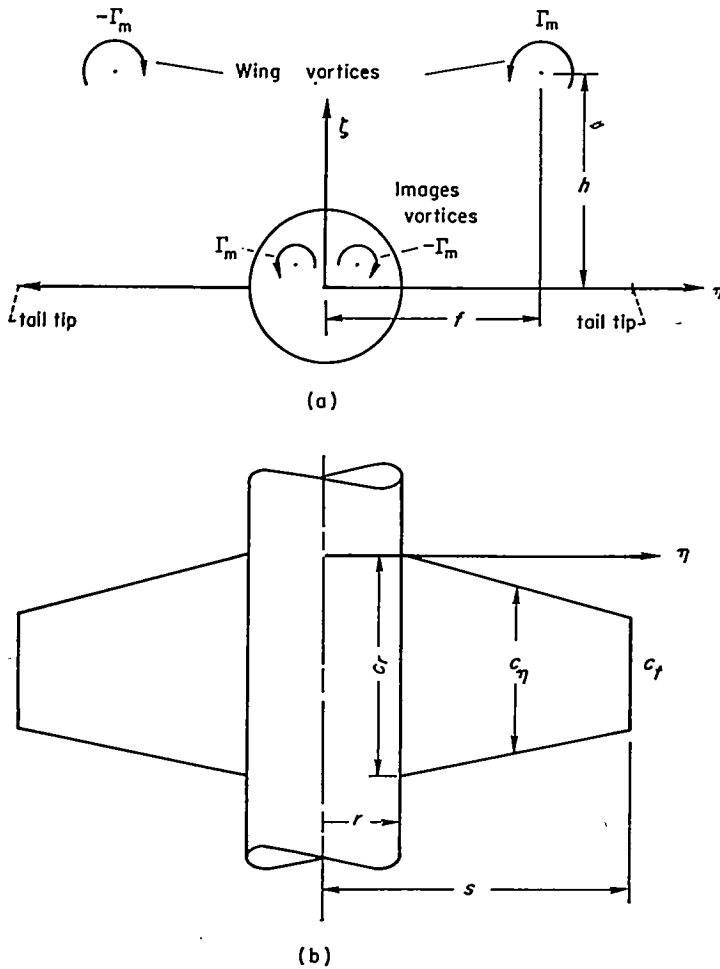
## APPENDIX B

## DETERMINATION OF TAIL INTERFERENCE FACTOR BY STRIP THEORY AND SLENDER-BODY THEORY

The tail interference factor to be evaluated is

$$i = \frac{L_{T(v)}/(L_T)_\alpha}{\Gamma_m/2\pi\alpha V_\infty(s_T - r_T)} \quad (B1)$$

The lift ratio is readily evaluated by a combination of strip theory and slender-body theory. The model used to obtain the vertical velocity at the tail induced by the wing vortices is the slender-body model of figure 39. From the Biot-



(a) Wing vortices in crossflow plane of tail.  
(b) Tail planform dimensions.

FIGURE 39.—Model and dimensions for determination of tail interference factor by strip theory.

Savart law for an infinite line vortex, the vertical velocity due to the right external vortex is

$$w = -\frac{\Gamma_m(f-\eta)}{2\pi[h^2+(f-\eta)^2]} \quad (B2)$$

In this equation  $\Gamma_m$  is positive counterclockwise facing upstream, and  $w$  is positive upward. The tail is effectively

twisted because of the variation of  $w$  across its span. All geometric quantities in the derivation are understood to be those of the tail rather than the wing so that no subscripts are used.

The application of strip theory to obtain the load on the tail due to the vortex involves an integration across the exposed part of the tail. As previously discussed, the lift evaluated by this procedure appears partly on the tail panels and partly on the body. If the section lift coefficient is taken as  $4/\beta$ , the lift due to the right external vortex on the right external panel is

$$L_1 = -\frac{q_\infty}{2\pi V_\infty} \int_r^s \left(\frac{4}{\beta}\right) \frac{\Gamma_m(f-\eta)}{h^2+(f-\eta)^2} c_\eta d\eta \quad (B3)$$

The value of  $L_1$  obtained by integrating equation (B3) is expressed with the aid of the following function:

$$L\left(\lambda, \frac{r}{s}, \frac{f}{s}, \frac{h}{s}\right) = \left\{ \frac{(s-r\lambda)-f(1-\lambda)}{2(s-r)} \ln \frac{h^2+(f-s)^2}{h^2+(f-r)^2} - \frac{1-\lambda}{s-r} \left[ (s-r)+h \tan^{-1}\left(\frac{f-s}{h}\right) - h \tan^{-1}\left(\frac{f-r}{h}\right) \right] \right\} \quad (B4)$$

as

$$L_1 = \frac{4q_\infty \Gamma_m c_r}{2\pi\beta V_\infty} L\left(\lambda, \frac{r}{s}, \frac{f}{s}, \frac{h}{s}\right) \quad (B5)$$

The lift on the right panel due to the left vortex is

$$L_2 = -\frac{4q_\infty \Gamma_m c_r}{2\pi\beta V_\infty} L\left(\lambda, \frac{r}{s}, -\frac{f}{s}, \frac{h}{s}\right) \quad (B6)$$

Consider the image vortices having coordinates  $f_i$  and  $h_i$  given by the following equation:

$$\left. \begin{aligned} f_i &= \frac{fr^2}{f^2+h^2} \\ h_i &= \frac{hr^2}{f^2+h^2} \end{aligned} \right\} \quad (B7)$$

The lifts of the right and left image vortices are then given, respectively, by

$$L_3 = -\frac{4q_\infty \Gamma_m c_r}{2\pi\beta V_\infty} L\left(\lambda, \frac{r}{s}, \frac{f_i}{s}, \frac{h_i}{s}\right) \quad (B8)$$

$$L_4 = \frac{4q_\infty \Gamma_m c_r}{2\pi\beta V_\infty} L\left(\lambda, \frac{r}{s}, -\frac{f_i}{s}, \frac{h_i}{s}\right) \quad (B9)$$

The total lift due to the wing vortices and their images is

$$L_{T(v)} = \frac{8q_\infty \Gamma_m c_r}{2\pi\beta V_\infty} \left[ L\left(\frac{f}{s}\right) - L\left(-\frac{f}{s}\right) - L\left(\frac{f_i}{s}\right) + L\left(-\frac{f_i}{s}\right) \right] \quad (B10)$$

To obtain the tail interference factor,  $i$ , requires a determination of the lift of the tail alone by strip theory to non-dimensionalize the foregoing lift quantity.

$$(L_T)_\alpha = 2q_\infty \alpha \int_r^s \left(\frac{4}{\beta}\right) c_r d\eta \quad (B11)$$

Integration gives

$$(L_T)_\alpha = \frac{4\alpha q_\infty (s-r)c_r(1+\lambda)}{\beta} \quad (B12)$$

Forming the ratio given by equation (B1) yields the following result for  $i$ :

$$i = \frac{2}{1+\lambda} \left[ L\left(\lambda, \frac{r}{s}, \frac{f}{s}, \frac{h}{s}\right) - L\left(\lambda, \frac{r}{s}, -\frac{f}{s}, \frac{h}{s}\right) - L\left(\lambda, \frac{r}{s}, \frac{f_t}{s}, \frac{h_t}{s}\right) + L\left(\lambda, \frac{r}{s}, -\frac{f_t}{s}, \frac{h_t}{s}\right) \right] \quad (B13)$$

## APPENDIX C

### DETERMINATION OF TAIL INTERFERENCE FACTOR FOR RECTANGULAR TAILS USING ALDEN-SCHINDEL TECHNIQUE

The technique of Alden and Schindel described in reference 12 can be used for estimating the load on the tail section due to wing vortices. Figure 40 shows the model which is analyzed. The assumption is made that the lift due to the vortices originates on the exposed tail panels even though some of this lift might be transmitted to the body. Thus, an integration across the exposed wing panels gives all the lift. This assumption is the same as that made in evaluating the tail interference factor by strip theory and

has been previously discussed. The analysis is carried out with  $\beta=1$  to simplify the algebra, and then  $\beta$  is reintroduced into the final charts. The essential idea of the Alden-Schindel technique is that the total lift acting on a wing of arbitrary twist can be evaluated by a strip technique wherein the weighting factor for the local strip corresponds to the span loading at the strip for the same plan form at uniform angle of attack in reversed flow. In mathematical form this result is stated as

$$L = \int_{\text{span}} w(\eta) F(\eta) d\eta \quad (C1)$$

wherein  $F(\eta)$  is the weighting factor and  $w(\eta)$  is the vertical component of velocity. With reference to figure 40 for model and coordinates, the weighting factor is given for the three regions as

Region I.:

$$F(\eta) = \frac{4q_\infty c}{V_\infty} \quad (C2)$$

Region II.:

$$F(\eta) = \frac{4q_\infty c}{V_\infty} \left[ \frac{1}{\pi} \cos^{-1} \left( 1 + \frac{2\eta}{c} - \frac{2s}{c} \right) + \frac{2}{\pi} \sqrt{\left( \frac{s-\eta}{c} \right)^2 - \left( \frac{s}{c} - \frac{\eta}{c} \right)^2} \right] \quad (C3)$$

Region III.:

$$F(\eta) = \frac{4q_\infty c}{V_\infty} \left[ \frac{1}{\pi} \cos^{-1} \left( 1 - \frac{2\eta}{c} - \frac{2s}{c} \right) + \frac{2}{\pi} \sqrt{\left( \frac{s+\eta}{c} \right)^2 - \left( \frac{s}{c} + \frac{\eta}{c} \right)^2} \right] \quad (C4)$$

The vertical velocity component due to the right external vortex is

$$w(\eta) = -\frac{\Gamma_m(f-\eta)}{2\pi[h^2+(f-\eta)^2]} \quad (C5)$$

To evaluate the lift due to the right external vortex the following integration must be performed:

$$L_1 = \int_{-s}^{-s+c} F(\eta) w(\eta) d\eta + \int_{-s+c}^{-r} F(\eta) w(\eta) d\eta + \int_r^{s-c} F(\eta) w(\eta) d\eta + \int_{s-c}^s F(\eta) w(\eta) d\eta \quad (C6)$$

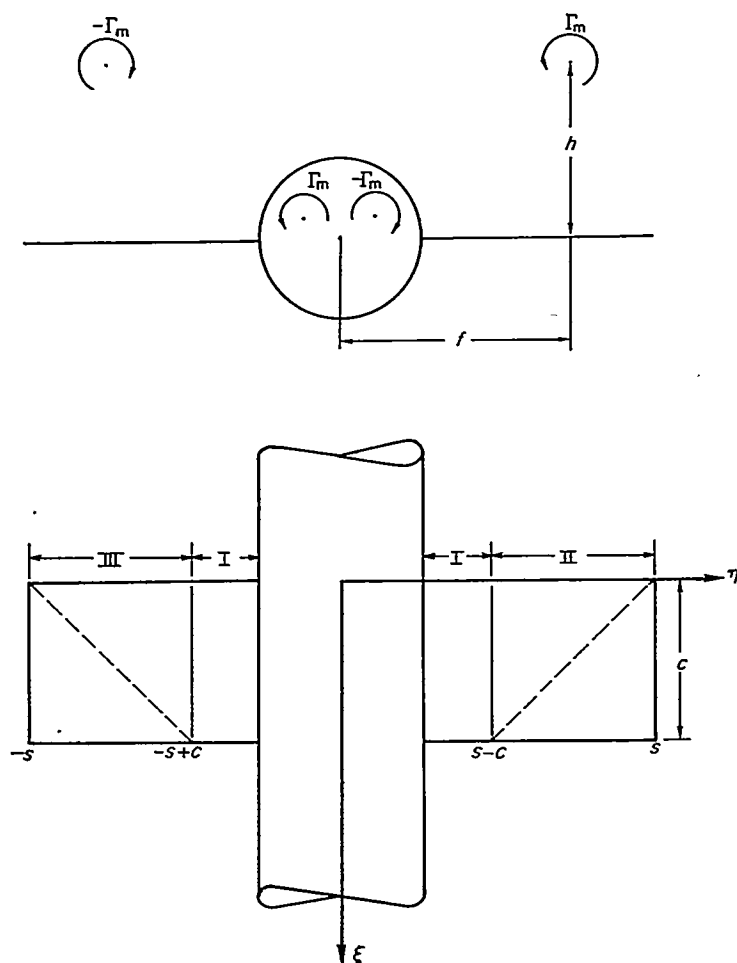


FIGURE 40.—Geometry of model used for determining tail interference factor for rectangular tail by Alden-Schindel technique.

Performing the integrations presents some algebraic difficulty. However, the answer was obtained in closed form in terms of the following function:

$$\chi\left(\frac{f}{c}, \frac{h}{c}, \frac{s}{c}, \frac{r}{c}\right) = \frac{L_1}{\Gamma_m q_\infty s / \pi V_\infty} = \frac{2c}{s} \left\{ \frac{1}{2} \ln \frac{(\delta_2 + 1)^2 + \left(\frac{2h}{c}\right)^2}{(\delta_1 + 1)^2 + \left(\frac{2h}{c}\right)^2} + (\delta_2 - \delta_1) + \right. \\ \left. \frac{1}{2} \ln \left[ \frac{\delta_1^2 + \left(\frac{2h}{c}\right)^2 + \gamma_1 + \sqrt{2}|\delta_1|\sqrt{\alpha_1 + \gamma_1} + \sqrt{2}\left(\frac{2h}{c}\right)\sqrt{-\alpha_1 + \gamma_1}}{\delta_2^2 + \left(\frac{2h}{c}\right)^2 + \gamma_2 + \sqrt{2}|\delta_2|\sqrt{\alpha_2 + \gamma_2} + \sqrt{2}\left(\frac{2h}{c}\right)\sqrt{-\alpha_2 + \gamma_2}} \right] + \right. \\ \left. \frac{\sqrt{2}\delta_1\left(\frac{2h}{c}\right)\sqrt{-\alpha_1 + \gamma_1}}{\gamma_1} + \frac{\alpha_1\delta_1\sqrt{\alpha_1 + \gamma_1}}{\sqrt{2}|\delta_1|\gamma_1} - \frac{\sqrt{2}\delta_2\left(\frac{2h}{c}\right)\sqrt{-\alpha_2 + \gamma_2}}{\gamma_2} \right. \\ \left. \frac{\alpha_2\delta_2\sqrt{\alpha_2 + \gamma_2}}{\sqrt{2}|\delta_2|\gamma_2} + \frac{1}{2} \ln \left[ \frac{h^2 + (f-s+c)^2}{h^2 + (f-r)^2} \times \frac{h^2 + (f+r)^2}{h^2 + (f+s-c)^2} \right] \right\} \quad (C7)$$

where

$$\left. \begin{aligned} \delta_1 &= \frac{2f}{c} - \frac{2s}{c} + 1 \\ \delta_2 &= -\frac{2f}{c} - \frac{2s}{c} + 1 \\ \alpha_{1,2} &= \delta_{1,2}^2 - 1 - \left(\frac{2h}{c}\right)^2 \\ \gamma_{1,2} &= \sqrt{\left[\delta_{1,2}^2 - \left(\frac{2h}{c}\right)^2 - 1\right]^2 + 4\delta_{1,2}^2 \left(\frac{2h}{c}\right)^2} \end{aligned} \right\} \quad (C8)$$

In terms of the function  $\chi$ , the lift is

$$L_1 = \frac{\Gamma_m q_\infty s}{\pi V_\infty} \chi\left(\frac{f}{c}, \frac{h}{c}, \frac{s}{c}, \frac{r}{c}\right) \quad (C9)$$

The contribution of the image vortex to the lift must now be determined. The coordinates of the image vortex to the right are

$$\left. \begin{aligned} f_i &= \frac{r^2 f}{f^2 + h^2} \\ h_i &= \frac{r^2 h}{f^2 + h^2} \end{aligned} \right\} \quad (C10)$$

In terms of these coordinates the lift due to the image vortex, taking into account the change in the sign of the circulation, is

$$L_2 = -\frac{\Gamma_m q_\infty s}{\pi V_\infty} \chi\left(\frac{f_i}{c}, \frac{h_i}{c}, \frac{s}{c}, \frac{r}{c}\right) \quad (C11)$$

The  $\chi$  function is determined in terms of the following parameters:

$$\left. \begin{aligned} \delta_3 &= \frac{2f_i}{c} - \frac{2s}{c} + 1 \\ \delta_4 &= -\frac{2f_i}{c} - \frac{2s}{c} + 1 \\ \alpha_{3,4} &= \delta_{3,4}^2 - 1 - \left(\frac{2h_i}{c}\right)^2 \\ \gamma_{3,4} &= \sqrt{\left[\delta_{3,4}^2 - \left(\frac{2h_i}{c}\right)^2 - 1\right]^2 + 4\delta_{3,4}^2 \left(\frac{2h_i}{c}\right)^2} \end{aligned} \right\} \quad (C12)$$

The lift due to the two external vortices and the two internal vortices is thus

$$2(L_1 + L_2) = \frac{2\Gamma_m q_\infty s}{\pi V_\infty} \left[ \chi\left(\frac{f}{c}, \frac{h}{c}, \frac{s}{c}, \frac{r}{c}\right) - \chi\left(\frac{f_i}{c}, \frac{h_i}{c}, \frac{s}{c}, \frac{r}{c}\right) \right] \quad (C13)$$

The lift so determined is exact within the limits of linear theory. It is necessary to obtain the lift of the wing alone, as given by linear theory, to form the ratio given by the tail interference factor  $i$ .

$$i = \frac{2(L_1 + L_2)/(L_T)_\alpha}{\Gamma_m / 2\pi V_\infty \alpha (s-r)} \quad (C14)$$

The lift-curve slope of a rectangular tail per radian is

$$\frac{dC_L}{d\alpha} = 4 \left( 1 - \frac{1}{2A_T} \right) \quad (C15)$$

so that

$$(L_T)_\alpha = \frac{2c(s-r)q_\infty \alpha \left[ 4 \left( 1 - \frac{r}{s} \right) - \frac{c}{s} \right]}{\left( 1 - \frac{r}{s} \right)} \quad (C16)$$

The lift ratio is obtained by division

$$\frac{2(L_1 + L_2)}{(L_T)_\alpha} = \left[ \frac{\Gamma_m}{\alpha V_\infty (s-r)} \right] \frac{\left( \frac{s}{c} \right) \left( 1 - \frac{r}{s} \right)}{\pi \left[ 4 \left( 1 - \frac{r}{s} \right) - \frac{c}{s} \right]} \left[ \chi\left(\frac{f}{c}, \frac{h}{c}\right) - \chi\left(\frac{f_i}{c}, \frac{h_i}{c}\right) \right] \quad (C17)$$

or

$$i = \frac{2 \left( 1 - \frac{r}{s} \right) \left( \frac{s}{c} \right)}{\left[ 4 \left( 1 - \frac{r}{s} \right) - \frac{c}{s} \right]} \left[ \chi\left(\frac{f}{c}, \frac{h}{c}\right) - \chi\left(\frac{f_i}{c}, \frac{h_i}{c}\right) \right] \quad (C18)$$

## APPENDIX D

## DETERMINATION OF CENTER OF BODY LIFT DUE TO WING AT SUBSONIC SPEEDS

Hitherto, no subsonic method has been available for estimating the center of the lift transferred by a wing or tail to the body. An approximate method for accomplishing this, based on lifting-line theory, is now presented. It is known that a good approximation of the lift and moment characteristics of swept wings at subsonic speeds can be gained by placing a lifting line of variable loading at the wing quarter chord and satisfying the tangency conditions at the three-quarter chord. See, for instance, reference 23. An extension of this model to include the body is shown in figure 15. The image of the quarter-chord line inside the body is obtained by reflecting each point of the quarter-chord line into the body in its cross-flow plane. Since the quarter-chord line is not uniformly loaded, trailing vortices stream backward from the line proportional in strength to the gradient of the span-loading curve. A series of three horseshoe vortices representing the span loading is shown in figure 15. Image vortices inside the body are also illustrated. In the mathematical treatment that follows, the number of vortices increases without limit.

Consider the quarter-chord line with an elliptical loading

$$\Gamma = \Gamma_m \sqrt{1 - \left(\frac{\eta - r}{s - r}\right)^2} \quad (D1)$$

The strength of the bound vortices is proportional to  $\Gamma$ , for both the external flow and the internal flow. The lift due to the bound part of an elementary horseshoe vortex is proportional to the product of its strength times its length

$$dL \sim \Gamma d\eta_i = \Gamma d\left(\frac{r^2}{\eta}\right) = -\Gamma r^2 \frac{d\eta}{\eta^2} \quad (D2)$$

where  $\eta_i$  is the image vortex position and  $\eta$  is the corresponding external vortex position. The lift due to any horseshoe vortex is concentrated at its bound vortex so that the moment about the  $\eta$  axis is

$$dM \sim -\frac{\Gamma r^2 \xi d\eta}{\eta^2} = -\frac{\Gamma r^2 (\eta - r) \tan \Lambda_M d\eta}{\eta^2} \quad (D3)$$

$$\bar{x}_{B(W)} - \frac{c_r}{4} = \frac{M}{L} = \frac{\tan \Lambda_M \int_r^s \frac{\Gamma (\eta - r)}{\eta^2} d\eta}{\int_r^s \frac{\Gamma d\eta}{\eta^2}} \quad (D4)$$

$$\bar{x}_{B(W)} - \frac{c_r}{4} = \tan \Lambda_M \frac{\int_r^s \frac{\sqrt{(s-r)^2 - (\eta-r)^2}}{\eta^2} (\eta-r) d\eta}{\int_r^s \frac{\sqrt{(s-r)^2 - (\eta-r)^2}}{\eta^2} d\eta} \quad (D5)$$

The value of  $\bar{x}_{B(W)}$  as determined by integrating equation (D5) is

$$\bar{x}_{B(W)} = \frac{c_r}{4} + (s-r) \tan \Lambda_M \left[ \frac{r}{r-s} + \frac{\sqrt{s(s-2r)} \cosh^{-1}\left(\frac{s-r}{r}\right) - (s-r) + \frac{\pi r}{2}}{\frac{(s-r)r}{\sqrt{s(s-2r)}} \cosh^{-1}\left(\frac{s-r}{r}\right) + \frac{(s-r)^2}{r} - \frac{\pi}{2}(s-r)} \right]; s > 2r \quad (D6)$$

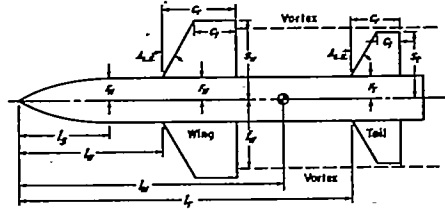
## REFERENCES

1. Wieselsberger, C.: Airplane Body (Non-Lifting System) Drag and Influence on Lifting System. Influence of the Airplane Body on the Wings. Vol. IV of Aerodynamics Theory, div. K, ch. III, sec. 1, W. F. Durand, ed., Julius Springer (Berlin), 1934, pp. 152-157.
2. Hopkins, Edward J., and Carel, Hubert C.: Experimental and Theoretical Study of the Interference at Low Speed Between Slender Bodies and Triangular Wings. NACA RM A53A14, 1953.
3. Nielsen, Jack N., and Pitts, William C.: Wing-Body Interference at Supersonic Speeds with an Application to Combinations with Rectangular Wings. NACA TN 2677, 1952.
4. Ferrari, Carlo: Interference Between Wing and Body at Supersonic Speeds—Theory and Numerical Application. Jour. Aero. Sci., vol. 15, no. 6, June 1948, pp. 317-336.
5. Morikawa, George K.: The Wing-Body Problem for Linearized Supersonic Flow. Ph.D. Thesis, Calif. Inst. of Tech., 1949.
6. Nielsen, Jack N., Katzen, Elliott D., and Tang, Kenneth K.: Lift and Pitching-Moment Interference Between a Pointed Cylindrical Body and Triangular Wings of Various Aspect Ratios at Mach Numbers of 1.50 and 2.02. NACA TN 3795, 1956. (Supersedes NACA RM A50F06)
7. Silverstein, Abe: Toward a Rational Method of Tail-Plane Design. Jour. Aero. Sci., vol. 6, no. 9, July 1939, pp. 361-369.
8. Silverstein, Abe, and Katzoff, S.: Design Charts for Predicting Downwash Angles and Wake Characteristics Behind Plain and Flapped Wings. NACA Rep. 648, 1939.
9. Morikawa, George: Supersonic Wing-Body-Tail Interference. Jour. Aero. Sci., vol. 19, no. 5, May 1952, pp. 333-340.
10. Lomax, Harvard, and Byrd, Paul F.: Theoretical Aerodynamic Characteristics of a Family of Slender Wing-Tail-Body Combinations. NACA TN 2554, 1951.
11. Lagerstrom, Paco A., and Graham, Martha E.: Aerodynamic Interference in Supersonic Missiles. SM-13743, Douglas Aircraft Co., Inc., Santa Monica, July 1950.
12. Alden, Henry L., and Schindel, Leon H.: The Calculations of Wing Lift and Moments in Nonuniform Supersonic Flows. M. I. T. Meteor Rep. 53, May 1950.
13. Spreiter, John R.: The Aerodynamic Forces on Slender Plane- and Cruciform-Wing and Body Combinations. NACA Rep. 962, 1950. (Formerly NACA TN's 1662 and 1897)
14. Morikawa, George: Supersonic Wing-Body Lift. Jour. Aero. Sci., vol. 18, no. 4, Apr. 1951, pp. 217-228.

15. Allen, H. Julian, and Perkins, Edward W.: A Study of Effects of Viscosity on Flow Over Slender Inclined Bodies of Revolution. NACA Rep. 1048, 1951.
16. Jones, Robert T.: Properties of Low-Aspect-Ratio Pointed Wings at Speeds Below and Above the Speed of Sound. NACA Rep. 835, 1946.
17. Beskin, L.: Determination of Upwash Around a Body of Revolution at Supersonic Velocities. Rep. No. CM-251, Johns Hopkins Univ., Applied Physics Lab., May 27, 1946.
18. Nielsen, Jack N.: Quasi-Cylindrical Theory of Wing-Body Interference at Supersonic Speeds and Comparison With Experiment. NACA Rep. 1252, 1956.
19. Lagerstrom, Paco A., and Van Dyke, M. D.: General Considerations About Planar and Non-Planar Lifting Systems. SM-13432, Douglas Aircraft Co., Inc., Santa Monica, June 1949.
20. Jones, Robert T.: Thin Oblique Airfoils at Supersonic Speed. NACA Rep. 851, 1946. (Formerly NACA TN 1107)
21. Lagerstrom, P. A.: Linearized Supersonic Theory of Conical Wings. NACA TN 1685, 1950.
22. Heaslet, Max. A., and Spreiter, John R.: Reciprocity Relations in Aerodynamics. NACA TN 2700, 1952.
23. DeYoung, John, and Harper, Charles W.: Theoretical Symmetric Span Loading at Subsonic Speeds for Wings Having Arbitrary Plan Form. NACA Rep. 921, 1950.
24. Spreiter, John R., and Sacks, Alvin H.: The Rolling-Up of the Trailing Vortex Sheet and Its Effect on Downwash Behind Wings. Jour. Aero. Sci., vol. 18, no. 1, Jan. 1951, pp. 21-32, 72.
25. Rogers, Arthur W.: Application of Two-Dimensional Vortex Theory to the Prediction of Flow Fields Behind Wings of Wing-Body Combinations at Subsonic and Supersonic Speeds. NACA TN 3227, 1954.
26. Lawrence, H. R.: The Lift Distribution on Low Aspect Ratio Wings at Subsonic Speeds. Jour. Aero. Sci., vol. 18, no. 10, Oct. 1951, pp. 683-695.
27. McDavitt, John B.: A Correlation by Means of Transonic Similarity Rules of Experimentally Determined Characteristics of a Series of Symmetrical and Cambered Wings of Rectangular Plan Form. NACA Rep. 1253, 1955.
28. Dugan, Duane W., and Hikido, Katsumi: Theoretical Investigation of the Effects Upon Lift of a Gap Between Wing and Body of a Slender Wing-Body Combination. NACA TN 3224, 1954.
29. Johnson, Ben H., Jr., and Rollins, Francis W.: Investigation of a Thin Wing of Aspect Ratio 4 in the Ames 12-Foot Pressure Wind Tunnel. V—Static Longitudinal Stability and Control Throughout the Subsonic Speed Range of a Semispan Model of a Supersonic Airplane. NACA RM A9I01, 1949.
30. Cahn, Maurice S., and Bryan, Carroll R.: A Transonic-Wing Investigation in the Langley 8-Foot High-Speed Tunnel at High Subsonic Mach Numbers and at a Mach Number of 1.2. Wing-Fuselage Configuration Having a Wing of 0° Sweepback, Aspect Ratio 4.0, Taper Ratio 06, and NACA 65A006 Airfoil Section. NACA RM L51A02, 1951.
31. Weber and Kehl: Wind-Tunnel Measurements on the Henschel Missile "Zitterrochen" in Subsonic and Supersonic Velocities. NACA TM 1159, 1948.
32. Anderson, Adrien E.: An Investigation at Low Speed of a Large-Scale Triangular Wing of Aspect Ratio Two. III. Characteristics of Wing With Body and Vertical Tail. NACA RM A9H04, 1949.
33. Polhamus, Edward C., and King, Thomas J., Jr.: Aerodynamic Characteristics with Fixed and Free Transition of a Modified Delta Wing in Combination with a Fuselage at High Subsonic Speeds. NACA RM L50C21, 1950.
34. House, Rufus O., and Wallace, Arthur R.: Wind Tunnel Investigation of Effect of Interference on Lateral-Stability Characteristics of Four NACA 23012 Wings, and Elliptical and a Circular Fuselage, and Vertical Fins. NACA Rep. 705, 1941.
35. McKay, James M., and Hall, Albert W.: The Effects on the Aerodynamic Characteristics of Reversing the Wing of a Triangular Wing-Body Combination at Transonic Speeds as Determined by the NACA Wing-Flow Method. NACA RM L51H23, 1951.
36. Hall, Albert W., and Morris, Garland J.: Aerodynamic Characteristics at a Mach Number of 1.25 of a 6-Percent-Thick Triangular Wing and 6- and 9-Percent-Thick Triangular Wings in Combination With a Fuselage. Wing Aspect Ratio 2.31, Biconvex Airfoil Sections. NACA RM L50D05, 1950.
37. Ellis, Macon C., Jr., and Grigsby, Carl E.: Aerodynamic Investigation at Mach Number 1.92 of a Rectangular Wing and Tail and Body Configuration and Its Components. NACA RM L9L28a, 1950.
38. Jaeger, B. F., and Brown, A. E.: The Aerodynamic Characteristics at Mach Number 2.0 of 14- and 18-Caliber Fin-Stabilized Rockets with Varying Body and Fin Parameters. U. S. Naval Ordnance Test Station, Inyokern, Calif., NAVORD Rep. 1211, Jan. 20, 1950.
39. Stivers, Louis S., Jr., and Malick, Alexander W.: Wind-Tunnel Investigation at Mach Numbers from 0.50 to 1.29 of an All-Movable Triangular Wing of Aspect Ratio 4 Alone and with a Body. NACA RM A9L01, 1950.
40. Niewald, Roy J., and Moul, Martin T.: The Longitudinal Stability, Control Effectiveness, and Control Hinge-Moment Characteristics Obtained from a Flight Investigation of a Canard Missile Configuration at Transonic and Supersonic Speeds. NACA RM L50I27, 1950.

TABLE I.—WING-BODY-TAIL INTERFERENCE CALCULATING FORM

1	$M_\infty = 1.38$
2	$R = 0.81 \times 10^6$
3	$l_w = 5.25$
4	$S_w = 5.062$
5	$l_t = 10.5$
6	$\beta = \sqrt{M_\infty^2 - 1} = 1.72$



Wing-body				Tail-body				Nose	
7	$r_w = 0.562$	16	$(8) - (7) \cdot (9) + (10)$ $= S_w = 5.062$	23	$r_t = 0.562$	32	$(24) - (23) \cdot (25) + (26)$ $= S_t = 1.562$	39	$r_n = 0.562$
8	$S_w = 2.812$	17	$4 \cdot (9) \cdot (10) \cdot (7) / (15)$ $= \beta A_w = 6.88$	24	$S_t = 1.812$	33	$4 \cdot (26) \cdot (27) \cdot (23) / (32)$ $= \beta A_t = 6.88$	40	$S_n = \pi \cdot (39)^2 = 0.994$
9	$C_f = 0$	18	$\beta A_w / C_f = 2 \cdot (17) / (15) = 0.88$	25	$C_f = 0$	34	$\beta A_t / C_f = 2 \cdot (33) / (32) = 1.54$	41	$l_n = 3.19$
10	$C_f = 2.25$	19	$(17) \cdot (11) / (15) \cdot (1 + (3)) =$ $\beta A \cdot (1 + 1/\alpha \beta) \cdot (1 + \lambda) = 10.87$	26	$C_f = 1.25$	35	$(33) \cdot (1 + 1/(3)) \cdot (1 + (26)) =$ $\beta A \cdot (1 + 1/\alpha \beta) \cdot (1 + \lambda) = 10.87$	42	$V_n = 1.56$
11	$\Delta L/E = 45^\circ$	20	$S_n = 1.375$	27	$\Delta L/E = 45^\circ$	36	$S_t / S_w = (32) / (15) = 0.308$	43	
12	$l_w = 3.75$	21	$(10) - (20) / 57.3 = 0.0153$	28	$l_t = 9.16$	37		44	
13	$\lambda_w = (9) \cdot (10) = C_f / C_f = 0$	22		29	$\lambda_t = (28) / (32) = 0$	38		45	
14	$(r/r)_w = (7) / (8) = 0.2$			30	$(r/r)_t = (29) / (32) = 0.310$	39		46	
15	$(\alpha \beta) = (6) \cdot \cos(11) = 1.72$			31	$(\alpha \beta) = (30) \cdot \cos(27) = 1.72$	40		47	
Instructions				Instructions				Instructions	
47	Chart 1	Items	$K_f(r) = 1.16$	63	Chart 1	Items	$K_f(r) = 1.27$	79	$S_n / S_w = (40) / (4) = 0.196$
48	Chart 1; $M_\infty > 1$ , (19) > 4, Chart 4		$K_f(r) = 0.23$	64	Chart 1; $M_\infty > 1$ , (20) > 4, Chart 4		$K_f(r) = 0.13$	80	$K_w = C_{L_{\alpha w}} \cdot (73) / (80) = 0.163(4)$
49	Chart 1; $\lambda = 1$ , $\beta A > 2$ , Chart 3		$K_f(r) = 0.94$	65	Chart 1; $\lambda = 1$ , $\beta A > 2$ , Chart 3		$K_f(r) = 0.93$	81	$V_n / S_w = (42) / (60) = 1.57(2)$
50	Chart 1		$K_f(r) = 0.23$	66	Chart 1		$K_f(r) = 0.33$	82	$I_n = (41) - (50) = 1.62(2)$
51	$M_\infty < 1$ , Chart 11 or Ref. 23	(3)	$(2/C_f) \cdot r(r)_w = 0.667$	67	$M_\infty < 1$ , Chart 11 or Ref. 23	(3)	$(2/C_f) \cdot r(r)_t = 0.667$	83	$I_n / l_n =$ (a)
52	$M_\infty > 1$ , Chart 10		$(2/C_f) \cdot r(r)_w = 0.667$	68	$M_\infty > 1$ , Chart 10		$(2/C_f) \cdot r(r)_t = 0.667$	84	$I_n = (53) \cdot (4) =$ (b)
53	$(2) + (5) \cdot (10)$		$I_w(r)_a = 5.25$	69	$(2) + (5) \cdot (10)$		$I_t(r)_a = 9.99$	85	$I_n - I_w = (5) - I_w = 3.03$
54	$(2) + (5) \cdot (10)$		$I_w(r)_b = 5.25$	70	$(2) + (5) \cdot (10)$		$I_t(r)_b = 9.99$	86	
55	$(3) - (6)$		$I_w - I_w(r)_a = 0$	71	$(3) - (6)$		$I_t - I_t(r)_a = -4.74$	87	
56	$(3) - (6)$		$I_w - I_w(r)_b = 0$	72	$(3) - (6)$		$I_t - I_t(r)_b = -4.74$		
57	$M_\infty < 1$ , Chart 16;		$(2/C_f) \cdot r(r)_w = 0.938$	73	$M_\infty < 1$ , Chart 16;		$(2/C_f) \cdot r(r)_t = 0.667$		
58	$M_\infty > 1$ , Chart 14 if (9) > 4		$I_w(r) = 5.86$	74	$M_\infty > 1$ , Chart 14 if (9) > 4		$I_t(r) = 9.99$		
59	$M_\infty > 1$ , Chart 15 if (9) < 4		$I_w - I_w(r) = -0.61$	75	$M_\infty > 1$ , Chart 15 if (9) < 4		$I_t - I_t(r) = -4.74$		
60	$M_\infty < 1$ , Chart 5; $M_\infty > 1$ , Chart 6		$(r-r)_w / (r-r)_w = 0.678$	76					
61	$(8) - (7)$		$(s-r)_w = 2.250$	77	$(2) - (3)$		$(s-r)_t = 1.250$		
62	$M_\infty < 1$ , Ref. 23; $M_\infty > 1$ , Chart 8 or experiment ( $C_{L_{\alpha w}} = 0.0406$ )		$(C_{L_{\alpha w}}) / (4) = 0.0406$	78	$M_\infty < 1$ , Ref. 23; $M_\infty > 1$ , Chart 8 or experiment ( $C_{L_{\alpha t}} = 0.0406$ )		$(C_{L_{\alpha t}}) / (4) = 0.0125$	(1)	

Combination — No wing-tail interference											
88	$C_{L_{\alpha w}} = [(90) + (47) + (48) + (62) + (63) + (64) + (78)] / 8 = 0.0606$	91	$C_{L_{\alpha t}} = [(80) + (65) + (67) + (68) + (69) + (72) + (73) + (78)] / 8 = -0.00607$								
89	$C_{L_{\alpha w}} = (49) + (50) + (62) = 0.0475$	92	$C_{L_{\alpha w}} = (49) + (50) + (62) = -0.00054$								
90	$C_{L_{\alpha w}} = (63) + (65) + (78) = 0.0158$	93	$C_{L_{\alpha t}} = (63) + (65) + (78) = -0.00712$								
Lift						Moment					
94	95	96	97	98	99	100	101	102	103	104	105
$\alpha^\circ$	$\delta_w^\circ$	$\delta_r^\circ$	$(2) - (3)$	$(2) - (3)$	$(2) - (3)$	$(2) - (3)$	$(2) - (3)$	$(2) - (3)$	$(2) - (3)$	$(2) - (3)$	$(2) - (3)$
0	4.9	0	0	0.2326	0	0.233	0	-0.0027	0	-0.0027	-0.0116
5						0.637	-0.0304			-0.0331	-0.0525
10						1.041	-0.0607			-0.0634	-0.0609
15						1.445	-0.0911			-0.0938	-0.0649

Combination — With wing-tail interference											
106	$(63) + (65) + (78) + (57.3) = 0.00307$	108	$(1/r)_w = (63) + (65) + (78) = 1.152$ (6)	110							
107	$(63) - (12) - (19) / 57.3 = 0.0697$	109	$l = -2.20$ (Chart 7, $(A/r)_w = 0$ ) (6)	111							
Lift						Moment					
112	113	114	115(6)	116	117	118	119	120	121	122	123
$(67) + (94)$	$(67) + (94)$	$(12) - (19) / 24$	Chart 7	$(67) + (94)$	$(67) + (94)$	$(119) + (117)$	$(67) + (94)$	$(119) + (117)$	$(119) + (117)$	$(67) + (94)$	$(119) + (117)$
0	0.075	-0.042	-2.16	0	4.60	4.80	-0.0306	0.202	0.0138	0.0111	0.0549
.349		.151	-2.02	5.80		10.40	-0.0648	.572	.0292	-.0039	-.0068
.697		.343	-1.71	11.60		16.20	-.0851	.955	-.0384	-.0260	-.0262
1.046		.536	-1.44	17.40		22.00	-.0973	1.347	-.0440	-.0498	-.0370

SUMMARY OF LIFT AND MOMENT COMPONENTS				
	Body	Wing-body	Tail-body minus nose	Wing-body-tail
124	$(C_{L_{\alpha w}})_{\alpha = \delta_w = 0}$	$(60) + (62) = 0.0069$	$(62) + (47) + (48) + (62) = 0.083$	$(88) + (90) + (47) + (48) = 0.073$
125	$(C_{L_{\alpha w}})_{\alpha = \delta_w = 0}$	$(60) + (62) = 0.0024$	$(62) + (47) + (48) + (62) = 0.0018$	$(91) + (106) + (47) + (48) = -0.0025$
126	$(C_{L_{\alpha w}})_{\alpha = \delta_w = 0}$		$(62) = 0.047$	$(88) + (106) + (47) + (48) = 0.041$
127	$(C_{L_{\alpha w}})_{\alpha = \delta_w = 0}$		$(62) = -0.0005$	$(92) + (106) + (47) + (48) = 0.0023$

Notes	
(1)	Lift-curve slope per degree
(2)	Chart for ogival noses
(3)	For greater accuracy use $\lambda = 1$ , $\beta A > 2$ , Chart 12
(4)	Use experimental value per degree based on $S_w$ . If not available, use slender-body values ( $C_{L_{\alpha w}} = 2/57.3$ )
(5)	Ogival nose only, Chart 9.
(6)	For rectangular tails at supersonic speeds and use equations C-7 and C-10 to obtain $l_n$ .

TABLE II.- SUMMARY OF GEOMETRIC AND AERODYNAMIC CHARACTERISTICS AND TEST  
CONDITIONS FOR WING-BODY COMBINATIONS  
(a) Geometric characteristics

No.	Sketch	$M_\infty$	$R \times 10^{-6}$	$\frac{l}{r_N}$	$\frac{l_M}{l}$	$\frac{l_R}{l}$	$\frac{l_W}{l}$	BA	ALB, deg	$\lambda$	$\frac{r}{r_N}$	$\frac{r}{s}$	Source
1a		0.20	1.86	22.5	0.483	0.128	0.440	3.43	9.45	0.546	0.992	0.179	Ref. 29
b		.50	1.86	22.5	.483	.128	.440	3.02	9.45	.546	.992	.179	Ref. 29
c		.70	1.86	22.5	.483	.128	.440	2.49	9.45	.546	.992	.179	Ref. 29
d		.80	1.86	22.5	.483	.128	.440	2.10	9.45	.546	.992	.179	Ref. 29
e		.90	1.86	22.5	.483	.128	.440	1.52	9.45	.546	.992	.179	Ref. 29
2a		1.50	1.0	14.7	---	.182	.450	4.47	45	0	1	.201	Ref. 6
b		2.00	1.0	14.7	---	.182	.450	6.93	45	0	1	.201	Ref. 6
3a		1.20	.59	31.8	---	.062	.912	2.66	45	0	1	.254	Ames 6 x 6 ft
b		1.40	.59	31.8	---	.062	.912	3.92	45	0	1	.254	Ames 6 x 6 ft
c		1.70	.59	31.8	---	.062	.912	5.50	45	0	1	.254	Ames 6 x 6 ft
4a		.60	1.66	20.0	.600	.184	.547	2.85	3.6	.635	1	.139	Ref. 30
b		.70	1.79	20.0	.600	.184	.547	2.55	3.6	.635	1	.139	Ref. 30
c		.80	1.88	20.0	.600	.184	.547	2.14	3.6	.635	1	.139	Ref. 30
d		.90	1.93	20.0	.600	.184	.547	1.56	3.6	.635	1	.139	Ref. 30
e		1.20	1.86	20.0	.600	.184	.547	2.37	3.6	.635	1	.139	Ref. 30
5a		.50	4.25	19.6	1.000	.102	.380	1.73	26.5	0	1	.243	Ref. 31
b		.70	---	19.6	1.000	.102	.380	1.43	26.5	0	1	.243	Ref. 31
c		.90	6.58	19.6	1.000	.102	.380	.87	26.5	0	1	.243	Ref. 31
d		1.45	2.76	19.6	1.000	.102	.380	2.10	26.5	0	1	.243	Ref. 31
e		1.99	2.34	19.6	1.000	.102	.380	3.45	26.5	0	1	.243	Ref. 31
6a		.50	5.60	19.6	1.000	.102	.355	.87	45	0	1	.327	Ref. 31
b		.70	---	19.6	1.000	.102	.355	.71	45	0	1	.327	Ref. 31
c		.90	8.67	19.6	1.000	.102	.355	.44	45	0	1	.327	Ref. 31
d		1.45	3.64	19.6	1.000	.102	.355	1.05	45	0	1	.327	Ref. 31
e		1.99	3.08	19.6	1.000	.102	.355	1.72	45	0	1	.327	Ref. 31
7		.13	12.7	25.0	.532	.291	.392	2.00	63	0	1	.196	Ref. 32
8a		.40	2.84	16.7	.521	.274	.386	2.51	35	.352	1	.160	Ref. 33
b		.60	3.67	16.7	.521	.274	.386	2.19	35	.352	1	.160	Ref. 33
c		.80	4.65	16.7	.521	.274	.386	1.64	35	.352	1	.160	Ref. 33
d		.90	4.89	16.7	.521	.274	.386	1.19	35	.352	1	.160	Ref. 33
9		.10	.57	11.7	.322	.233	.260	5.62	0	.88	1	.115	Ref. 34
10		.10	.62	11.7	.322	.244	.185	5.52	18.3	.38	1	.115	Ref. 34
11		.10	.62	11.7	.322	.244	.223	5.52	9.3	.38	1	.115	Ref. 34
12		.10	.62	11.7	.322	.244	.261	5.52	0	.38	1	.115	Ref. 34
13a		.75	1.27	24.0	.606	.291	.388	1.49	60	0	.981	.158	Ref. 35
b		.85	1.31	24.0	.606	.291	.388	1.18	60	0	.981	.158	Ref. 35
c		1.07	1.25	24.0	.606	.291	.388	.83	60	0	.981	.158	Ref. 35
14a		.75	1.31	24.0	.637	.276	.499	1.60	0	0	.861	.139	Ref. 35
b		.85	1.44	24.0	.637	.276	.499	1.26	0	0	.861	.139	Ref. 35
c		1.07	1.29	24.0	.637	.276	.499	.90	0	0	.861	.139	Ref. 35
15		1.25	.88	24.0	---	.290	.385	1.73	60	0	.970	.163	Ref. 36

TABLE II.—SUMMARY OF GEOMETRIC AND AERODYNAMIC CHARACTERISTICS AND TEST  
CONDITIONS FOR WING-BODY COMBINATIONS - Continued  
(b) Aerodynamic characteristics -  $\alpha$  variable

No.	$K_M$	$K_B(W)$	$K_W(B)$	Theoretical								Experimental			
				Lift				Center of pressure				Lift			c.p.
				$(BC_{L\alpha})_W$	$(BC_{L\alpha})_H$	$(BC_{L\alpha})_{W(B)}$	$(BC_{L\alpha})_C$	$\frac{\bar{L}_H}{l}$	$\frac{\bar{L}_B(W)\alpha}{l}$	$\frac{\bar{L}_B(B)\alpha}{l}$	$\frac{\bar{L}_C\alpha}{l}$	$(BC_{L\alpha})_B$	$(BC_{L\alpha})_{W(B)}$	$(BC_{L\alpha})_C$	
1a	0.08	0.24	1.14	3.47	0.27	---	5.05	0.229	0.480	0.485	0.47	---	---	4.70	0.47
b	.07	.24	1.14	3.16	.23	---	4.59	.229	.479	.485	.47	---	---	4.35	.47
c	.07	.24	1.14	2.83	.19	---	4.10	.229	.478	.485	.47	---	---	3.94	.47
d	.06	.24	1.14	2.51	.16	---	3.62	.229	.477	.485	.47	---	---	3.56	.47
e	.06	.24	1.14	2.02	.12	---	2.90	.229	.474	.485	.47	---	---	3.08	.47
2a	.11	.23	1.16	4.00	.44	---	6.01	.190	.675	.636	.60	.43	---	5.69	.60
b	.17	.23	1.16	4.00	.68	---	6.24	.190	.710	.636	.59	.90	---	7.09	.60
3a	.15	.20	1.21	3.10	.48	---	4.86	.207	.966	.969	.89	---	---	4.91	.90
b	.18	.18	1.21	3.96	.71	---	6.22	.207	.968	.969	.87	---	---	6.21	.87
c	.25	.14	1.21	4.00	1.00	---	6.40	.207	.969	.969	.84	---	---	7.26	.85
4a	.04	.19	1.11	3.07	.11	---	4.11	.236	.598	.601	.59	---	---	<sup>a</sup> 4.01	.57
b	.04	.19	1.11	2.88	.10	---	3.85	.236	.597	.601	.59	---	---	<sup>a</sup> 3.72	.58
c	.03	.19	1.11	2.58	.09	---	3.45	.236	.595	.601	.59	---	---	<sup>a</sup> 3.73	.57
d	.03	.19	1.11	2.07	.06	---	2.75	.236	.590	.601	.59	---	---	<sup>a</sup> 3.12	.60
e	.03	.18	1.11	3.28	.10	---	4.33	.236	.690	.638	.62	---	---	<sup>a</sup> 3.77	.62
5a	.14	.35	1.20	1.97	.28	---	3.34	.102	.452	<sup>a</sup> (.428)	.40	---	---	3.36	.40
b	.14	.35	1.20	1.70	.23	---	2.86	.102	.447	<sup>a</sup> (.428)	.40	---	---	3.04	.40
c	.12	.35	1.20	1.13	.16	---	1.89	.102	.441	<sup>a</sup> (.428)	.40	---	---	2.18	.40
d	.13	.35	1.20	2.69	.34	---	4.50	.102	.606	<sup>a</sup> (.477)	.47	---	---	4.40	.43
e	.15	.35	1.20	3.71	.55	---	6.31	.102	.632	<sup>a</sup> (.477)	.47	---	---	5.95	.43
6a	.27	.49	1.28	1.22	.33	---	2.48	.102	.434	.456	.40	---	---	2.49	.41
b	.26	.49	1.28	1.02	.27	---	2.08	.102	.430	.454	.40	---	---	2.05	.40
c	.25	.49	1.28	.65	.16	---	1.32	.102	.424	.445	.40	---	---	1.50	.41
d	.20	.49	1.28	2.01	.40	---	3.96	.102	.558	.473	.45	---	---	3.35	.44
e	.23	.49	1.28	2.83	.65	---	5.66	.102	.609	.491	.47	---	---	5.12	.45
7	.07	.25	1.15	2.19	.15	---	3.22	.206	.546	.591	.56	---	---	3.38	.56
8a	.05	.22	1.13	2.72	.14	---	3.81	---	.506	.541	---	---	---	3.84	.52
b	.05	.22	1.13	2.51	.13	---	3.51	---	.505	.541	---	---	---	3.64	.52
c	.04	.22	1.13	2.07	.09	---	2.88	---	.506	.541	---	---	---	3.15	.52
d	.04	.22	1.13	1.63	.07	---	2.26	---	.507	.540	---	---	---	2.63	.51
9	.14	.15	1.09	4.13	.60	---	5.30	.100	.322	.319	.31	---	---	5.81	.32
10	.14	.15	1.09	4.12	.58	---	5.27	.100	.290	.338	.33	---	---	4.83	.32
11	.14	.15	1.09	4.12	.58	---	5.27	.100	.316	.334	.33	---	---	4.83	.32
12	.14	.15	1.09	4.12	.58	---	5.27	.100	.341	.325	.32	---	---	4.83	.32
13a	.05	.23	1.13	1.76	.09	---	2.48	.217	.548	.592	.57	---	---	2.40	.56
b	.05	.23	1.13	1.46	.07	---	2.06	.217	.552	.595	.57	---	---	1.95	.56
c	.04	.21	1.13	1.22	.05	---	1.68	.217	.584	.631	.60	---	---	1.53	.59
14a	.05	.19	1.11	1.84	.09	---	2.48	.217	.566	.558	.54	---	---	2.38	.50
b	.05	.19	1.11	1.53	.07	---	2.05	.217	.560	.556	.54	---	---	2.19	.50
c	.04	.19	1.11	1.31	.05	---	1.74	.217	.578	.539	.52	---	---	1.76	.53
15	---	.20	1.17	2.33	.11	---	3.29	---	---	---	---	---	---	3.09	---

<sup>a</sup> $BC_{L\alpha}$  per radian based on exposed wing area.

<sup>a</sup>( ) denotes experimental value used in theory for combination.

<sup>a</sup>Experimental data nonlinear near  $\alpha = 0$ .



TABLE II.- SUMMARY OF GEOMETRIC AND AERODYNAMIC CHARACTERISTICS AND TEST  
CONDITIONS FOR WING-BODY COMBINATIONS - Continued -  
(c) Geometric characteristics

No.	Sketch	$M_\infty$	$R \times 10^{-5}$	$\frac{l}{r_H}$	$\frac{l_R}{l}$	$\frac{l_W}{l}$	$\beta A$	$\Delta \alpha_E$ , deg	$\lambda$	$\frac{x}{r_H}$	$\frac{x}{s}$	Source
16		1.93	0.19	25.0	0.067	0.440	9.41	0	1	1	0.172	Langley 9 in.
17		1.93	.19	25.0	.067	.440	7.35	0	1	1	.210	Langley 9 in.
18		1.93	.19	25.0	.067	.440	5.24	0	1	1	.273	Langley 9 in.
19		1.93	.19	25.0	.143	.408	5.64	0	1	1	.382	Langley 9 in.
20		1.92	.40	25.0	.067	.440	3.16	0	1	1	.140	Ref. 37
21a		1.62	.40	19.5	.146	.501	1.66	0	1	1	.350	Langley 9 in.
b		1.93	.40	19.5	.146	.501	2.14	0	1	1	.350	Langley 9 in.
c		2.40	.40	19.5	.146	.501	2.84	0	1	1	.350	Langley 9 in.
22a		2.00	.79	23.3	.360	.468	4.76	0	1	1	.083	Ames 1 x 3 ft
b		1.50	.91	23.3	.360	.468	3.08	0	1	1	.083	Ames 1 x 3 ft
23a		1.93	.18	25.1	.067	.438	3.17	0	1	1	.382	Langley 9 in.
b		1.62	.21	25.1	.067	.438	2.45	0	1	1	.382	Langley 9 in.
24		2.00	---	27.9	.143	.860	1.73	0	1	1	.333	Ref. 38
25		2.00	---	27.9	.143	.860	3.46	0	1	1	.200	Ref. 38
26		1.50	.26	22.9	.034	.148	2.98	26.6	.500	.986	.486	Ames 1 x 3 ft
27a		1.50	.70	22.9	.092	.632	3.30	14.0	.461	1	.250	Ames 1 x 3 ft
b		2.00	.70	22.9	.092	.632	5.11	14.0	.461	1	.250	Ames 1 x 3 ft
28a		1.50	.56	22.9	.074	.645	2.98	20.5	.500	1	.314	Ames 1 x 3 ft
b		2.00	.56	22.9	.074	.645	4.61	20.5	.500	1	.314	Ames 1 x 3 ft
29a		1.62	.31	21.8	.094	.870	1.57	60	.305	1	.465	Langley 9 in.
b		1.93	.28	21.8	.094	.870	2.03	60	.305	1	.465	Langley 9 in.
30		1.93	.33	21.8	.113	.487	1.69	15	.323	1	.465	Langley 9 in.
31		1.93	.24	22.9	.078	.888	3.16	45	.352	1	.388	Langley 9 in.
32		1.93	.83	22.9	.270	.633	1.03	70	.400	1	.356	Langley 9 in.
33a		1.93	.30	24.8	.111	.407	2.57	60	0	1	.382	Langley 9 in.
b		1.62	.34	24.8	.111	.407	1.99	60	0	1	.382	Langley 9 in.
34a		1.50	1.0	14.7	.182	.450	.75	80.4	0	1	.600	Ref. 6
b		2.00	1.0	14.7	.182	.450	1.16	80.4	0	1	.600	Ref. 6
35a		1.50	1.0	14.7	.182	.450	1.50	71.6	0	1	.428	Ref. 6
b		2.00	1.0	14.7	.182	.450	2.32	71.6	0	1	.428	Ref. 6
36a		1.50	1.0	14.7	.182	.450	2.26	63.2	0	1	.333	Ref. 6
b		2.00	1.0	14.7	.182	.450	3.50	63.2	0	1	.333	Ref. 6
37a		1.50	1.0	14.7	.182	.450	3.01	56	0	1	.272	Ref. 6
b		2.00	1.0	14.7	.182	.450	4.66	56	0	1	.272	Ref. 6
38a		1.50	1.0	14.7	.182	.450	3.72	50	0	1	.231	Ref. 6
b		2.00	1.0	14.7	.182	.450	5.77	50	0	1	.231	Ref. 6

TABLE II.— SUMMARY OF GEOMETRIC AND AERODYNAMIC CHARACTERISTICS AND TEST  
CONDITIONS FOR WING-BODY COMBINATIONS - Continued  
(d) Aerodynamic characteristics -  $\alpha$  variable

No.	$K_H$	$K_B(W)$	$K_W(B)$	Theoretical								Experimental				
				$^2Lift$				Center of pressure				$^2Lift$				c.p.
				$(\beta C_{L\alpha})_W$	$(\beta C_{L\alpha})_H$	$(\beta C_{L\alpha})_{W(B)}$	$(\beta C_{L\alpha})_C$	$\frac{\bar{Y}_H}{l}$	$\frac{\bar{Y}_{B(W)\alpha}}{l}$	$\frac{\bar{Y}_{W(B)\alpha}}{l}$	$\frac{\bar{Y}_{Ca}}{l}$	$(\beta C_{L\alpha})_B$	$(\beta C_{L\alpha})_{W(B)}$	$(\beta C_{L\alpha})_C$	$\frac{\bar{Y}_{Ca}}{l}$	
16	0.17	0.12	1.14	3.79	0.64	---	5.40	0.192	0.532	0.473	0.41	0.64	---	5.44	0.41	
17	.22	.16	1.17	3.73	.82	---	5.76	.192	.532	.473	.41	.82	---	5.47	.41	
18	.32	.22	1.23	3.62	1.15	---	6.41	.192	.532	.473	.40	1.15	---	6.69	.42	
19	.56	.40	1.33	3.37	1.90	---	7.73	.192	.532	.473	.38	1.90	---	7.16	.36	
20	.06	.12	1.11	3.65	.23	---	4.71	.192	.547	.473	.44	.23	---	4.37	.46	
21a	.27	.52	1.30	2.79	.76	---	5.84	.207	.646	.568	.51	.80	---	4.71	.49	
b	.32	.44	1.30	3.07	.98	---	6.32	.207	.657	.566	.50	1.05	---	5.66	.50	
c	.39	.38	1.30	3.30	1.29	---	6.84	.207	.679	.568	.49	1.34	---	6.72	.51	
22a	---	.08	1.06	3.58	.06	---	4.14	---	---	---	---	---	---	4.11	---	
b	---	.09	1.06	3.35	.04	---	3.89	---	---	---	---	---	---	4.05	---	
23a	.56	.40	1.33	3.37	1.90	---	7.73	.191	.528	.467	.38	2.04	---	7.93	.37	
b	.46	.45	1.33	3.18	1.47	---	7.13	.191	.518	.467	.39	1.53	---	6.97	.37	
24	.24	.25	1.28	2.84	.68	---	5.02	.083	.992	.920	.78	.68	---	5.48	.80	
25	.10	.11	1.16	3.42	.34	---	4.67	.083	.953	.928	.83	.34	---	4.88	.84	
26	1.38	.56	1.44	3.49	4.83	---	11.81	.090	.213	.175	.13	4.98	---	11.05	.13	
27a	.16	.29	1.21	3.56	.57	---	5.91	.090	.742	.688	.62	.59	---	6.10	.62	
b	.24	.27	1.21	3.78	.89	---	6.48	.090	.766	.691	.60	1.09	---	7.15	.61	
28a	.28	.41	1.27	3.50	.98	---	6.86	.090	.743	.697	.60	1.01	---	7.15	.59	
b	.41	.32	1.27	3.72	1.51	---	7.42	.090	.759	.692	.56	1.86	---	8.20	.58	
29a	.71	.31	1.41	2.62	1.87	---	6.38	.165	.956	.949	.69	2.15	---	6.12	.68	
b	.78	.16	1.41	3.12	2.42	---	7.32	.165	.960	.949	.67	2.91	---	7.78	.64	
30	.68	.63	1.41	2.94	2.01	---	8.01	.165	.644	.541	.45	2.41	---	7.74	.41	
31	.54	.16	1.34	3.67	1.99	---	7.50	.114	.972	.954	.71	2.39	---	6.80	.66	
32	.25	.41	1.31	1.94	.49	---	3.88	.114	.889	.827	.73	.59	---	3.90	.73	
33a	.44	.52	1.33	3.53	1.54	---	8.06	.172	.561	.497	.44	1.67	---	7.69	.43	
b	.39	.54	1.33	3.05	1.19	---	6.89	.172	.544	.494	.44	1.16	---	6.50	.43	
34a	2.33	.97	1.56	1.13	2.63	---	5.48	.190	.675	.636	.42	2.56	---	6.35	.44	
b	2.44	.94	1.56	1.67	4.08	---	8.25	.190	.710	.636	.42	5.38	---	10.02	.41	
35a	.64	.60	1.38	2.07	1.32	---	5.41	.190	.675	.636	.53	1.29	---	5.86	.53	
b	.71	.52	1.38	2.88	2.04	---	7.52	.190	.710	.636	.52	2.69	---	8.33	.53	
36a	.31	.41	1.29	2.83	.88	---	5.69	.190	.675	.636	.56	.86	---	5.77	.56	
b	.36	.37	1.29	3.73	1.36	---	7.54	.190	.710	.636	.56	1.79	---	8.24	.57	
37a	.19	.32	1.23	3.42	.66	---	5.95	.190	.675	.636	.58	.64	---	5.71	.58	
b	.26	.30	1.23	4.00	1.02	---	7.14	.190	.710	.636	.57	1.35	---	7.76	.58	
38a	.14	.26	1.19	3.86	.53	---	6.13	.190	.675	.636	.59	.52	---	5.69	.60	
b	.20	.26	1.19	4.00	.82	---	6.62	.190	.710	.636	.58	1.08	---	7.55	.60	

<sup>1</sup> See footnote 1, bottom of Table II(b).

TABLE II.- SUMMARY OF GEOMETRIC AND AERODYNAMIC CHARACTERISTICS AND TEST  
CONDITIONS FOR WING-BODY COMBINATIONS - Continued  
(e) Geometric characteristics

No.	Sketch	$M_\infty$	$R \times 10^{-3}$	$\frac{l}{r_H}$	$\frac{l_R}{l}$	$\frac{l_H}{l}$	SA	$\Delta LE$ , deg	$\lambda$	$\frac{x}{r_H}$	$\frac{x}{l}$	Source
39a		1.15	1.26	31.9	0.132	0.365	1.31	60	0	1	0.216	Ames 6 x 6 ft
b		1.2	1.26	31.9	.132	.365	1.53	60	0	1	.216	Ames 6 x 6 ft
c		1.3	1.26	31.9	.132	.365	1.92	60	0	1	.216	Ames 6 x 6 ft
d		1.4	1.26	31.9	.132	.365	2.26	60	0	1	.216	Ames 6 x 6 ft
e		1.53	1.26	31.9	.132	.365	2.68	60	0	1	.216	Ames 6 x 6 ft
f		1.7	1.26	31.9	.132	.365	3.18	60	0	1	.216	Ames 6 x 6 ft
40		2.07	.64	18.7	.143	.357	7.25	45	0	1	.200	Ames 1 x 3 ft
41a		1.20	1.09	24.0	.111	.333	2.65	45	0	1	.200	Ref. 39
b		1.24	1.09	24.0	.111	.333	2.93	45	0	1	.200	Ref. 39
c		1.29	1.09	24.0	.111	.333	3.26	45	0	1	.200	Ref. 39
42		1.92	.2	25.0	.070	.920	5.13	0	1	1	.228	Ref. 37
43a		1.40	1.25	31.8	.132	.365	2.27	60	0	1	.216	Ames 6 x 6 ft
b		1.53	1.25	31.8	.132	.365	2.68	60	0	1	.216	Ames 6 x 6 ft
c		1.70	1.25	31.8	.132	.365	3.18	60	0	1	.216	Ames 6 x 6 ft
44		1.40	1.25	31.8	.132	.412	2.27	0	0	1	.216	Ames 6 x 6 ft
45a		1.40	1.51	31.8	.197	.389	1.13	0	1	1	.216	Ames 6 x 6 ft
b		1.90	1.51	31.8	.197	.389	1.87	0	1	1	.216	Ames 6 x 6 ft

TABLE II.— SUMMARY OF GEOMETRIC AND AERODYNAMIC CHARACTERISTICS AND TEST  
CONDITIONS FOR WING-BODY COMBINATIONS - Concluded  
(f) Aerodynamic characteristics -  $\alpha$  variable

No.	$K_N$	$K_B(W)$	$K_W(B)$	Theoretical								Experimental			
				<sup>1</sup> Lift				Center of pressure				<sup>1</sup> Lift		c.p.	
				$(\beta C_{L\alpha})_W$	$(\beta C_{L\alpha})_B$	$(\beta C_{L\alpha})_{W(B)}$	$(\beta C_{L\alpha})_C$	$\frac{\bar{t}_H}{l}$	$\frac{\bar{t}_B(W)\alpha}{l}$	$\frac{\bar{t}_W(B)\alpha}{l}$	$\frac{\bar{t}_{Ca}}{l}$	$(\beta C_{L\alpha})_B$	$(\beta C_{L\alpha})_{W(B)}$	$(\beta C_{L\alpha})_C$	$\frac{\bar{t}_{Ca}}{l}$
39a	0.09	0.27	1.18	1.86	0.16	---	2.84	0.206	0.489	0.498	0.47	---	---	3.01	0.47
b	.09	.26	1.18	2.11	.18	---	3.22	.206	.492	.498	.47	---	---	3.39	.48
c	.09	.25	1.18	2.51	.23	---	3.83	.206	.497	.498	.47	---	---	3.95	.47
d	.10	.25	1.18	2.83	.27	---	4.31	.206	.502	.498	.47	---	---	4.41	.46
e	.10	.25	1.18	3.17	.32	---	4.84	.206	.507	.498	.47	---	---	4.88	.46
f	.11	.24	1.18	3.53	.38	---	5.38	.206	.514	.498	.47	---	---	5.36	.46
40	.18	.23	1.16	4.00	.71	4.65	6.28	.15	.561	.497	.46	---	---	7.31	---
41a	.17	.24	1.16	3.16	.52	3.66	4.95	.14	.448	.441	.40	---	---	---	---
b	.17	.22	1.16	3.37	.58	3.91	5.25	.14	.451	.441	.40	---	---	---	---
c	.18	.22	1.16	3.57	.64	4.14	5.58	.14	.455	.441	.40	---	---	---	---
42	.29	.07	1.19	3.61	1.06	4.30	5.61	.19	.954	.954	.78	---	---	5.61	.75
43a	.10	.25	1.18	2.83	.27	3.34	4.31	.21	.501	.493	.47	---	3.54	4.41	.46
b	.10	.25	1.18	3.17	.32	3.74	4.84	.21	.505	.493	.47	---	3.85	4.88	.46
c	.11	.24	1.18	3.53	.38	4.16	5.38	.21	.513	.493	.47	---	4.02	5.36	.46
44	.10	.31	1.18	2.83	.27	3.34	4.48	.21	.548	.457	.45	---	3.03	4.60	.45
45a	.06	.31	1.18	2.23	.13	2.63	3.48	.21	.525	.460	.43	---	2.69	3.59	.45
b	.08	.31	1.18	2.93	.22	3.46	4.58	.21	.545	.475	.45	---	3.43	4.54	.47

(g) Aerodynamic characteristics -  $\delta$  variable

No.	$K_B(W)$	$K_W(B)$	Theoretical						Experimental			
			<sup>1</sup> Lift		Center of pressure		$\frac{\bar{t}_{Ca}}{l}$	$(\beta C_{L\delta})_{W(B)}$	$(\beta C_{L\delta})_C$	<sup>1</sup> Lift		c.p.
			$(\beta C_{L\delta})_{W(B)}$	$(\beta C_{L\delta})_C$	$\frac{\bar{t}_B(W)\delta}{l}$	$\frac{\bar{t}_W(B)\delta}{l}$				$(\beta C_{L\delta})_{W(B)}$	$(\beta C_{L\delta})_C$	$\frac{\bar{t}_W(B)\delta}{l}$
40	0.22	0.94	3.78	4.65	0.561	0.500	0.50	---	4.87	0.765	---	---
41a	.22	.94	2.98	3.66	.448	.444	.44	2.13	2.74	.438	---	---
b	.22	.94	3.18	3.91	.451	.444	.44	2.27	2.86	.439	---	---
c	.22	.94	3.37	4.14	.455	.444	.44	2.43	3.00	---	---	---
42	.25	.98	3.53	4.43	.954	.953	.96	---	3.03	---	.98	---
43a	.24	.94	2.67	3.34	.501	.497	.49	2.47	2.81	.494	.48	---
b	.24	.94	2.99	3.74	.505	.497	.49	---	3.05	---	.49	---
c	.24	.94	3.33	4.16	.513	.497	.49	---	3.47	---	.49	---
44	.24	.94	2.67	3.34	.548	.467	.47	2.58	3.26	.450	.48	---
45a	.24	.94	2.10	2.63	.525	.457	.44	2.25	2.75	.458	.46	---
b	.24	.94	2.76	3.46	.545	.475	.46	2.96	3.52	.467	.48	---

<sup>1</sup> See footnote 1, bottom of Table II(b).

## LIFT AND CENTER OF PRESSURE OF WING-BODY-TAIL COMBINATIONS

TABLE III.- SUMMARY OF GEOMETRIC AND AERODYNAMIC CHARACTERISTICS AND TEST CONDITIONS FOR WING-BODY-TAIL COMBINATIONS  
(a) Geometric characteristics

No.	Sketch	$M_\infty$	$R \times 10^{-6}$	$\frac{1}{r_H}$	$\frac{l_M}{l}$	$\frac{l_R}{l}$	$\frac{S_T}{S_W}$	Surface	$\frac{l_W}{l}$ or $\frac{l_T}{l}$	$\frac{t}{c}$	$\beta A$	$\Delta L_E$ , deg	$\lambda$	$\frac{r}{r_H}$	$\frac{r}{R}$	Source
101		1.99	.81	18.6	.500	1.000	.309	wing tail	.357 .872	.08 .08	6.88 6.88	45 45	0 0	1 1	.200 .310	Ames 1 x 3 ft
102a		.20	1.86	22.5	.483	.128	.252	wing tail	.440 .895	.042 .042	3.43 3.43	9.45 9.45	.546 .548	.992 .488	.179 .176	Ref. 29
b		.50	1.86	22.5	.483	.128	.252	wing tail	.440 .895	.042 .042	3.02 3.03	9.45 9.45	.546 .548	.992 .488	.179 .176	Ref. 29
c		.70	1.86	22.5	.483	.128	.252	wing tail	.440 .895	.042 .042	2.49 2.50	9.45 9.45	.546 .548	.992 .488	.179 .176	Ref. 29
d		.80	1.86	22.5	.483	.128	.252	wing tail	.440 .895	.042 .042	2.10 2.10	9.45 9.45	.546 .548	.992 .488	.179 .176	Ref. 29
e		.90	1.86	22.5	.483	.128	.252	wing tail	.440 .895	.042 .042	1.52 1.53	9.45 9.45	.546 .548	.992 .488	.179 .176	Ref. 29
103a		.89	6.0	32.6	.525	.157	9.00	wing tail	.226 .597	--- ---	1.05 1.05	60 60	0 0	1 1	.467 .226	Ref. 40
b		1.25	9.2	32.6	.525	.157	9.00	wing tail	.226 .597	--- ---	1.73 1.73	60 60	0 0	1 1	.467 .226	Ref. 40
104		1.90	1.51	31.8	.508	.197	.392	wing tail	.389 .809	.03 .02	1.87 .78	0 0	1 1	1 1	.216 .405	Ames 6 x 6 ft
105		1.93	.33	21.9	.522	.091	.839	wing tail	.486 .869	--- .049	1.69 2.03	60 60	.323 .305	1 1	.465 .465	Langley 9 in.
106		1.93	.33	22.8	.541	.088	.931	wing tail	.507 .947	--- .064	1.69 5.51	60 0	.323 0	1 1	.465 .333	Langley 9 in.
107		1.93	.33	22.8	.541	.088	1.01	wing tail	.507 .893	--- ---	1.69 3.16	60 45	.323 .322	1 1	.465 .388	Langley 9 in.
108		1.93	.83	22.8	.541	.088	5.74	wing tail	.290 .636	--- ---	1.69 1.03	60 70	.323 .400	1 1	.508 .356	Langley 9 in.
109		1.93	.83	22.8	.541	.088	23.10	wing tail	.404 .636	--- ---	3.81 1.03	60 70	0 .400	1 1	.579 .356	Langley 9 in.
110		1.93	.83	22.8	.541	.088	10.30	wing tail	.376 .636	--- ---	3.81 1.03	60 70	0 .400	1 1	.479 .356	Langley 9 in.
111		1.93	.83	22.8	.541	.088	5.79	wing tail	.349 .636	--- ---	3.81 1.03	60 70	0 .400	1 1	.408 .356	Langley 9 in.
112		1.92	.40	25.0	.477	.143	.221	wing tail	.408 .920	.06 .06	5.64 5.14	0 0	1 1	1 .814	.140 .228	Ref. 37
113		1.92	.40	25.0	.563	.143	.221	wing tail	.494 .920	.06 .06	5.64 5.14	0 0	1 1	1 .814	.140 .228	Ref. 37
114		1.92	.40	25.0	.649	.143	.221	wing tail	.648 .920	.06 .06	5.64 5.14	0 0	1 1	1 .814	.140 .228	Ref. 37
115		1.62	.23	25.7	.486	.078	1	wing tail	.355 .880	--- ---	3.31 3.31	0 0	0 0	1 1	.350 .350	Langley 9 in.
116		1.62	.23	25.7	.486	.078	1	wing tail	.355 .880	--- ---	3.31 3.31	0 0	0 0	1 1	.350 .350	Langley 9 in.
117		1.62	.23	25.7	.486	.078	1	wing tail	.355 .880	--- ---	3.31 3.31	57 0	0 0	1 1	.350 .350	Langley 9 in.
118		1.62	.23	25.7	.486	.078	1	wing tail	.355 .880	--- ---	3.31 3.31	57 0	0 0	1 1	.350 .350	Langley 9 in.
119		1.62	.23	25.7	.486	.078	1	wing tail	.355 .880	--- ---	3.31 3.31	57 0	0 0	1 1	.350 .350	Langley 9 in.
120		1.62	.23	25.7	.486	.078	1	wing tail	.355 .880	--- ---	3.31 3.31	57 0	0 0	1 1	.350 .350	Langley 9 in.
121		1.62	.35	25.7	.486	.078	1	wing tail	.355 .880	.06 .06	1.66 1.66	0 0	1 1	1 1	.350 .350	Langley 9 in.
122		1.62	.35	25.7	.486	.078	1	wing tail	.355 .880	.06 .06	1.66 1.66	0 0	1 1	1 1	.350 .350	Langley 9 in.
123		1.62	.52	25.7	.486	.078	.667	wing tail	.327 .880	.03 .03	1.11 1.66	0 0	1 1	1 1	.350 .350	Langley 9 in.
124		1.62	.52	25.7	.486	.078	.667	wing tail	.493 .880	.03 .03	1.11 1.66	0 0	1 1	1 1	.350 .350	Langley 9 in.

TABLE III.— SUMMARY OF GEOMETRIC AND AERODYNAMIC CHARACTERISTICS AND TEST CONDITIONS FOR WING-BODY-TAIL COMBINATIONS - Concluded  
(b) Aerodynamic characteristics

No.	$K_H$	$K_B(W)$	$K_W(B)$	$K_B(T)$	$K_T(B)$	Theoretical													Experimental		
						<sup>1</sup> Lift					Center of pressure								<sup>1</sup> Lift	c.p.	
						$(\beta C_{L\alpha})_W$	$(\beta C_{L\alpha})_T$	$(\beta C_{L\alpha})_B$	$\frac{2}{\beta}(\beta C_{L\alpha})_C$	$(\beta C_{L\alpha})_C$	$\frac{\bar{I}_N}{l}$	$\frac{\bar{I}_B(W)\alpha}{l}$	$\frac{\bar{I}_W(B)\alpha}{l}$	$\frac{\bar{I}_B(T)\alpha}{l}$	$\frac{\bar{I}_T(B)\alpha}{l}$	$\frac{\bar{I}_{Ca}}{l}$	$\frac{\bar{I}_{Ca}}{l}$	$(\beta C_{L\alpha})_B$	$(\beta C_{L\alpha})_O$	$\frac{\bar{I}_{Ca}}{l}$	
101	.17	.23	1.16	.12	1.27	4.00	4.00	.68	7.99	7.20	.154	.558	.500	.951	.951	.573	.535	---	7.74	.550	
102a	.08	.24	1.14	.24	1.14	3.47	3.48	.27	6.45	5.56	.229	.480	.485	.915	.918	.557	.521	---	5.20	.505	
b	.07	.24	1.14	.24	1.14	3.16	3.16	.23	5.71	5.16	.229	.480	.485	.915	.918	.557	.519	---	4.85	.500	
c	.07	.24	1.14	.24	1.14	2.83	2.83	.19	4.70	4.21	.229	.478	.485	.915	.918	.565	.525	---	4.25	.493	
d	.06	.24	1.14	.24	1.14	2.51	2.51	.16	4.50	4.02	.229	.477	.485	.914	.918	.558	.515	---	3.87	.489	
e	.06	.24	1.14	.24	1.14	2.02	2.02	.12	3.60	3.17	.229	.474	.485	.912	.918	.559	.510	---	3.11	.483	
103a	.96	.74	1.42	.32	1.19	1.32	1.32	.14	2.51	2.06	.104	.257	.261	.683	.701	.602	.581	---	1.97	.583	
b	.89	.62	1.42	.27	1.19	2.34	2.34	.23	4.17	3.40	.104	.281	.267	.714	.719	.627	.607	---	3.38	.603	
104	.08	.31	1.18	.62	1.36	2.93	1.50	.22	5.74	5.19	.182	.547	.475	.931	.864	.559	.508	---	5.00	.485	
105	<sup>3</sup> (.82)	.63	1.41	.26	1.41	2.94	3.12	2.01	12.77	8.70	<sup>3</sup> (.165)	.640	.574	.956	.948	.635	.488	2.41	8.39	<sup>4</sup> ---	
106	(.82)	.63	1.41	.06	1.29	2.94	3.64	2.01	12.87	11.73	(.118)	.655	.591	.982	.973	.647	.616	2.41	11.15	.599	
107	(.82)	.63	1.41	.14	1.34	2.94	3.67	1.99	13.81	10.31	(.118)	.655	.591	.964	.959	.662	.561	2.39	10.72	.555	
108	(1.15)	.69	1.46	.54	1.31	2.94	1.94	.49	4.98	4.26	(.118)	.431	.361	.868	.830	.666	.625	.59	<sup>4</sup> 3.90	<sup>4</sup> .595	
109	(3.48)	.70	1.54	.54	1.31	3.91	1.94	.49	4.54	4.16	(.118)	.505	.440	.868	.830	.718	.705	.59	3.77	.683	
110	(1.55)	.54	1.43	.54	1.31	3.91	1.94	.49	4.92	4.16	(.118)	.492	.432	.868	.830	.698	.675	.59	3.82	.663	
111	(.87)	.44	1.36	.54	1.31	3.91	1.94	.49	5.39	4.26	(.118)	.482	.431	.868	.830	.672	.629	.59	4.00	<sup>4</sup> .604	
112	(.07)	.12	1.11	.07	1.19	3.65	3.60	.23	5.73	5.45	(.036)	.546	.471	.968	.954	.548	.529	.23	5.24	.527	
113	(.07)	.12	1.11	.07	1.19	3.65	3.60	.23	5.73	5.45	(.036)	.632	.562	.968	.954	.615	.595	.23	5.31	.599	
114	(.07)	.12	1.11	.07	1.19	3.65	3.60	.23	5.73	5.45	(.036)	.719	.648	.968	.954	.682	.661	.23	5.36	.673	
115	(.48)	.53	1.30	.53	1.30	3.62	3.62	1.51	14.97	9.78	(.162)	.450	.390	.953	.914	.609	.446	1.72	9.09	<sup>4</sup> .486	
116	(.48)	.53	1.30	.53	1.30	3.62	3.62	1.51	14.97	9.78	(.162)	.617	.568	.953	.914	.686	.564	1.72	9.94	.970	
117	(.48)	.39	1.30	.53	1.30	3.62	3.62	1.51	14.53	10.73	(.162)	.461	.430	.953	.914	.628	.522	1.72	10.02	.515	
118	(.48)	.39	1.30	.53	1.30	3.62	3.62	1.51	14.53	10.73	(.162)	.628	.597	.953	.914	.698	.621	1.72	9.82	.615	
119	(.48)	.39	1.30	.20	1.30	3.62	3.62	1.51	13.29	9.49	(.162)	.461	.430	.953	.954	.613	.492	1.72	9.00	.486	
120	(.48)	.39	1.30	.20	1.30	3.62	3.62	1.51	13.29	9.49	(.162)	.628	.597	.953	.954	.690	.600	1.72	9.00	.580	
<sup>5</sup> 121	(.31)	.39	1.30	.53	1.30	2.79	2.79	.76	11.02	6.79	(.162)	.461	.403	.952	.927	.638	.457	.87	6.99	<sup>4</sup> ---	
<sup>5</sup> 122	(.31)	.39	1.30	.53	1.30	2.79	2.79	.76	11.02	6.79	(.162)	.628	.570	.952	.927	.714	.581	.87	7.05	.588	
<sup>5</sup> 123	(.26)	.53	1.30	.53	1.30	2.19	2.76	.50	7.96	4.67	(.162)	.411	.367	.952	.927	.604	.371	.58	4.55	.392	
<sup>5</sup> 124	(.26)	.53	1.30	.53	1.30	2.19	2.76	.50	7.96	4.67	(.162)	.578	.533	.952	.927	.689	.514	.58	4.48	<sup>4</sup> ---	

<sup>1</sup>All lift curve slopes (per radian) referred to exposed area of larger lifting surface except  $\beta C_{L\alpha W}$  or  $\beta C_{L\alpha T}$ .<sup>2</sup>Value by neglecting wing-tail interference.<sup>3</sup>( ) indicates experimental value used in theory for combination.<sup>4</sup>Experimental  $C_L$  or  $C_m$  curve nonlinear near  $\alpha = 0$ .<sup>5</sup>Alden-Schindler technique applied in estimating interference.

## CHARTS

The charts that follow present numerical values for the quantities necessary to obtain the lift and center-of-pressure positions of wing-body and wing-body-tail combinations by the method of this report. The charts are sufficiently accurate to estimate the lift of combinations within  $\pm 10$  percent and to determine the center of pressure of the combinations within  $\pm 0.02$  body length. A guide to the location of the parameters follows:

Parameter	Conditions	Chart
$K_{W(B)}$	$\lambda=1, \beta A > 2, M_\infty > 1$ -----	2
	other conditions-----	1
$K_{B(W)}$	$(\beta A)(1+\lambda)\left(\frac{1}{m\beta}+1\right) \geq 4$ , afterbody---	4 (a)
	$(\beta A)(1+\lambda)\left(\frac{1}{m\beta}+1\right) \geq 4$ , no afterbody--	4 (b)
	$(\beta A)(1+\lambda)\left(\frac{1}{m\beta}+1\right) \leq 4$ -----	1
$k_{W(B)}$	$\lambda=1, \beta A > 2, M_\infty > 1$ -----	3
	other conditions-----	1

Parameter	Conditions	Chart
$k_{B(W)}$	-----	1
$\frac{f_W - r_W}{s_W - r_W}$	$M_\infty < 1$ -----	5
$\frac{f_W - r_W}{s_W - r_W}$	$M_\infty > 1$ -----	6
$i$	(for $\lambda=1$ , see Appendix C)-----	7
$\beta C_{L_{aW}}$	$M_\infty > 1$ -----	8
$\bar{l}_N/l_S$	slender ogival nose-----	9
$(\bar{x}/c_r)_W$	$M_\infty > 1$ -----	10
	$M_\infty < 1$ -----	11
$(\bar{x}/c_r)_{W(B)\alpha}$	$\lambda=0, \Lambda_{TE}=0$ -----	13
	other conditions use $(\bar{x}/c_r)_W$	
$(\bar{x}/c_r)_{W(B)\delta}$	$\lambda=0, \Lambda_{TE}=0$ -----	13
	$\lambda=1, M_\infty > 1$ -----	12
	other conditions use $(\bar{x}/c_r)_W$	
$(\bar{x}/c_r)_{B(W)\alpha}$	$M_\infty > 1, (\beta A)(1+\lambda)\left(1+\frac{1}{m\beta}\right) \geq 4$ -----	14
or		
$(\bar{x}/c_r)_{B(W)\delta}$	$M_\infty > 1$ , low aspect ratio-----	15
	$M_\infty < 1$ -----	16

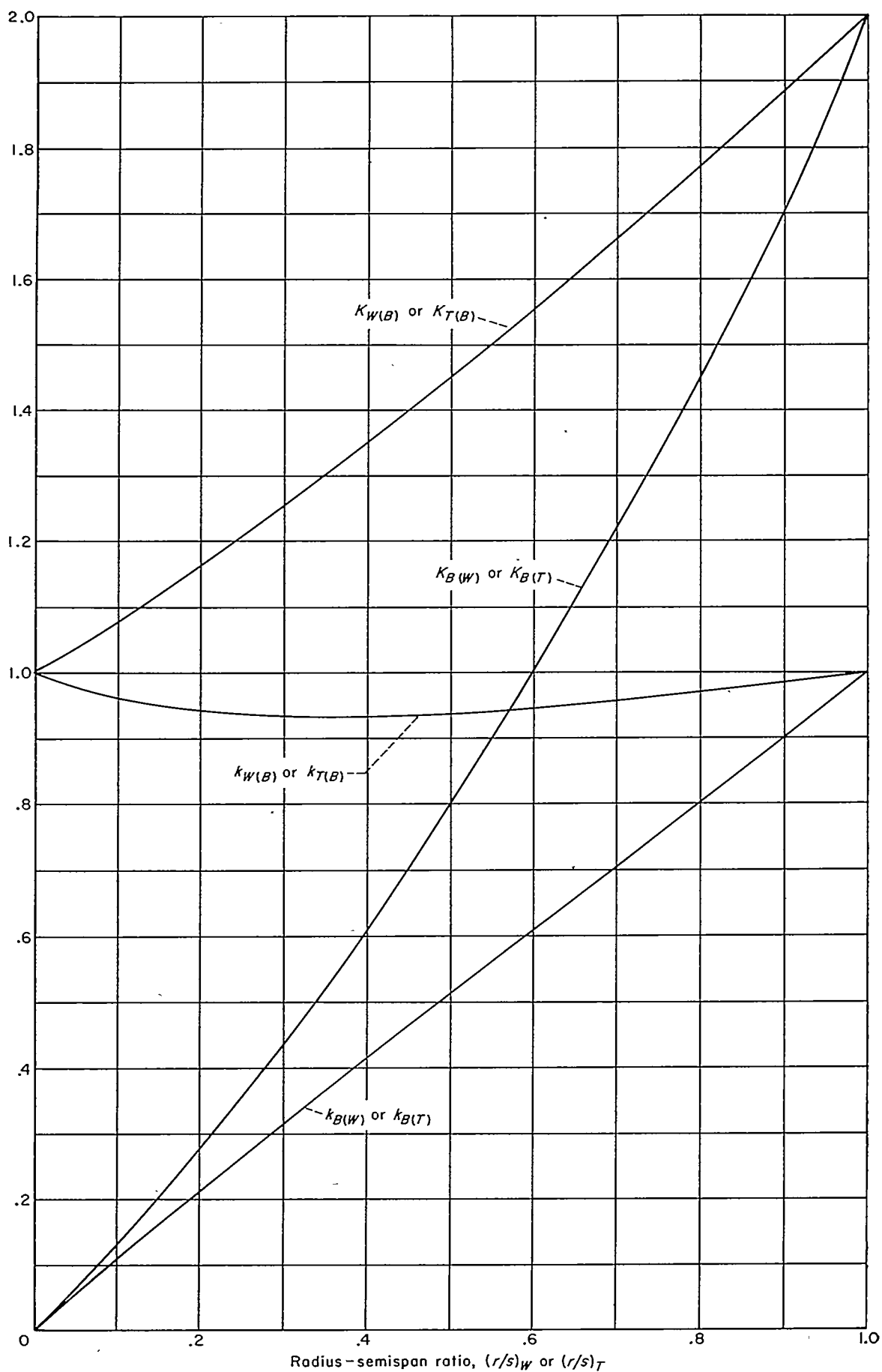


CHART 1.—Values of lift ratios based on slender-body theory.



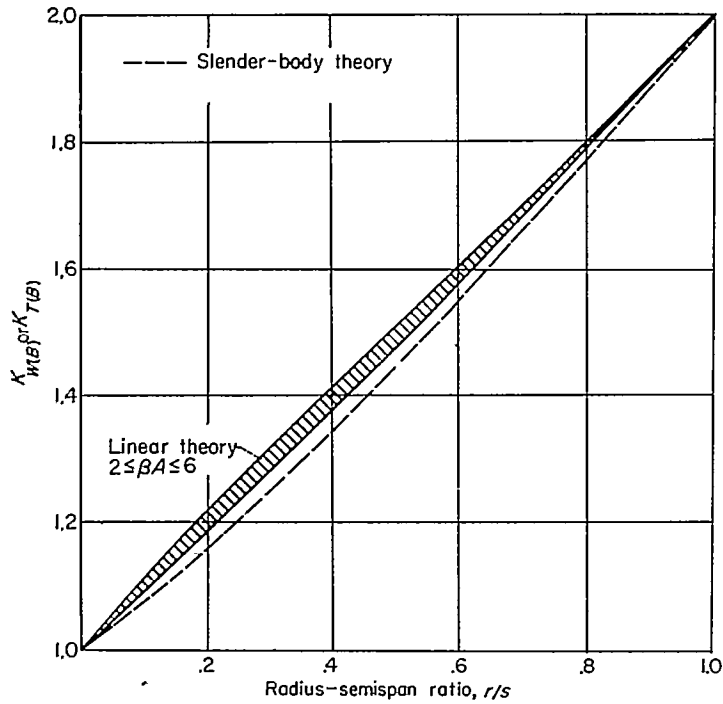


CHART 2.—Values of  $K_{W(B)}$  or  $K_{T(B)}$  for rectangular wing and body combinations.

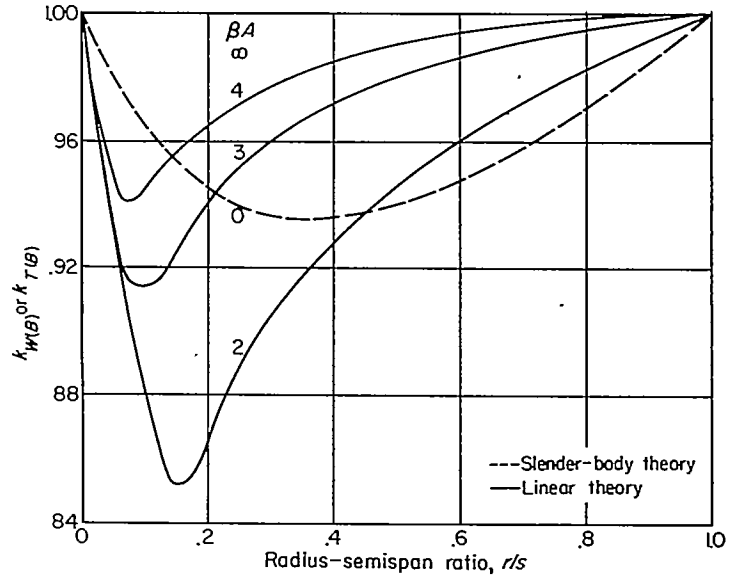
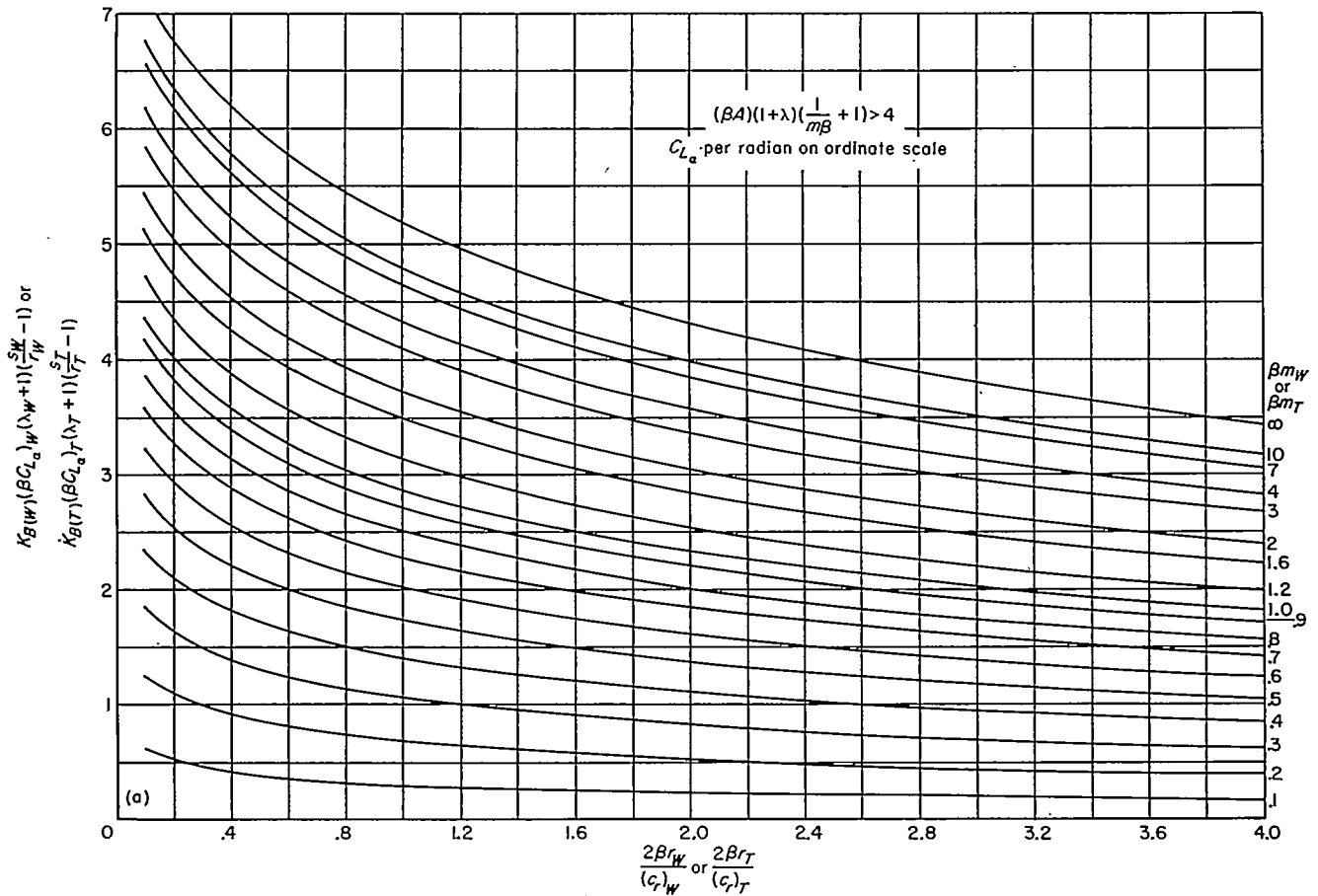
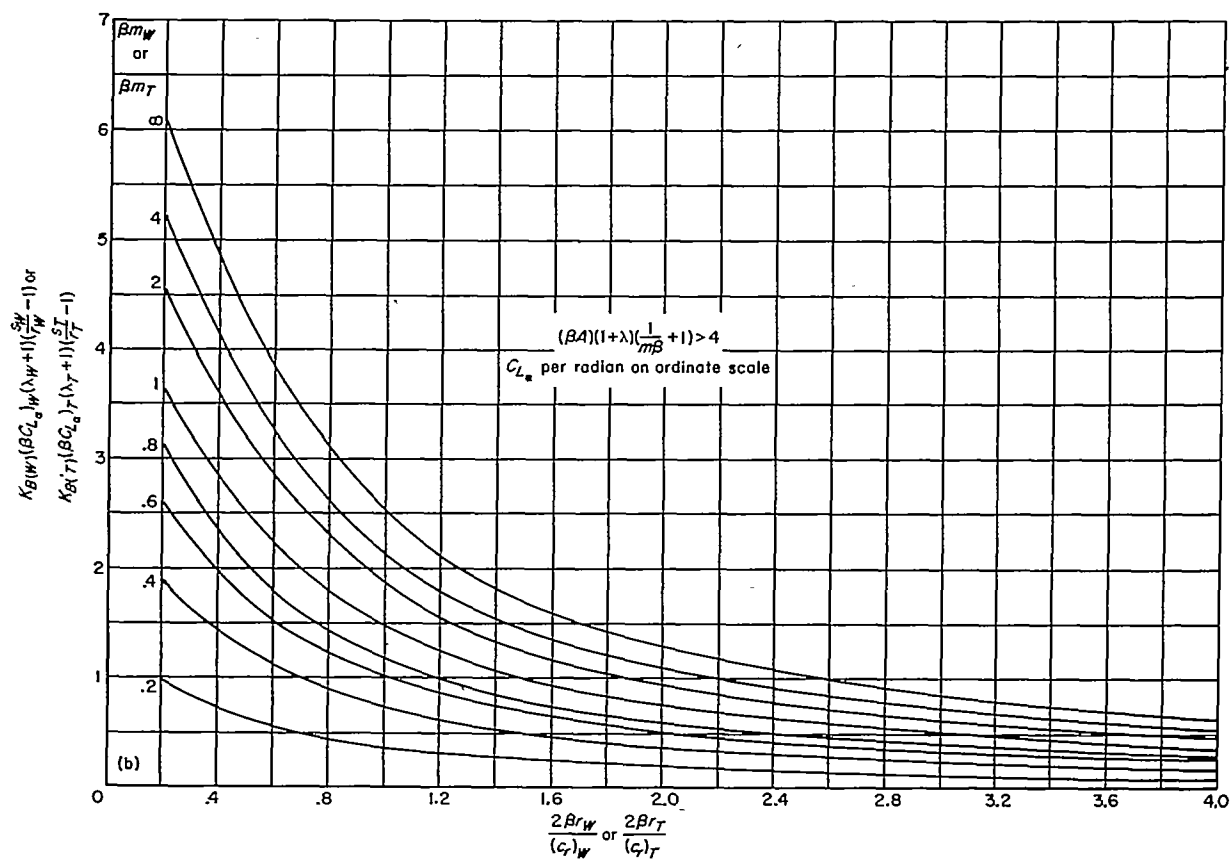


CHART 3.—Values of  $k_{W(B)}$  or  $k_{T(B)}$  for rectangular wing and body combinations.



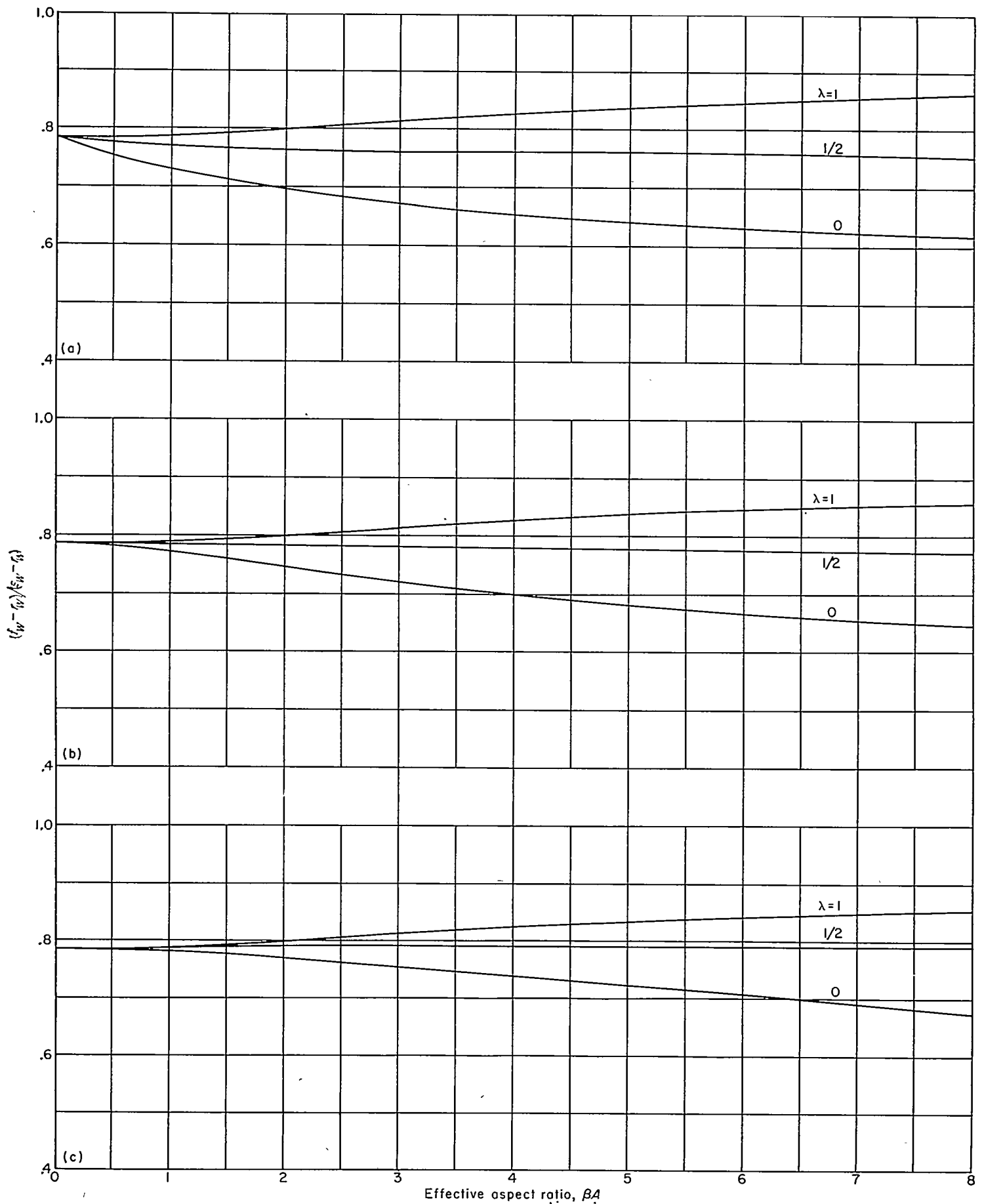
(a) Afterbody.

CHART 4.—Design charts for determining  $K_{B(W)}$  and  $K_{B(T)}$  for high-aspect-ratio range at supersonic speeds.



(b) No afterbody.

CHART 4.—Concluded.

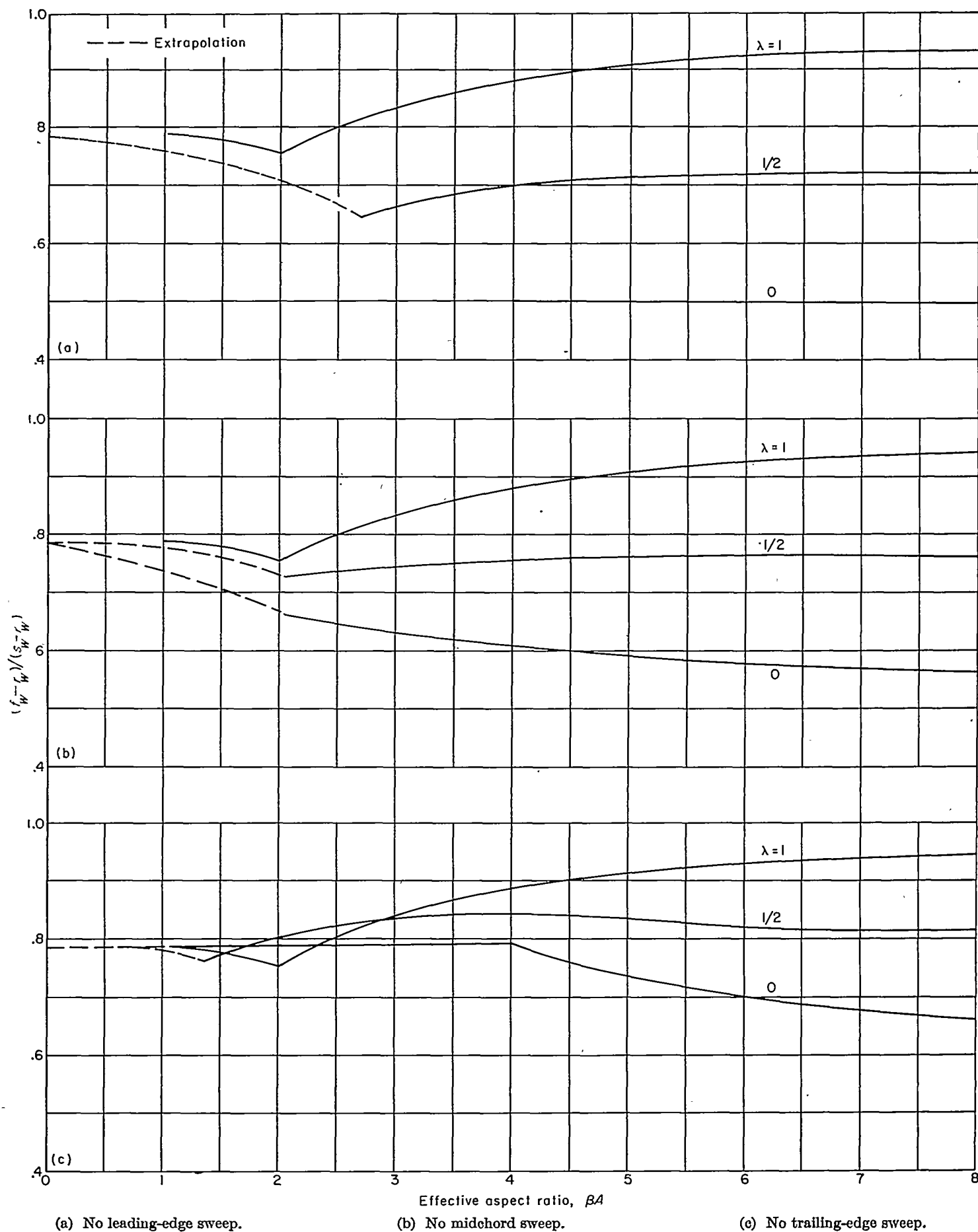


(a) No leading-edge sweep.

(b) No midchord sweep.

(c) No trailing-edge sweep.

CHART 5.—Chart for determination of wing vortex lateral positions at subsonic speeds.



(a) No leading-edge sweep.

(b) No midchord sweep.

(c) No trailing-edge sweep.

CHART 6.—Chart for determination of wing vortex lateral positions at supersonic speeds.

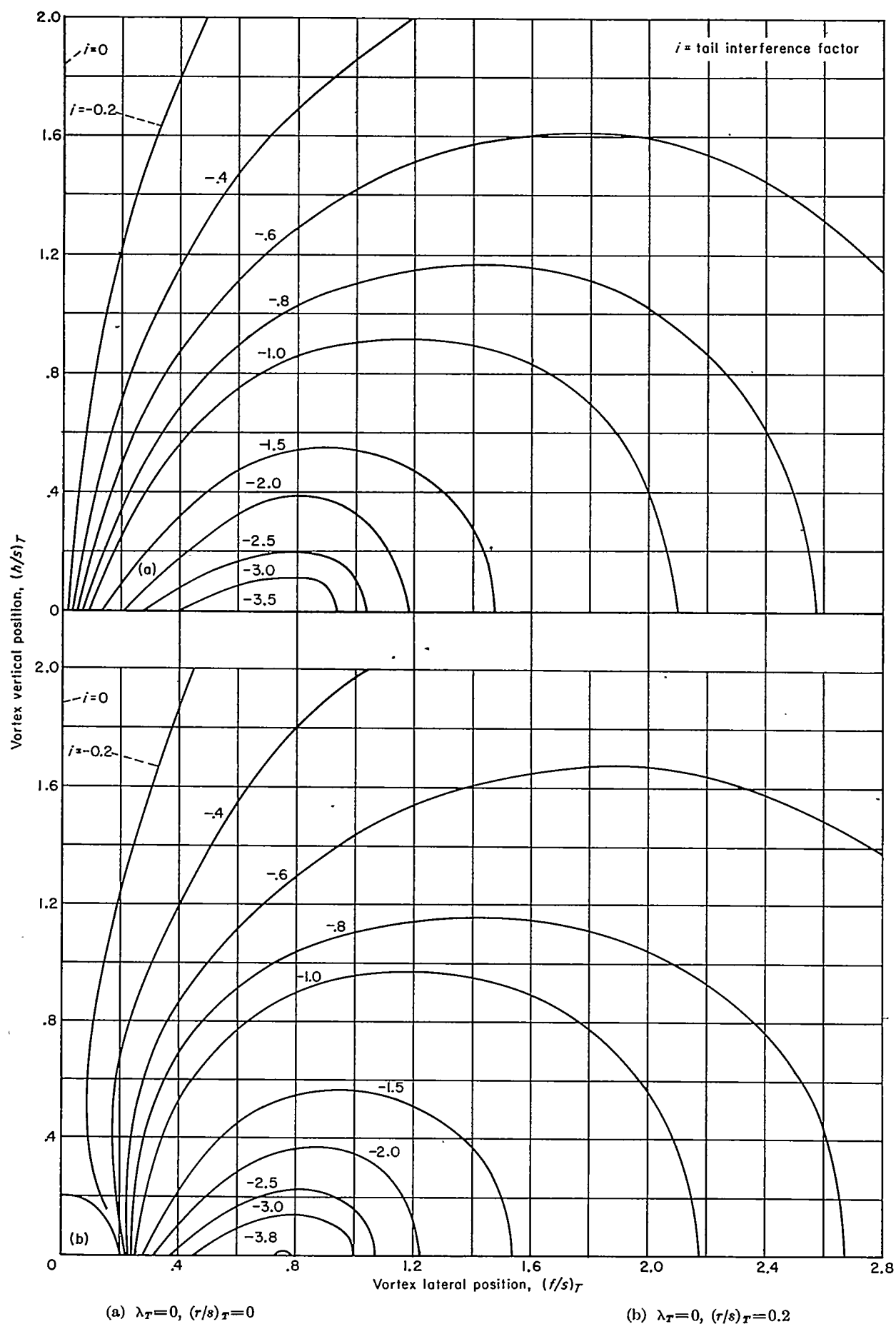
(a)  $\lambda_T = 0$ ,  $(r/s)_T = 0$ (b)  $\lambda_T = 0$ ,  $(r/s)_T = 0.2$ 

CHART 7.—Charts for determination of tail interference factor as determined by strip theory.

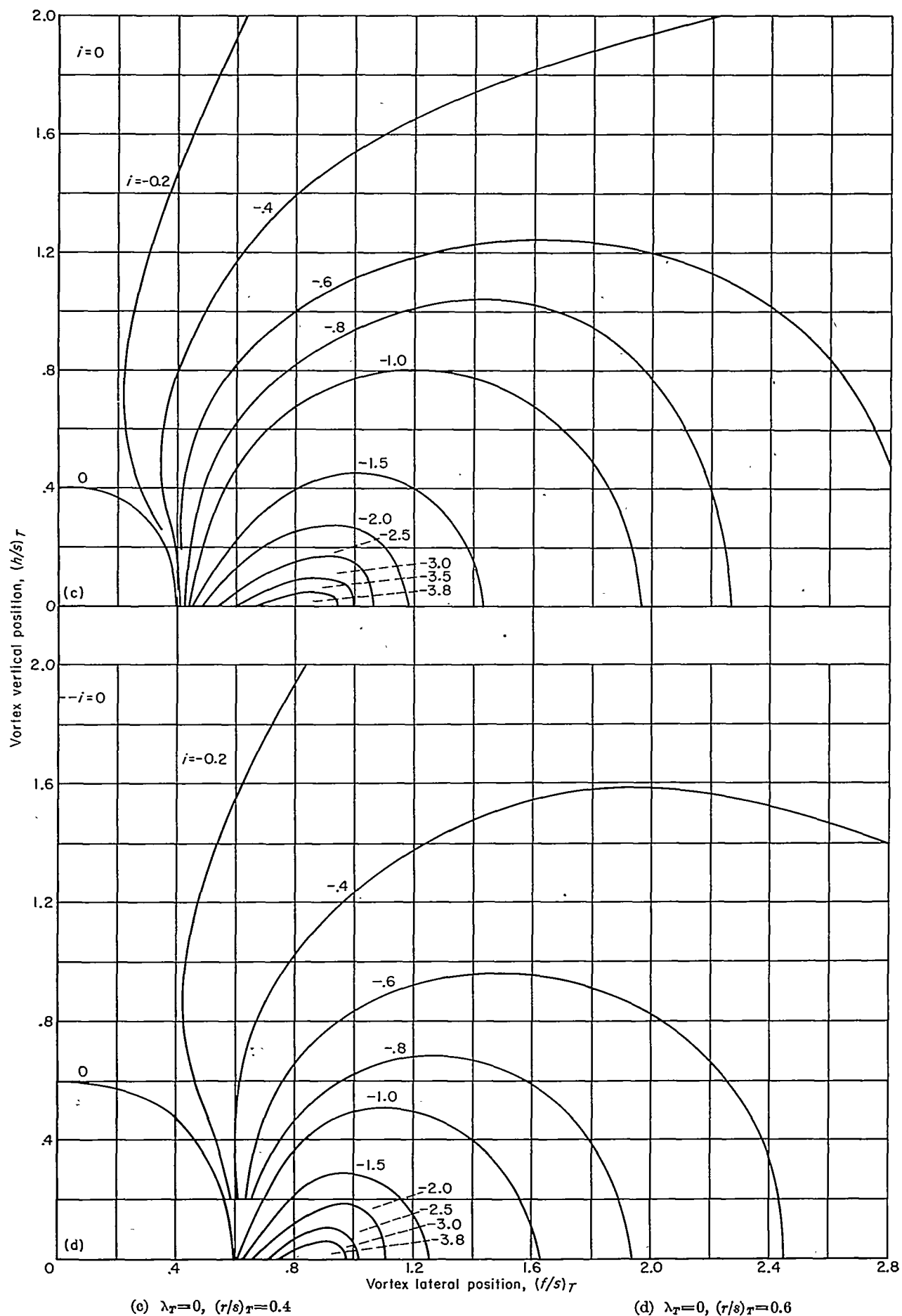


CHART 7.—Continued.

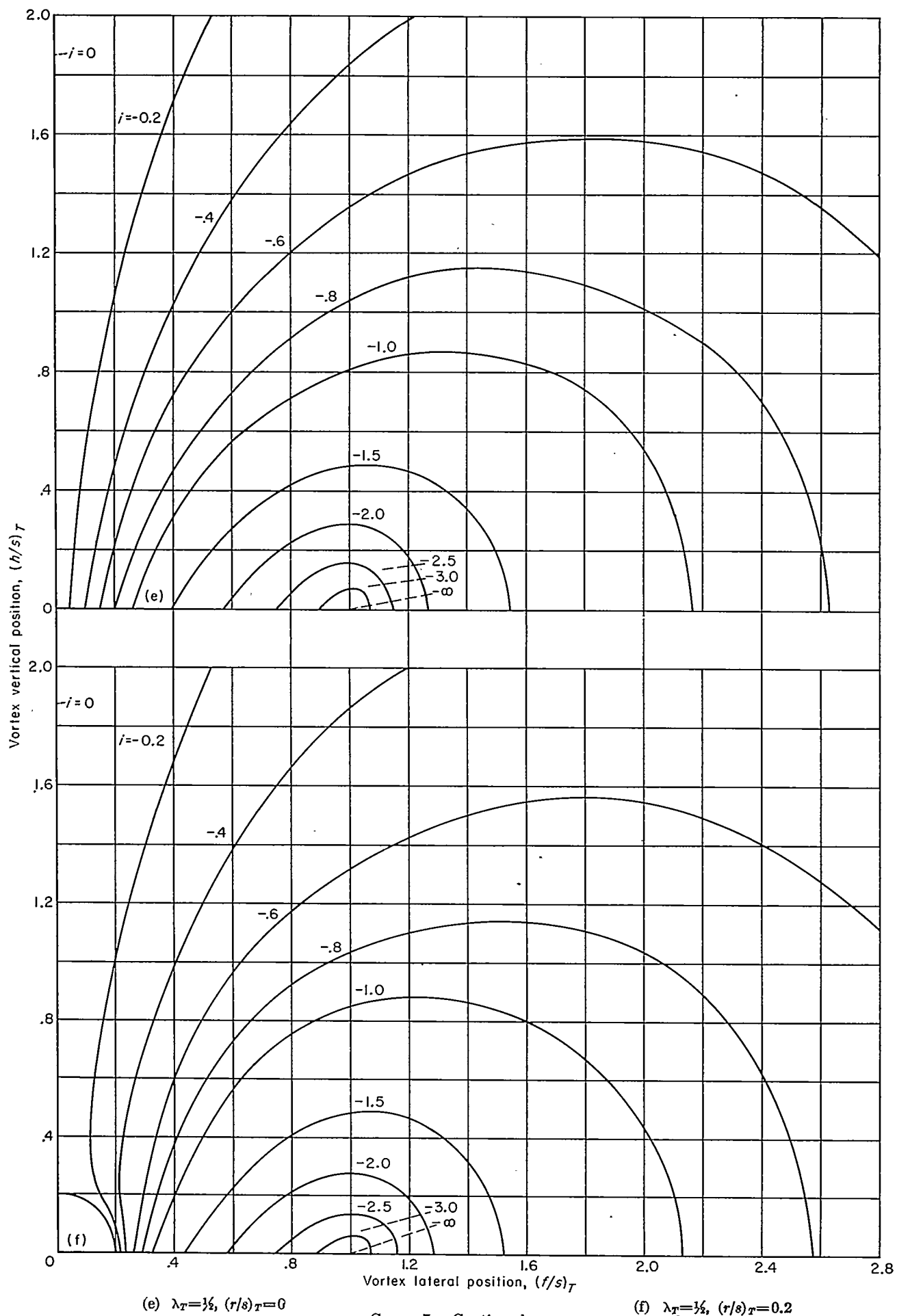
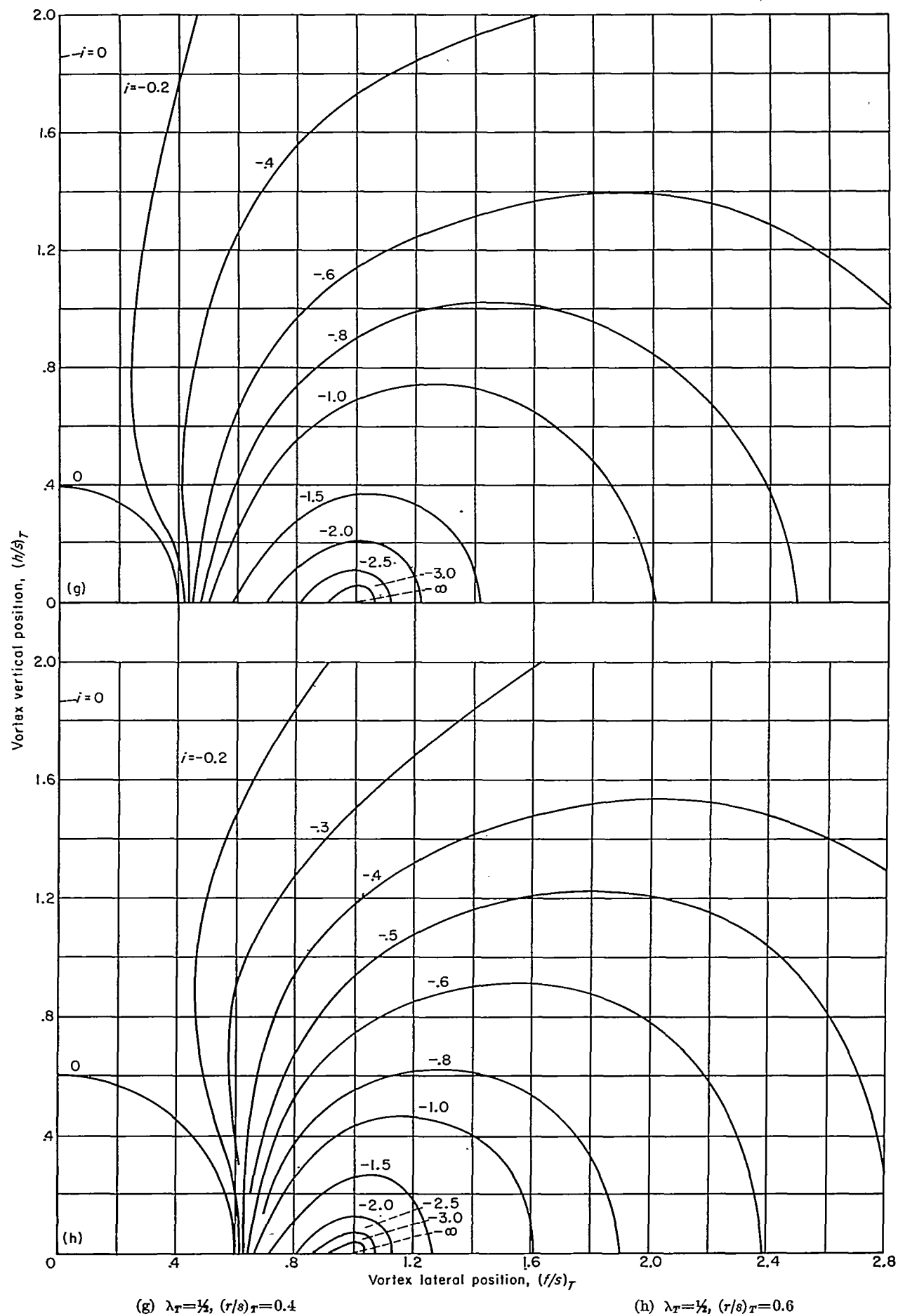


CHART 7.—Continued.

(g)  $\lambda_T = \frac{1}{2}$ ,  $(r/s)_T = 0.4$ (h)  $\lambda_T = \frac{1}{2}$ ,  $(r/s)_T = 0.6$



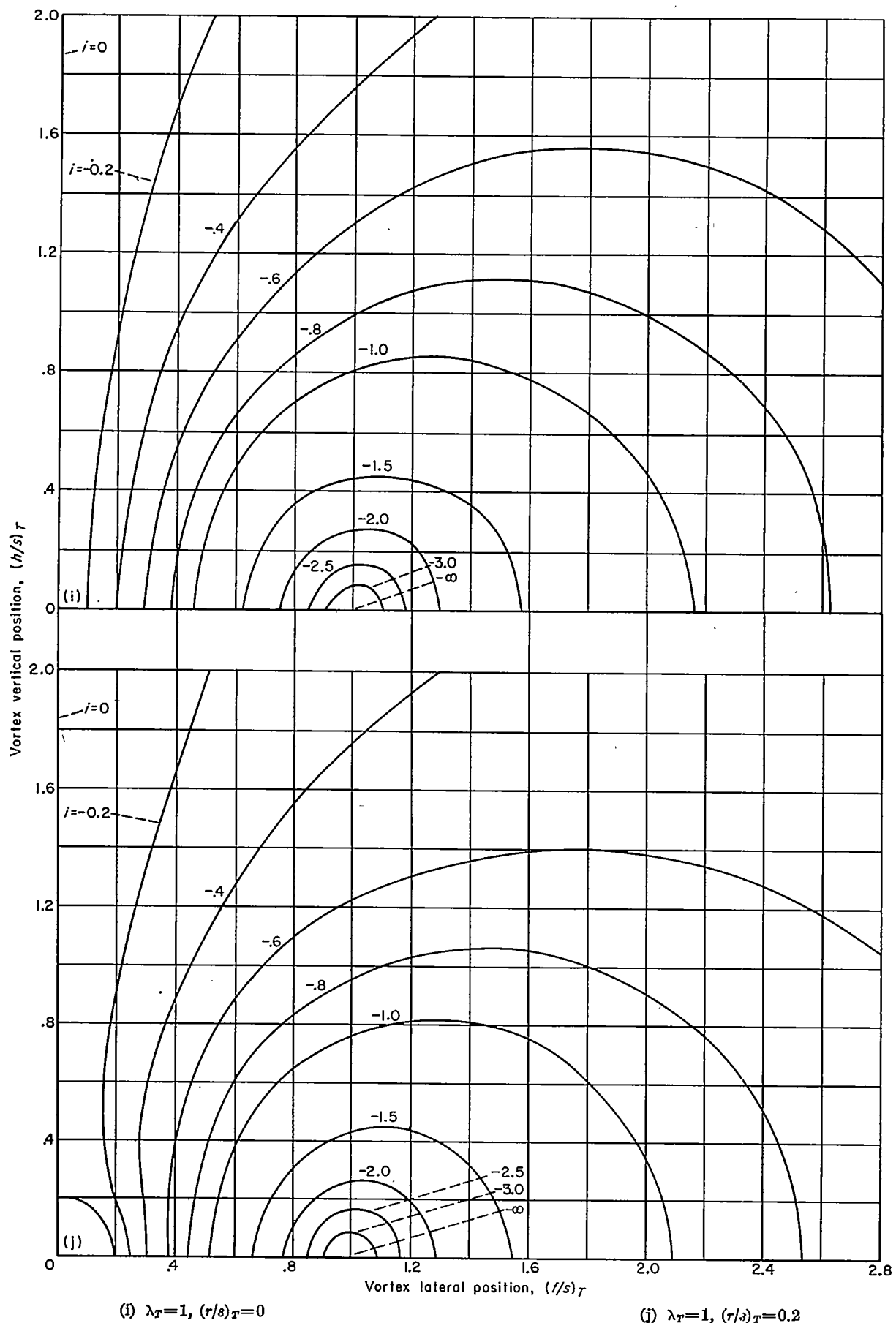
(i)  $\lambda_T=1, (r/s)_T=0$ (j)  $\lambda_T=1, (r/s)_T=0.2$ 

CHART 7.—Continued.

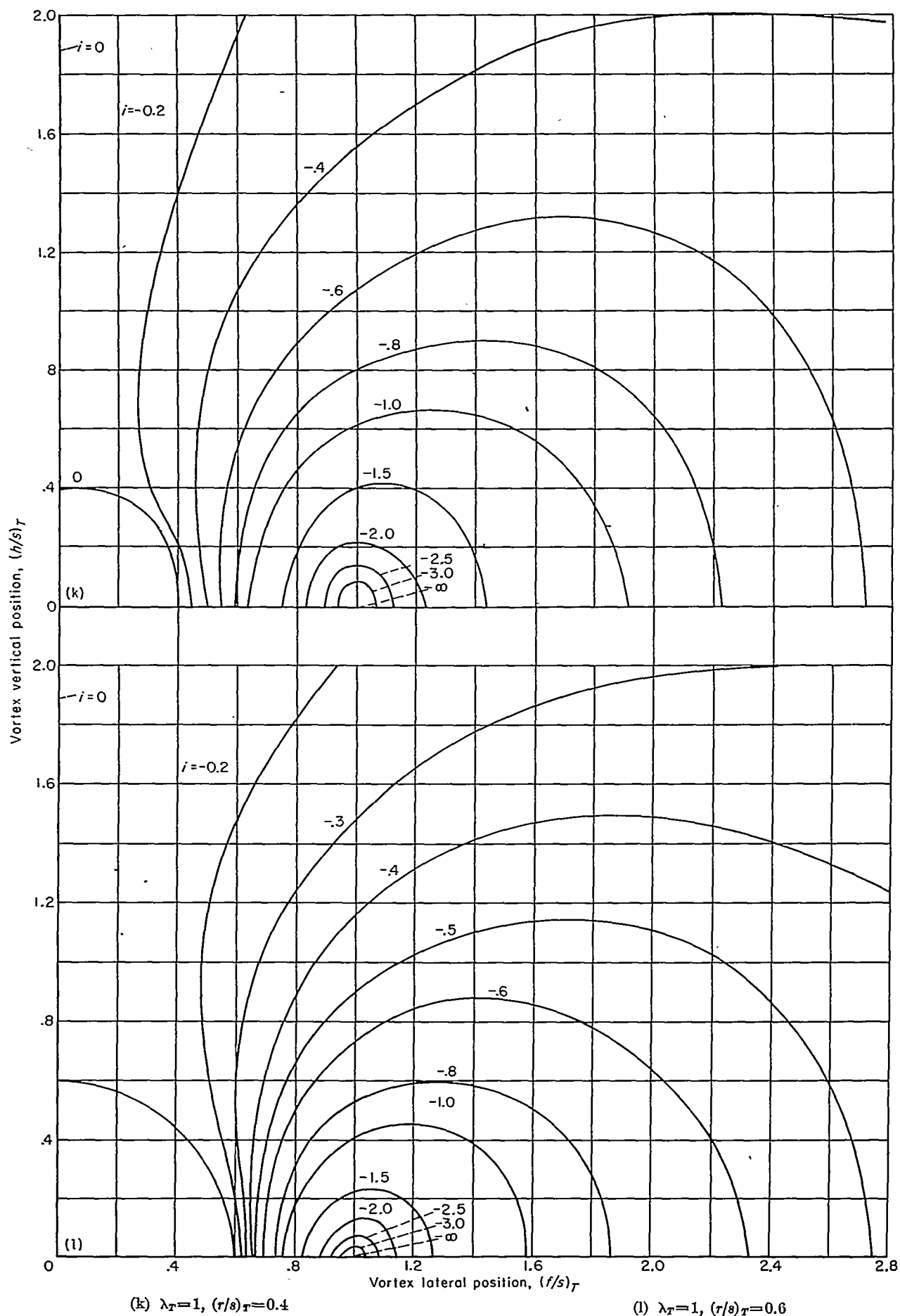


CHART 7.—Concluded.

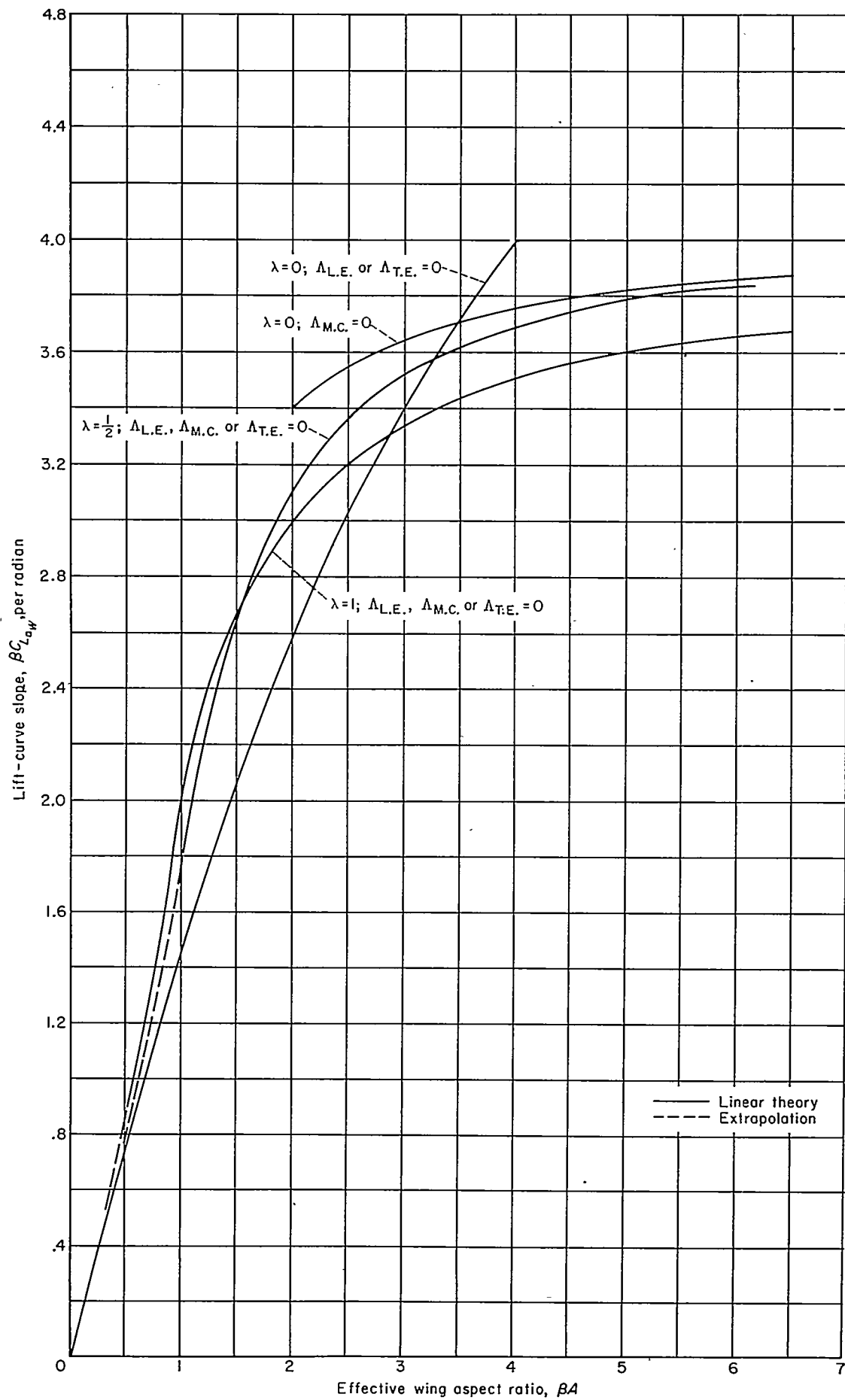


CHART 8.—Lift-curve slopes of wings as determined by linear theory for supersonic speeds.

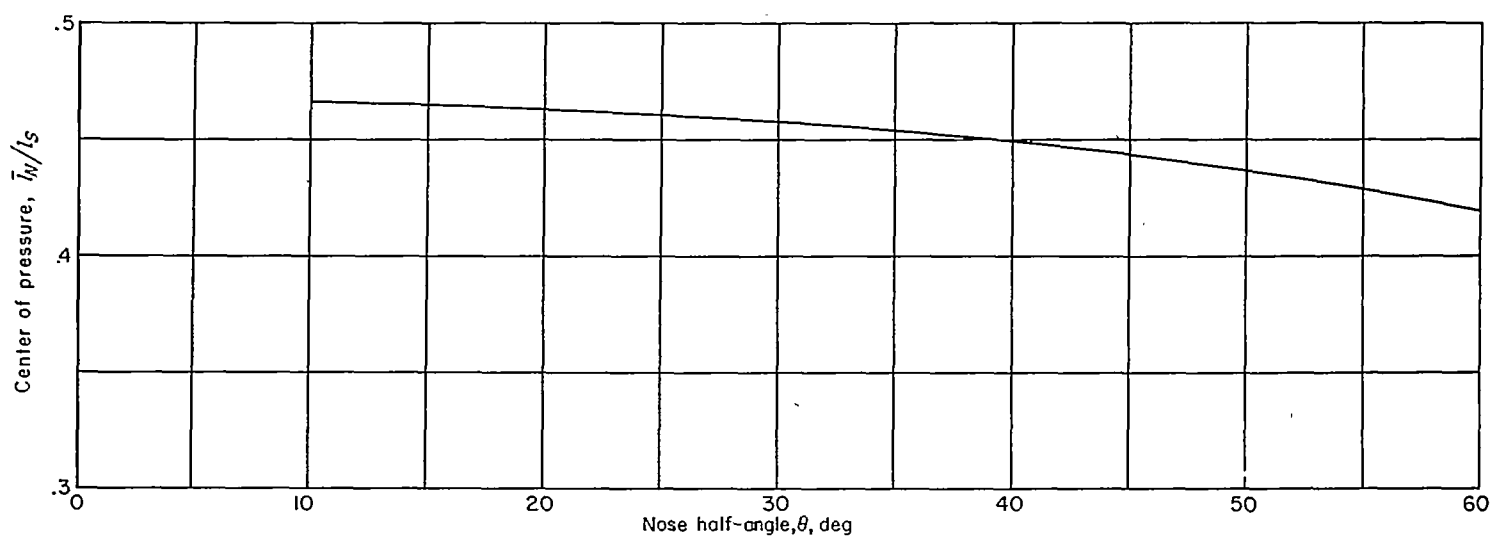
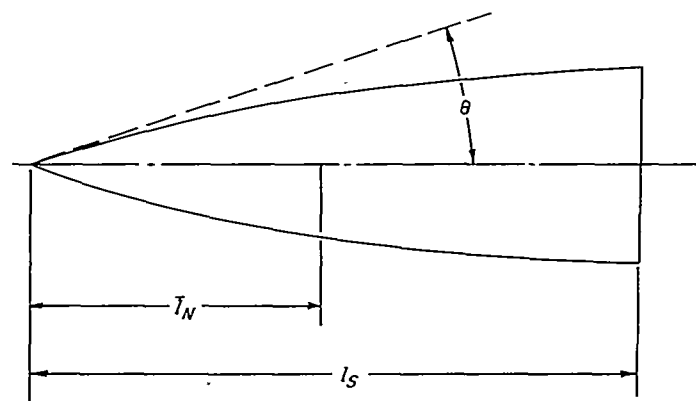
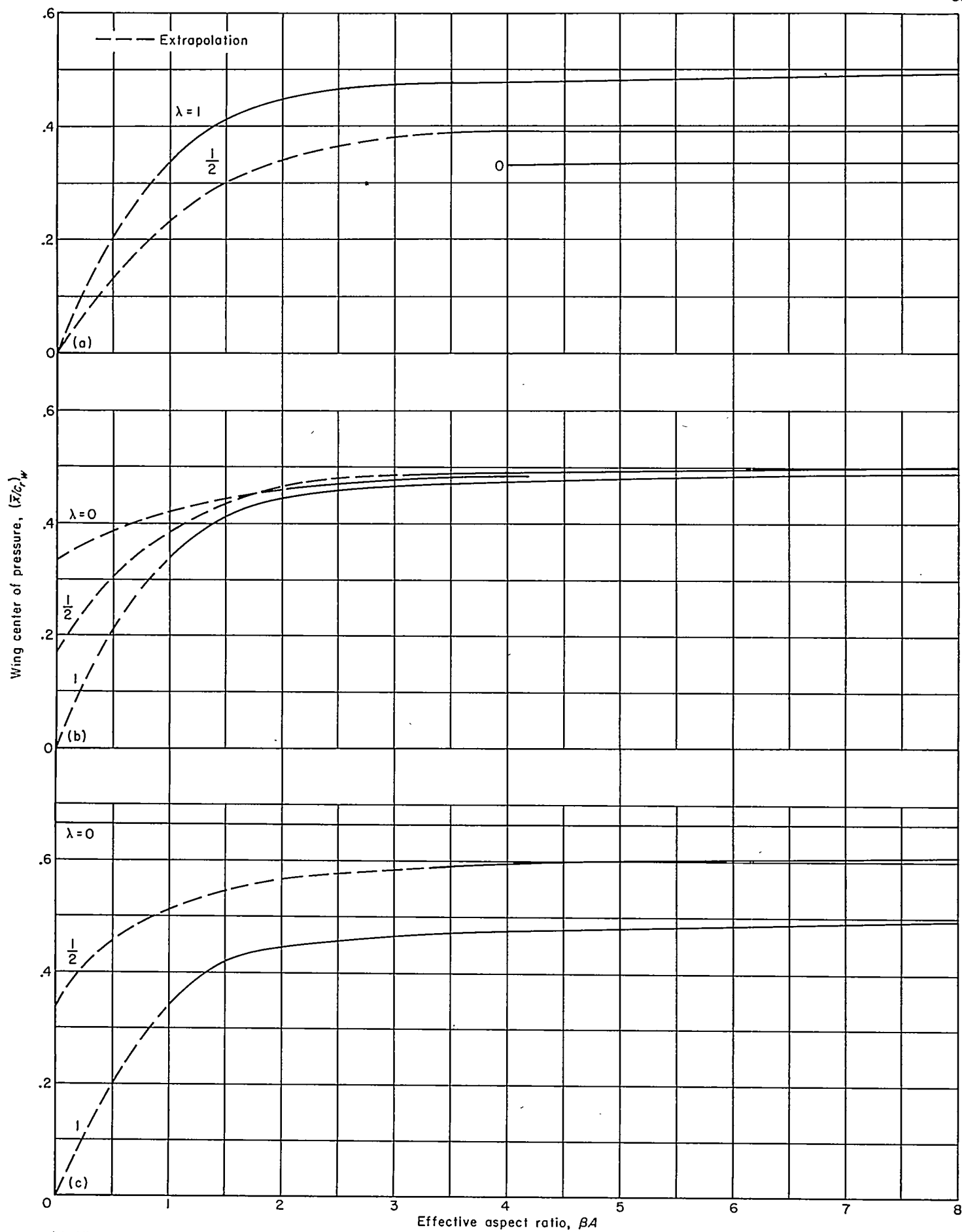


CHART 9.—Center of pressure of ogival nose as determined from slender-body theory.

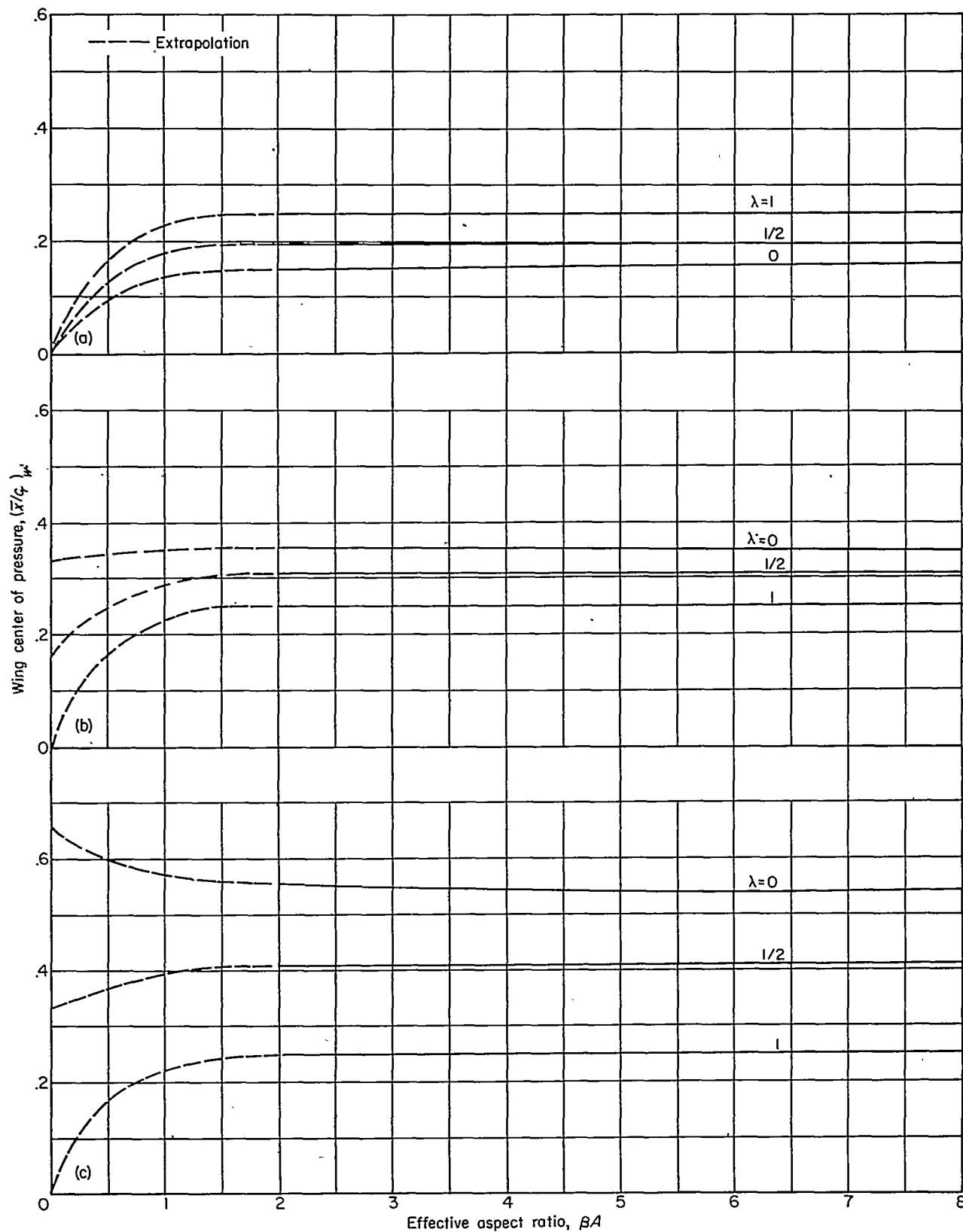


(a) No leading-edge sweep.

(b) No midchord sweep.

(c) No trailing-edge sweep.

CHART 10.—Charts for wing-alone center of pressure at supersonic speeds as determined by linear theory.



(a) No leading-edge sweep.

(b) No midchord sweep.

(c) No trailing-edge sweep.

CHART 11.—Charts for wing-alone center of pressure at subsonic speeds as determined by lifting-line theory.

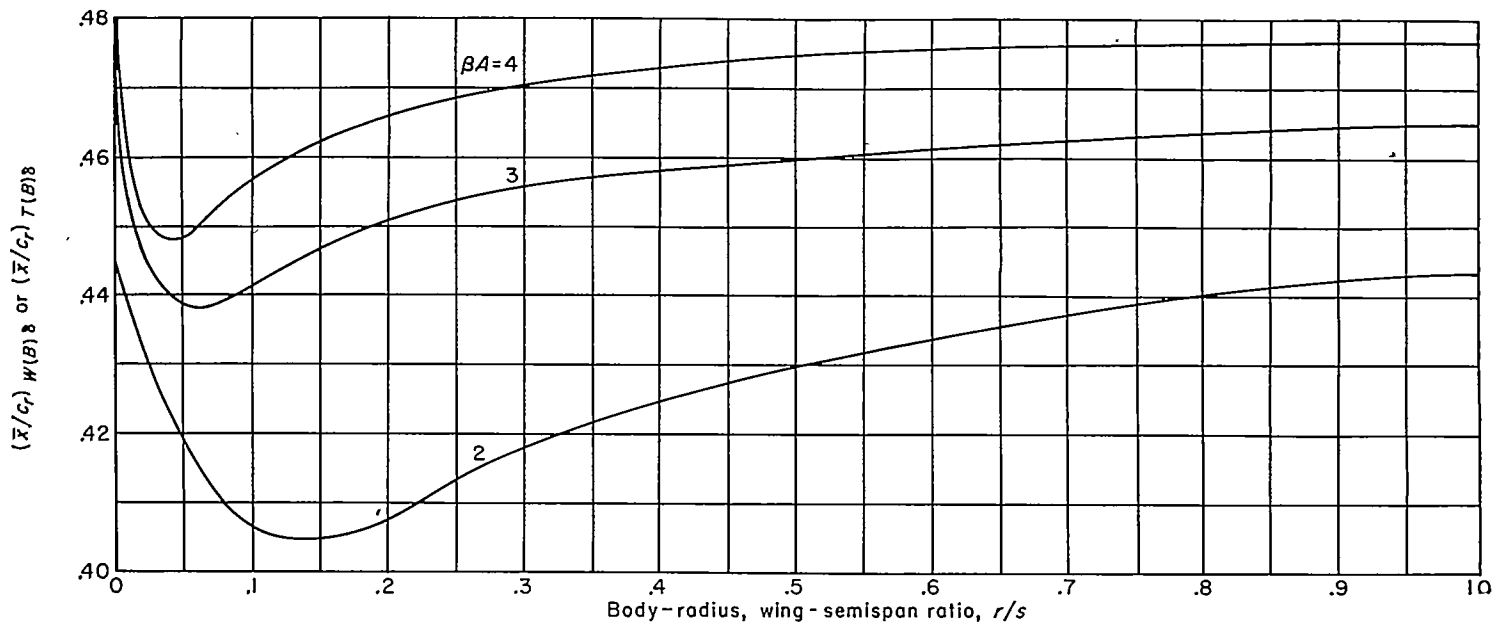


CHART 12.—Values of  $(\bar{x}/c_r)_{W(B)}$  or  $(\bar{x}/c_r)_{T(B)}$  from linear theory for rectangular wing (or tail) and body combinations at supersonic speeds.

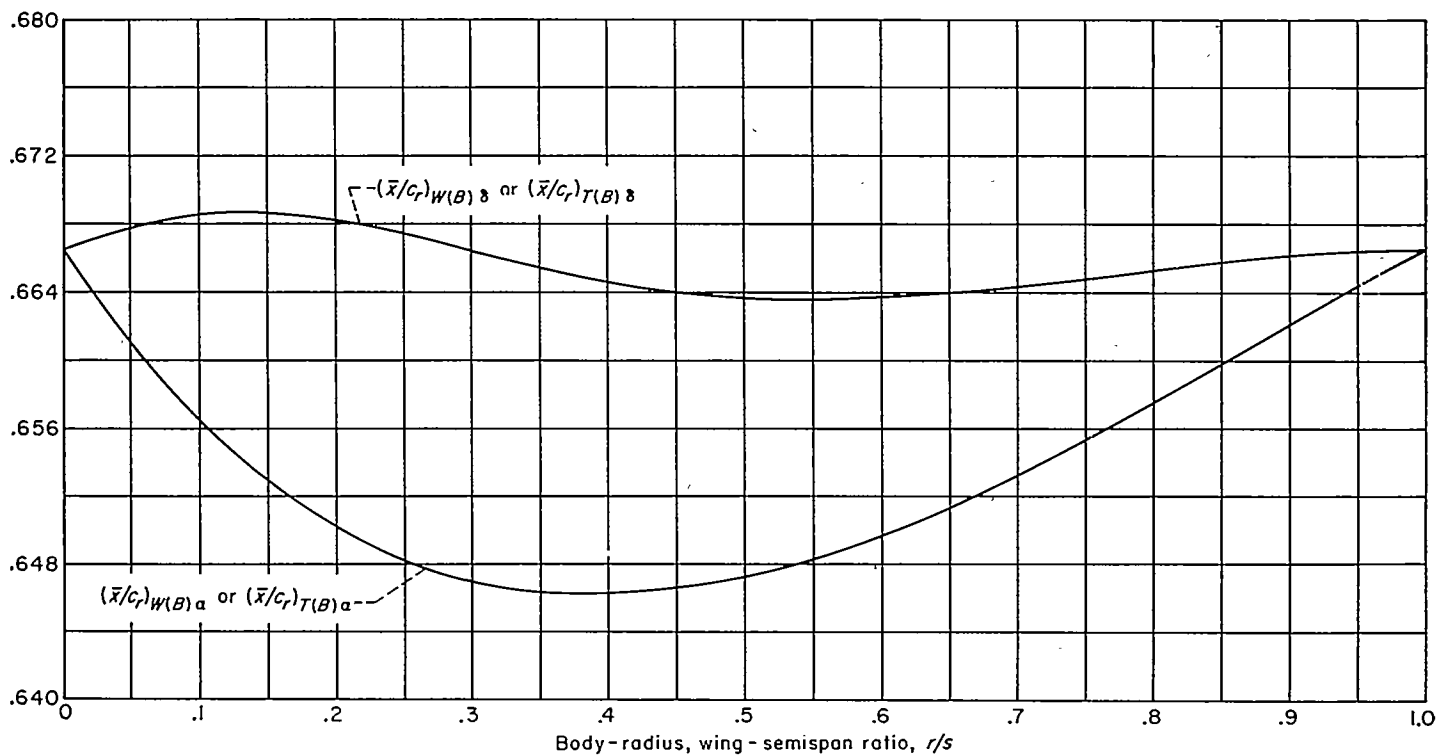


CHART 13.—Center of pressure of lift acting on triangular wing (or tail) panel in combination with a body, from slender-body theory ( $\Delta_{TF} = 0$ ).

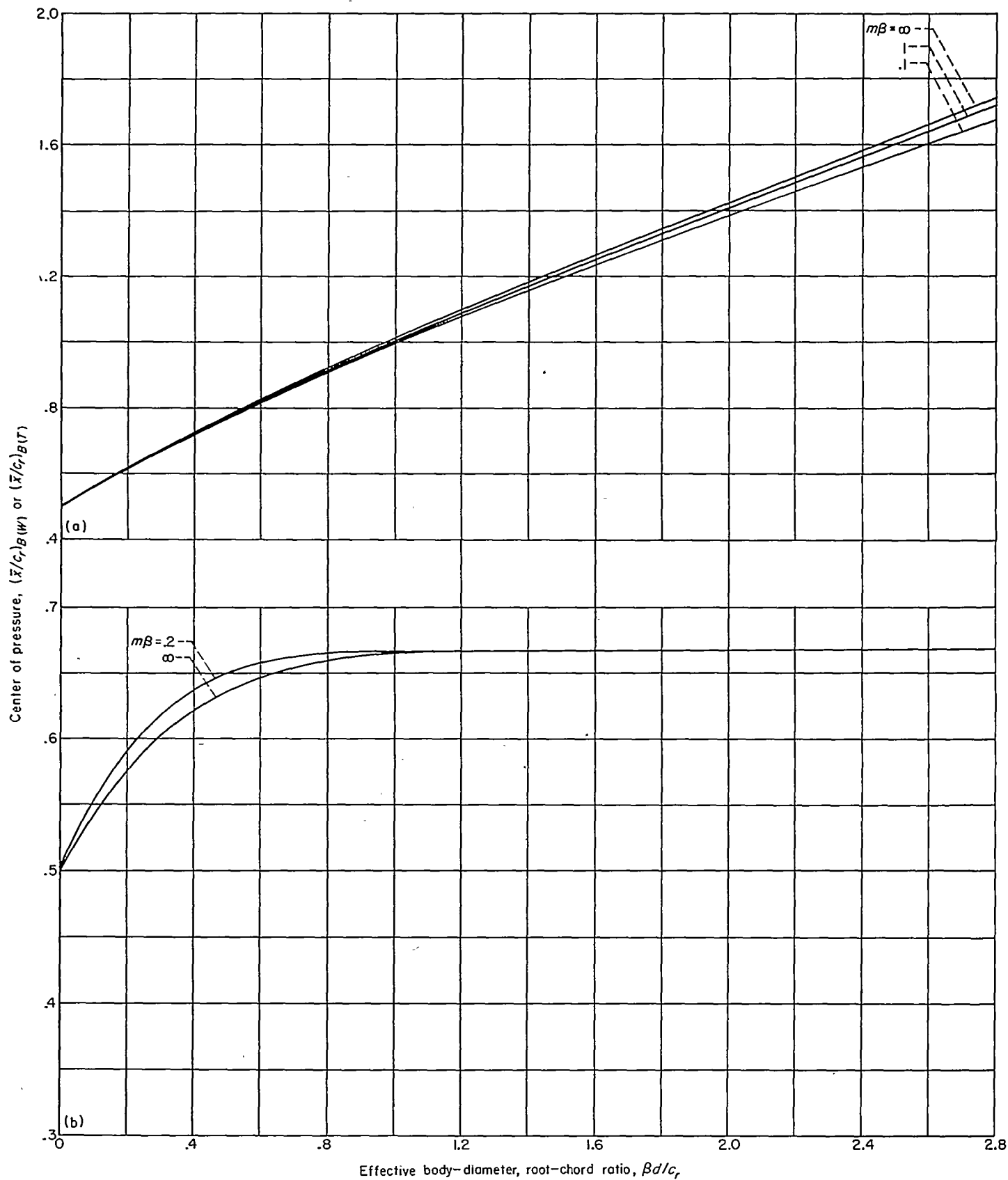
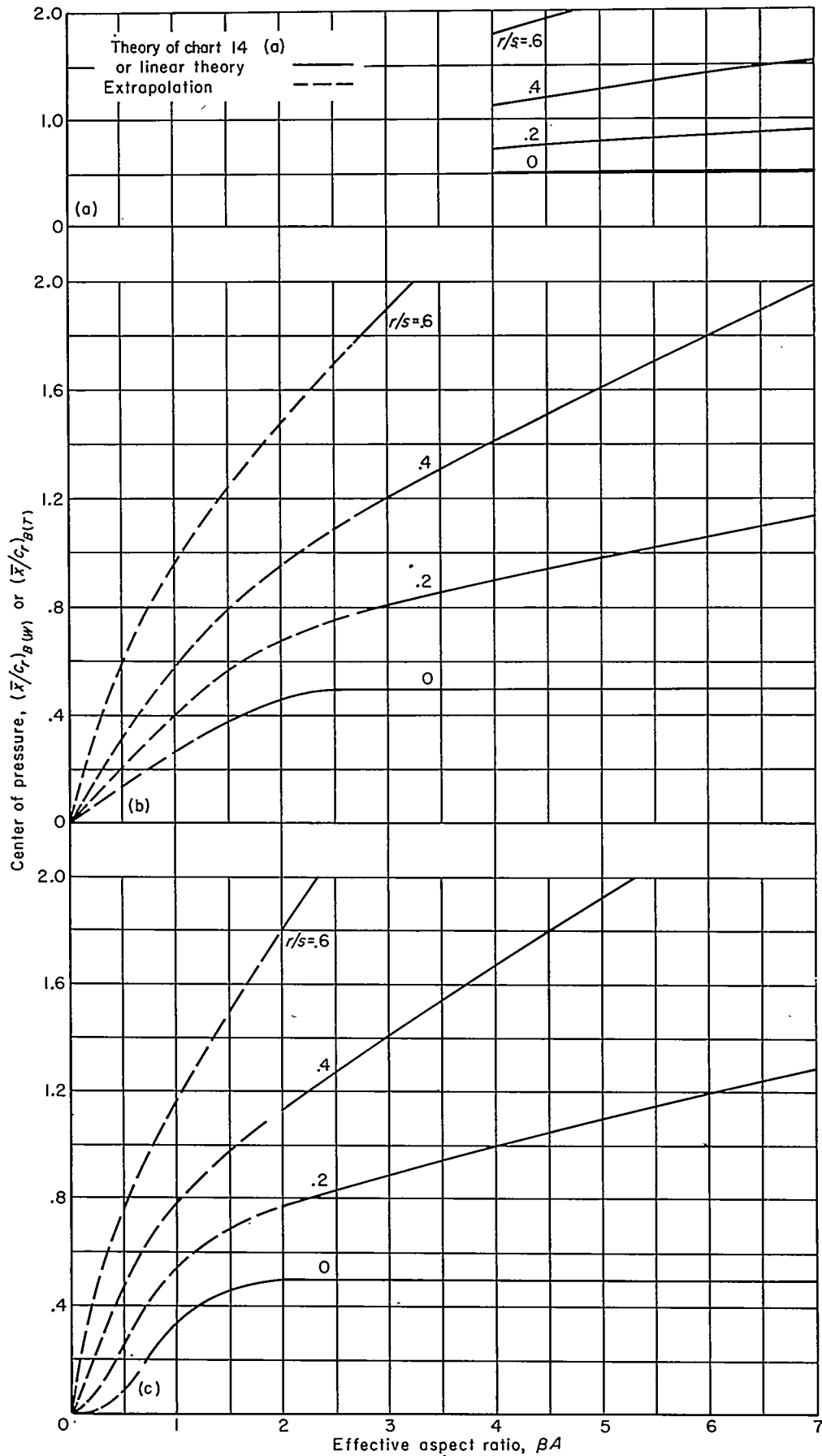


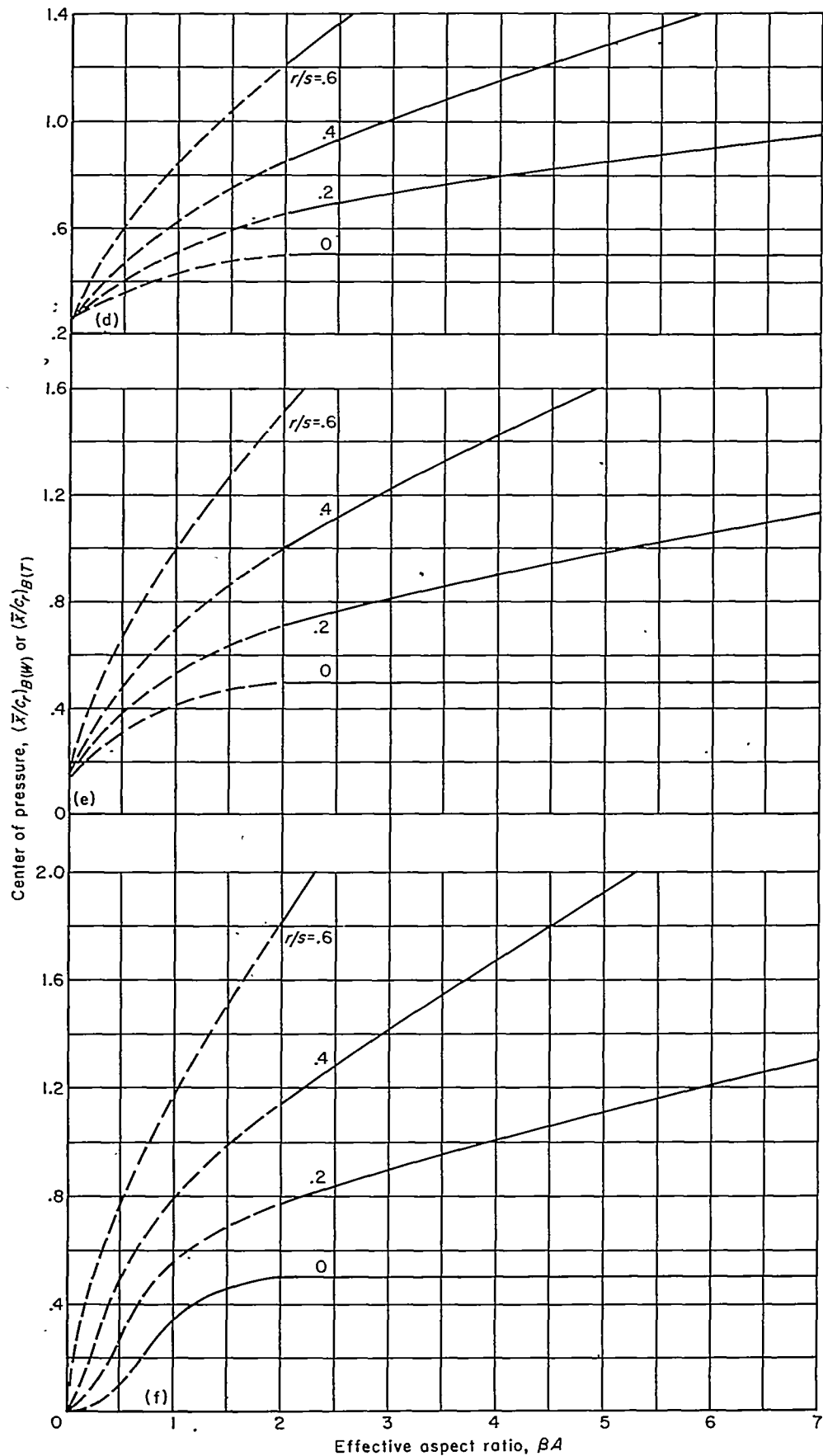
CHART 14.—Charts for determination of  $(\bar{x}/c_r)_{B(W)}$  or  $(\bar{x}/c_r)_{B(T)}$  at supersonic speeds when  $\beta A(1+\lambda)\left(1+\frac{1}{m\beta}\right) > 4$ .





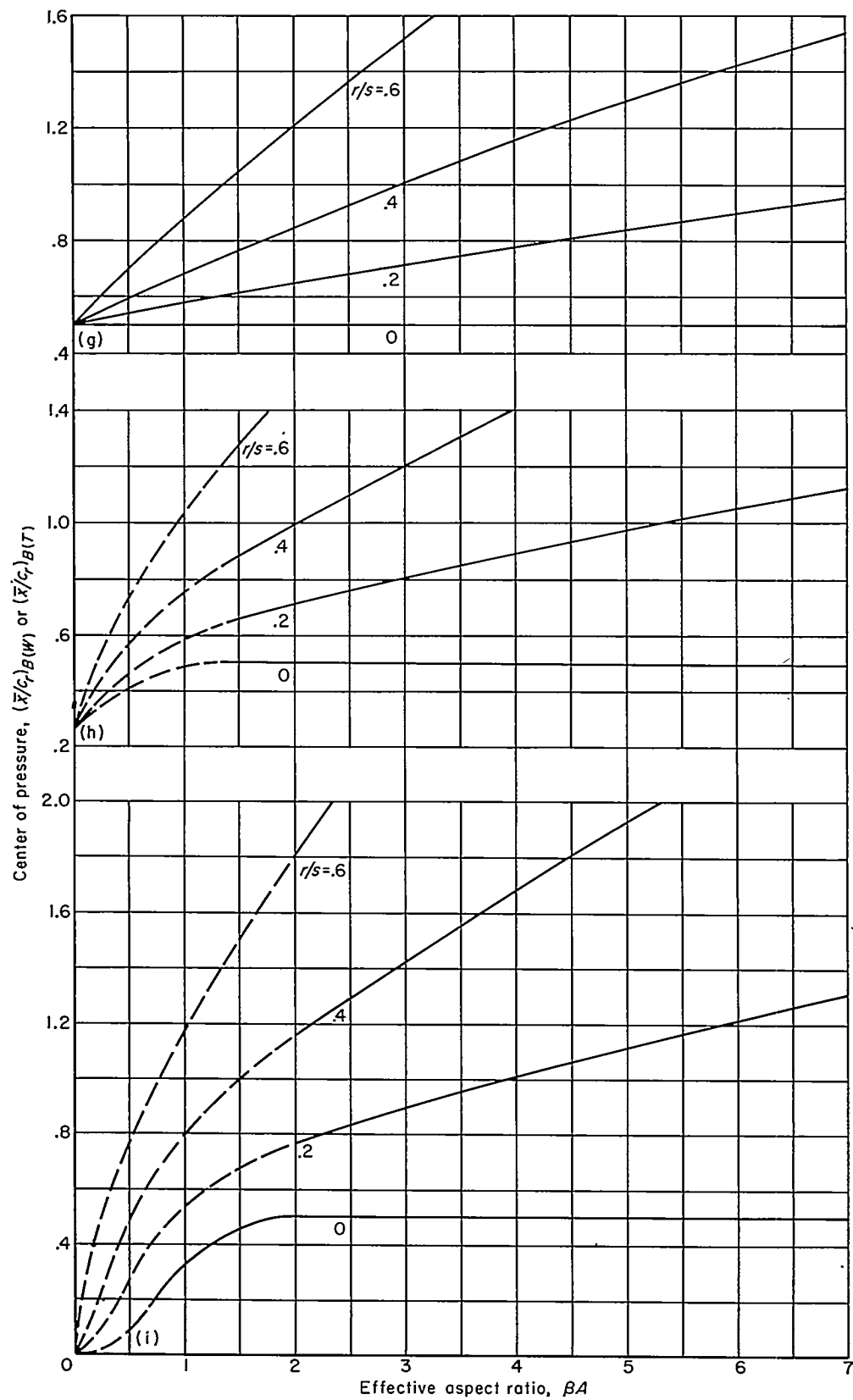
(a) No leading-edge sweep,  $\lambda=0$ . (b) No leading-edge sweep,  $\lambda=\frac{1}{2}$ . (c) No leading-edge sweep,  $\lambda=1$ .

CHART 15.—Charts for determination of  $(\bar{x}/c_r)_{B(W)}$  or  $(\bar{x}/c_r)_{B(T)}$  at supersonic speeds for wings and tails with afterbodies.



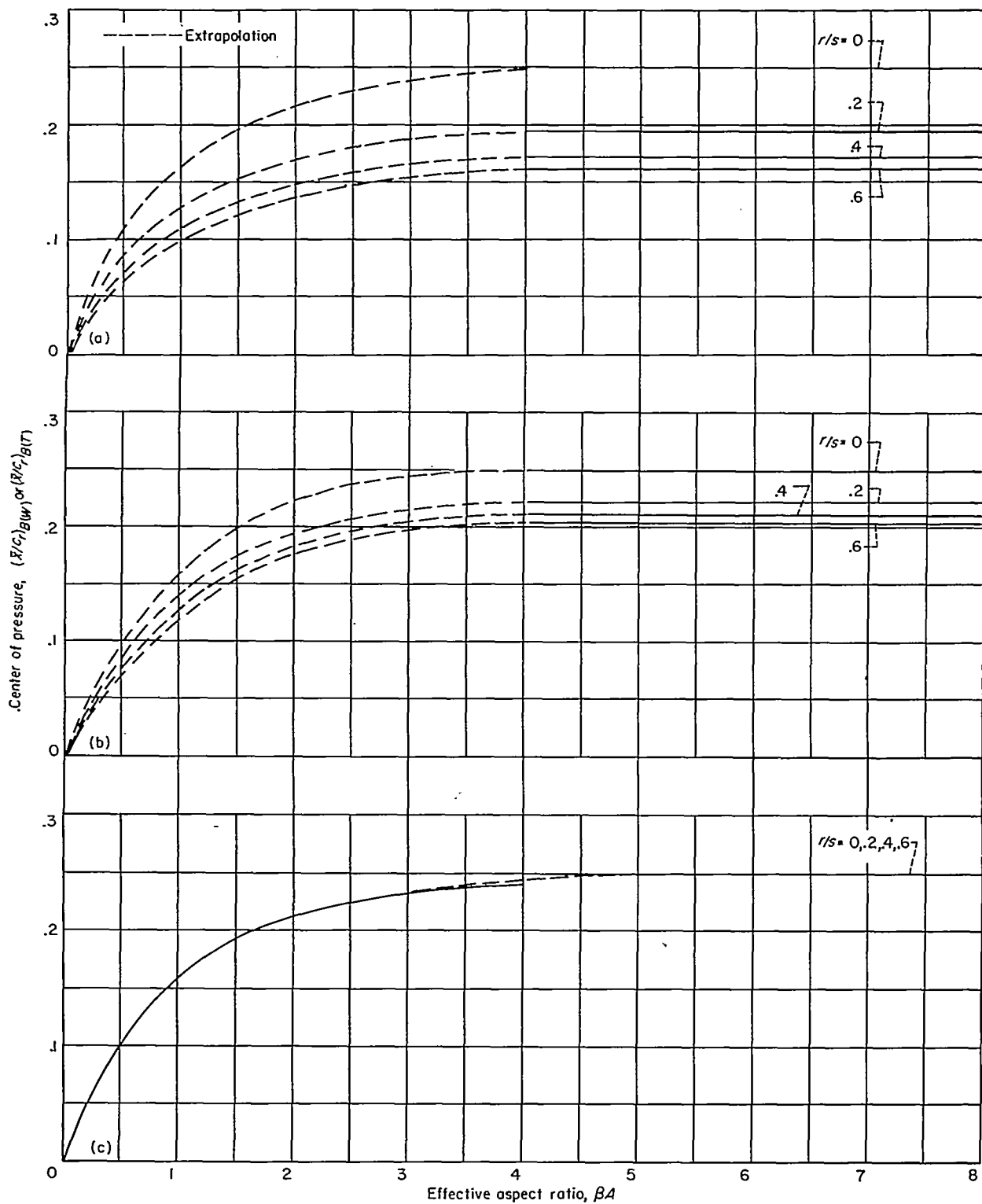
- (d) No midchord sweep,  $\lambda=0$ .  
 (e) No midchord sweep,  $\lambda=1/2$ .  
 (f) No midchord sweep,  $\lambda=1$ .

CHART 15.—Continued.



- (g) No trailing-edge sweep,  $\lambda=0$ .  
 (h) No trailing-edge sweep,  $\lambda=1/2$ .  
 (i) No trailing-edge sweep,  $\lambda=1$ .

CHART 15.—Concluded.

(a) No leading-edge sweep,  $\lambda=0$ .(b) No leading-edge sweep,  $\lambda=1/2$ .(c) No leading-edge sweep,  $\lambda=1$ .CHART 16.—Charts for determination of  $(\bar{x}/c_r)_{B(W)}$  or  $(\bar{x}/c_r)_{B(T)}$  at subsonic speeds.

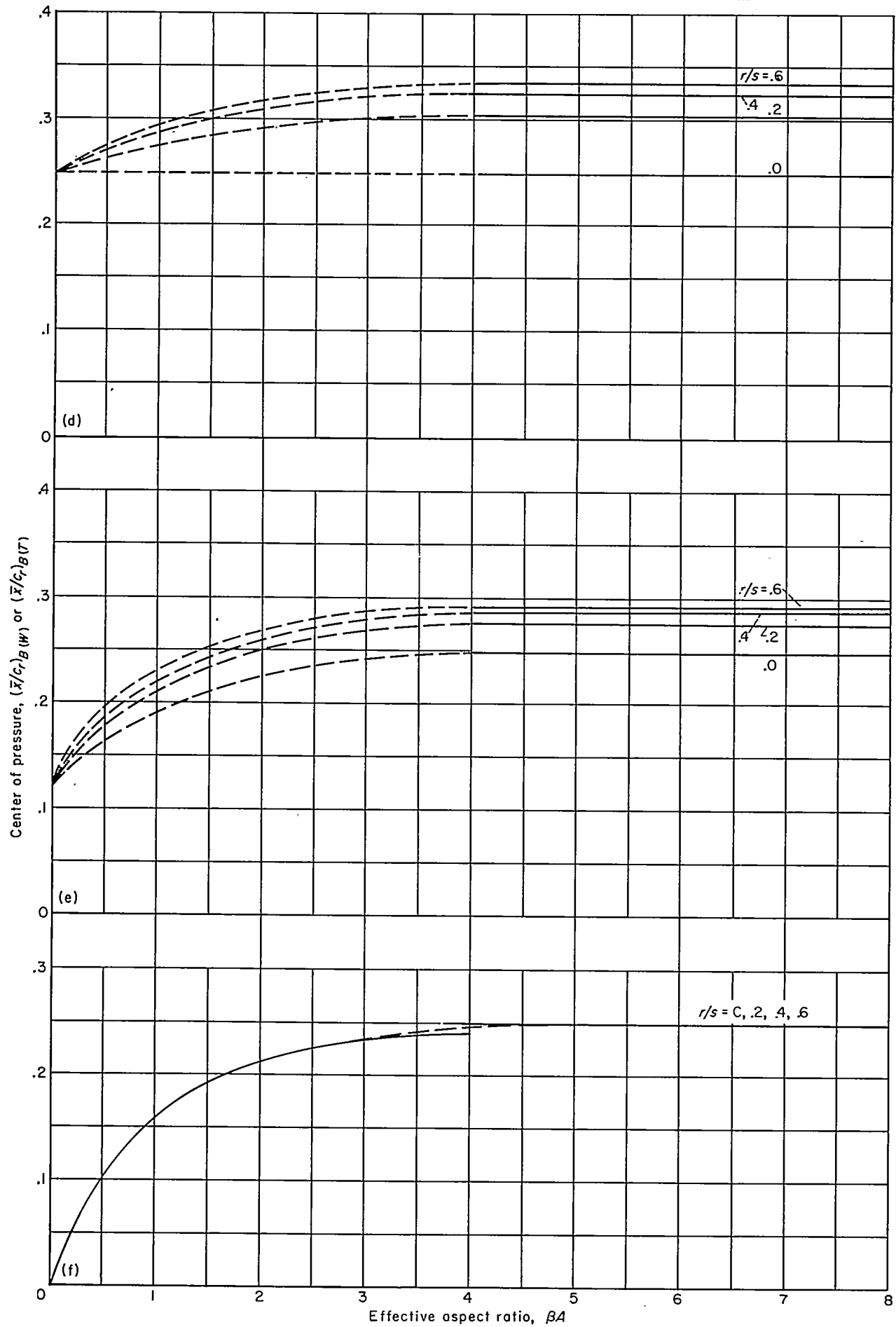
(d) No midchord sweep,  $\lambda=0$ .(e) No midchord sweep,  $\lambda=1/2$ .(f) No midchord sweep,  $\lambda=1$ .

CHART 16—Continued.

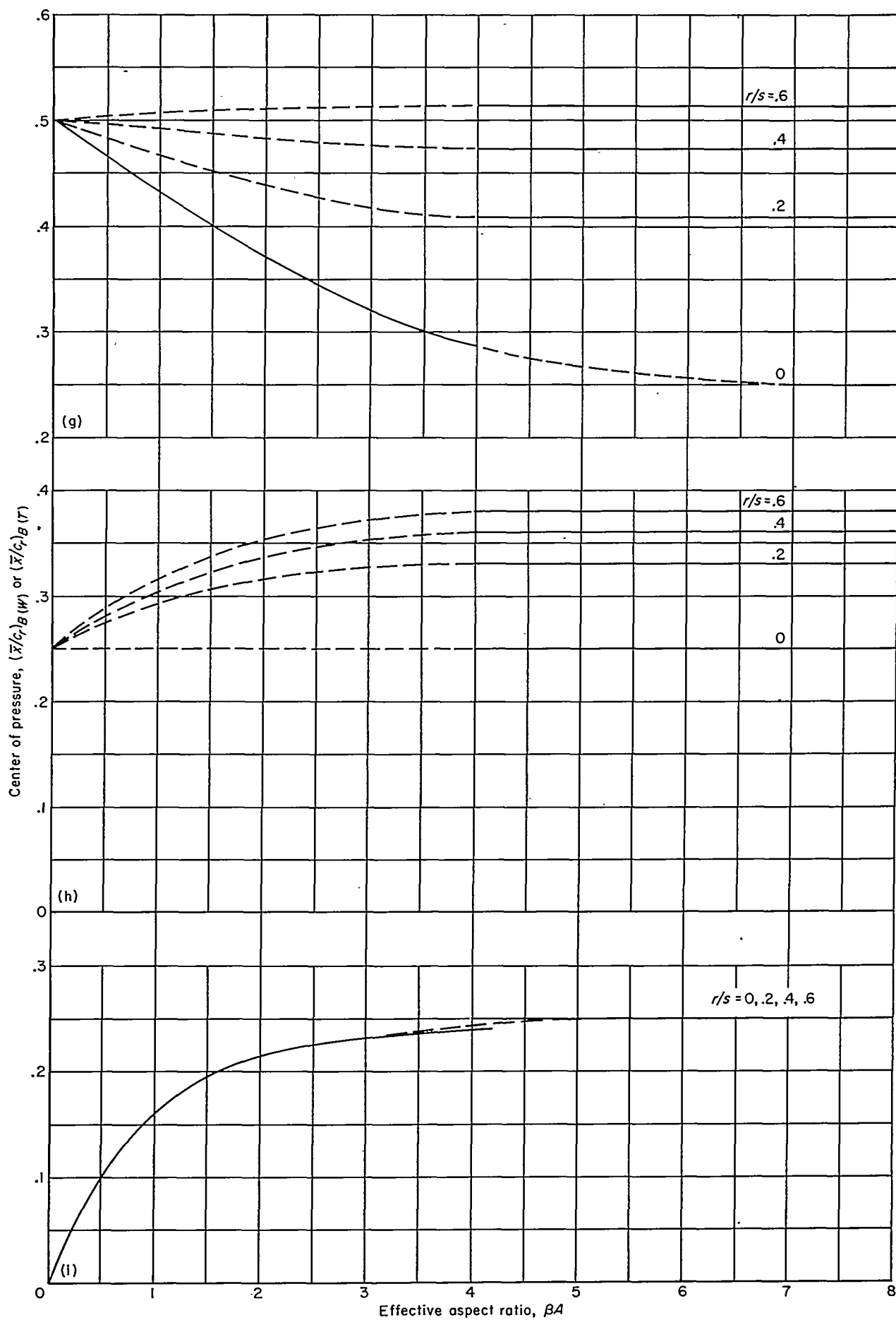
(g) No trailing-edge sweep,  $\lambda=0$ .(h) No trailing-edge sweep,  $\lambda=1/2$ .(i) No trailing-edge sweep,  $\lambda=1$ .

CHART 16.—Concluded.